To the Graduate Council:

I am submitting herewith a dissertation written by Mounir Laroussi entitled "Plasma Heating by Collisional Magnetic Pumping." I have examined the final copy of this dissertation for form and content and recommend that it be accepted in partial fulfillment of the requirements for the degree of Doctor of Philosophy, with a major in Electrical Engineering.

J. Reece Roth, Major Professor

We have read this dissertation
and recommend its acceptance:

Accepted for the Council:

Vice Provost
and Dean of the Graduate School

PLASMA HEATING BY
COLLISIONAL MAGNETIC PUMPING

A Dissertation

Presented for the

Doctor of Philosophy

Degree

The University of Tennessee, Knoxville

Mounir Laroussi

June 1988

TO MY PARENTS

Habib and Mannana Laroussi

ACKNOWLEDGEMENTS

The author is deeply indebted to Professor J. Reece Roth for excellent working conditions, good advice, and financial support. He also extends his gratitude to the remaining members of his dissertation committee: Professor I. Alexeff, Professor M. O. Pace, Associate Professor D. Rosenberg, and Professor L. G. Christophorou.

Special thanks go to Associate Professor Henry C. Simpson for his help and good suggestions.

The author wishes to thank Roberta L. Campbell for typing the manuscript of this dissertation with infinite patience, and Jenny L. Craven for drafting the figures.

Special thanks go to his wife Nicole C. Laroussi for her support and her constant help in typing the early drafts.

Finally, the author wishes to express his unbounded appreciation to his parents for their relentless support and encouragement throughout his academic career.

This work was supported by the Air Force Office of Scientific Research under contract 86-0100 (Roth).

ABSTRACT

Collisional magnetic pumping as a plasma heating method is investigated theoretically, computationally, and experimentally. Improvement of the efficiency of this heating method is also achieved. The theoretical treatment yields solutions to the energy transfer equations. The solution is presented in the form of an energy increase rate, which gives quantitatively the amount of energy increase per RF driving cycle. The RF wave adds a small perturbation to the background steady state DC magnetic field that confines the plasma. Depending on the type of waveform used, the energy increase rate obtained can be of first or second order in the amplitude of the magnetic field perturbation.

Two waveforms are used in this work. The first is a sinewave with variable frequency and amplitude. The energy increase rate in this case is proportional to the second power of the magnitude of the perturbation. This yields a small amount of heating for small perturbations. The second waveform used is a sawtooth with adjustable frequency and amplitude. The energy increase rate in this case is proportional to the first power of the magnitude of the perturbation. This yields an improvement of several orders of magnitude over the previous case.

Two circuits have been implemented to study experimentally the effects of the above mentioned perturbations on a cylindrical plasma generated by a classical Penning discharge. The circuit generating the sinusoidal perturbation is a high-Q parallel resonant circuit with tunable resonance frequency. The circuit generating the sawtooth perturbation is a switch-mode configuration using state-of-the-art metal-oxide-semiconductor transistors

capable of switching on and off in few tens of nanoseconds and of handling high curents and voltages. The experimental heating data collected in both cases is presented and discussed.

TABLE OF CONTENTS

CHAPTER			PAGE
I.	INTRODUCTION AND SUMMARY		1
II.	THEORETICAL TREATMENT OF COLLISIONAL MAGNETIC PUMPING		6
	II.1	Introduction	6
	II.2	Theoretical Analysis	10
		II.2.1 The equations and their first order solution	10
		II.2.2 Application to a sinewave perturbation	16
		II.2.3 Application to a sawtooth perturbation	22
		II.2.4 Comparison between first order heating rate and other plasma heating processes	27
	II.3	Conclusion	30
III.	COMPUTATIONAL TREATMENT		32
	III.1	Introduction	32
	III.2	Application to a Triangular Waveform	34
	III.3	Application to a Sinewave	41
	III.4	Application to a Sawtooth Waveform	48
	III.5	Conclusion	51
IV.	EXPERIMENTAL APPLICATION OF COLLISIONAL MAGNETIC PUMPING TO A CLASSICAL PENNING DISCHARGE PLASMA		54
	IV.1	Introduction	54
	IV.2	Design and Implementation of the Exciter Coil	54
	IV.3	Design, Implementation, and Testing of the High-Q Resonant Circuit	56
	IV.4	Design, Implementation, and Testing of the MOS Switching Circuit	60

CHAPTER PAGE

IV.5 Experimental Data Analysis 68

IV.5.1 Second order heating data 68

IV.5.2 First order heating data 74

IV.6 Conclusion 85

V. CONCLUSIONS 87

BIBLIOGRAPHY 89

APPENDIXES 95

A. Magnetosonic Waves 96

B. Derivation of ℓ_1 101

C. Programs Used for the Numerical Computations 108

D. Characterization of the Penning Discharge 113

E. Characterization of the Plasma 127

F. Binary Collision Frequencies 172

VITA 177

LIST OF TABLES

TABLE		PAGE
E.1.	Differential cross-sections per unit solid angle in units of a_0^2 per steradian for various excited states of helium atoms and two scattering angles	133
E.2.	Total cross-sections in units of πa_0^2 for various excited states of helium atoms	133
E.3.	Cross-sections in units of 10^{-16} cm^2 of the Penning process obtained experimentally for atoms of thermal energies	138
E.4.	Cross-sections of various collision processes for a helium gas and electron energy of 10 eV	139
F.1.	Collision frequencies for the various binary collision processes	175

LIST OF FIGURES

FIGURE		PAGE
II.1.	Exciter coil around a cylindrical plasma	6
II.2.	a) Plasma Compressed during the positive half cycle; b) Plasma relaxed during the negative half cycle	7
II.3.	Magnetic field waveform for a sinewave perturbation	8
II.4.	Heating rate coefficient versus collision frequency	20
II.5.	Magnetic field waveform for a sawtooth perturbation	22
III.1.	Magnetic field waveform for a triangular perturbation	34
III.2.	Parallel component of the energy versus time for $\delta = 0.1, \nu_c T = 10, E_o = 300$ eV, and a triangular perturbation	36
III.3.	Perpendicular component of the energy versus time for $\delta = 0.1, \nu_c T = 10, E_o = 300$ eV, and a triangular perturbation	36
III.4.	Total energy versus time for $\delta = 0.1, \nu_c T = 10, E_o = 300$ eV, and a triangular perturbation	37
III.5.	Parallel component of the energy versus time for $\delta = 0.1$, $\nu_c T = 0.1, E_o = 300$ eV, and a triangular perturbation	38
III.6.	Perpendicular component of the energy versus time for $\delta = 0.1, \nu_c T = 0.1, E_o = 300$ eV, and a triangular perturbation	38
III.7.	Total energy versus time for $\delta = 0.1, \nu_c T = 0.1, E_o = 300$ eV, and a triangular perturbation	39
III.8.	Energy increase rate versus collisionality parameter for $\delta = 0.1, E_o = 300$ eV, and a triangular perturbation	40
III.9.	Energy increase rate versus field modulation factor for $E_o = 300$ eV, several collisionality parameters, and a triangular perturbation	42
III.10.	Magnetic field waveform for a sinusoidal perturbation	43
III.11.	Parallel component of the energy versus time for $\delta = 0.1$, $\nu_c T = 0.2, E_o = 300$ eV, and a sinusoidal perturbation	43

FIGURE PAGE

III.12. Total energy versus time for $\delta = 0.1$, $v_c T = 0.2$, $E_o = 300$ eV, and a sinusoidal perturbation 44

III.13. Parallel component of the energy versus time for $\delta = 0.1$, $v_c T = 6$, $E_o = 300$ eV, and a sinusoidal perturbation 44

III.14. Total energy versus time for $\delta = 0.1$, $v_c T = 6$, $E_o = 300$ eV, and a sinusoidal perturbation 45

III.15. Energy increase rate versus collisionality parameter for $\delta = 0.1$, $E_o = 300$ eV, and a sinusoidal perturbation 46

III.16. Energy increase rate versus field modulation factor for $E_o = 300$ eV, several collisionality parameters, and a sinusoidal perturbation 47

III.17. Magnetic field waveform for a sawtooth perturbation 48

III.18. Parallel component of the energy versus time for $\delta = 0.01$, $v_c T = 0.2$, $E_o = 300$ eV, and a sawtooth perturbation 49

III.19. Perpendicular component of the energy versus time for $\delta = 0.01$, $v_c T = 0.2$, $E_o = 300$ eV, and a sawtooth perturbation 49

III.20. Total energy versus time for $\delta = 0.01$, $v_c T = 0.2$, $E_o = 300$ eV, and a sawtooth perturbation 50

III.21. Total energy versus time for $\delta = 0.01$, $v_c T = 6$, $E_o = 300$ eV, and a sawtooth perturbation 50

III.22. Energy increase rate versus collisionality parameter for $\delta = 0.01$, $E_o = 300$ eV, and a sawtooth pertubation 52

III.23. Energy increase rate versus field modulation factor for $E_o = 300$ eV and a sawtooth perturbation 53

IV.1. L-C parallel resonant circuit driven by a sinusoidal source 57

IV.2. Logarithmic magnitude of the impedance versus frequency 58

IV.3. Magnitude of the real part of the impedance versus frequency 59

IV.4. Magnitude of the imaginary part of the impedance versus frequency 59

FIGURE PAGE

IV.5. Experimental setup for generating a sinusoidal perturbation 61

IV.6. Ideal DC voltage source driving an inductor 62

IV.7. Ideal DC voltage source driving an inductor with a damping resistor 63

IV.8. a) Switch control voltage; b) Current waveform 64

IV.9. Circuit generating a periodic current sawtooth through the exciter coil 66

IV.10. State of the transistors when the switch is on 67

IV.11. State of the transistors when the switch is off 67

IV.12. Electron kinetic temperature increase versus field modulation for a sinewave perturbation 71

IV.13. Ion energy distributions with and without magnetic pumping for $V_A = 1.9$ kV, $I_A = 12$ mA, P = 60 μ Torr, $\delta = 0.002$, and a sinusoidal perturbation 72

IV.14. Ion energy distributions with and without magnetic pumping for $V_A = 1.6$ kV, $I_A = 18$ mA, P = 66 μ Torr, $\delta = 0.003$, and a sinusoidal perturbation 72

IV.15. a) Reflection coefficient converted into impedance when plasma is off; b) Reflection coefficient converted into impedance when plasma is on 73

IV.16. a) Scope trace of the control signal with 5 μs/division on the horizontal axis (f = 75 kHz) and 5 volts/division on the vertical axis; b) current trace with 5 μs/division horizontally and 4 amperes/division vertically; c) Gate voltage trace with 5 μs/division horizontally and 5 volts/division vertically 76

IV.17. a) Scope trace of the control signal with 20 μs/division on the horizontal axis (f = 40 kHz) and 5 volts/division on the vertical axis; b) Current trace with 20 μs/division horizontally and 5 amperes/division vertically; c) Gate voltage trace with 20 μs/division horizontally and 5 volts/division vertically ... 76

IV.18. Scope trace of inductor current and resistor voltage (f = 100 kHz) when a) Plasma is off; b) Plasma is on c) Peak of resistor voltage with 5 μs/division horizontally and 5 volts/division vertically, when plasma is off; d) When plasma is on 79

FIGURE		PAGE
IV.19.	DC and RF power decrease versus driving frequency	80
IV.20.	Electron kinetic temperature increase versus power decrease for a sawtooth perturbation	81
IV.21.	Electron kinetic temperature increase versus driving frequency for a sawtooth perturbation	82
IV.22.	Ion energy distributions with and without magnetic pumping for V_A = 2.2 kV, I_A = 32 mA, P = 110 μ Torr, f = 100 kHz, and a sawtooth perturbation	86
A.1.	Vector orientation for a magnetosonic wave	96
D.1.	Schematic of the classical Penning discharge with uniform axial magnetic field in the plasma volume	114
D.2.	Axial profile of the background magnetic field	115
D.3.	Axial profile of the number density at V_A = 1.5 kV, I_A = 40 mA, P = 100 μ Torr, B = 0.255 T	117
D.4.	Axial profile of the electron kinetic temperature at V_A = 1.5 kV, I_A = 40 mA, P = 100 μ Torr, B = 0.255 T	118
D.5.	Axial profile of the ion kinetic temperature at V_A = 1.5 kV, I_A = 40 mA, P = 100 μ Torr, B = 0.255 T	119
D.5.	Axial profile of the floating potential at V_A = 1.5 kV, I_A = 40 mA, P = 100 μ Torr, B = 0.255 T	120
D.5.	Axial profile of the plasma potential at V_A = 1.5 kV, I_A = 40 mA, P = 100 μ Torr, B = 0.255 T	121
D.8.	Electron kinetic temperature versus magnetic field strength at V_A = 1.5 kV, I_A = 40 mA, P = 100 μ Torr	122
D.9.	Ion kinetic temperature versus magnetic field strength at V_A = 1.5 kV, I_A = 40 mA, P = 100 μ Torr	122
D.10.	Plasma number density versus magnetic field strength at V_A = 1.5 kV, I_A = 40 mA, P = 100 μ Torr	123
D.11.	RF emission spectrum with 100 MHz/division horizontal and 40 μV/division vertical	125
E.1.	Angular distribution of electrons elastically scattered by helium atoms	131

FIGURE PAGE

E.2. Elastic scattering cross-section of slow electrons by helium atoms 131

E.3. Excitation function for a $5^1S \rightarrow 2^1P$ helium transion 134

E.4. Angular distribution of 200 eV incident electrons after the 2^1P and 3^1P transions in helium atoms 134

E.5. Cross-section for ionization of helium atoms by electron impact based on Born's approximation, in units of πa_o^2, where a_0 is the Bohr radius, ao = 0.529×10^{-10} m 136

E.6. Vector orientation for a density gradient generated drift wave 141

E.7. Block diagram of a two channel acquisition and handling system 151

E.8. Autopower spectra (A and B), coherency spectrum (C), and phase spectrum (D) of two potential fluctuations detected by two capacitive probes 90° apart, P = 190 μ Torr, V_A = 1.3 kV, I_A = 56 mA, B = 0.262 Tesla 154

E.9. Autopower spectra (A and B), coherency spectrum (C), and phase spectrum (D), of two potential fluctuations detected by two capacitive probes 90° apart, P = 210 μ Torr, V_A = 1.3 kV, I_A = 58 mA, B = 0.3 Tesla 155

E.10. Autopower spectra (A and B), coherency spectrum (C), and phase spectrum (D), of two capacitive probes 26 cm apart at the same azimuthal angle, θ = 0°. P = 210 μ Torr, V_A = 1.3 kV, I_A = 58 mA, B = 0.3 Tesla 156

E.11. Autopower spectra on linear frequency scale (A), and on logarithmic frequency scale (B) with a spectral index n = 2.5, P = 47 μ Torr, V_A = 1.6 kV, I_A = 22 mA, B = 0.3 Tesla 158

E.12. Autopower spectrum on linear frequency scale (A), and on logarithmic frequency scale (B) with a spectral index n = 2.92, P = 55 μ Torr, V_A = 1.6 kV, I_A = 24 mA, B = 0.347 Tesla 159

E.13. Autopower spectrum on linear frequency scale (A), and on logarithmic frequency scale (B), with a spectral index n = 3.57, P = 50 μ Torr, V_A = 1.6 kV, I_A = 20 mA, B = 0.395 Tesla 160

FIGURE PAGE

E.14. Autopower spectra of potential fluctuations at V_A = 1.3 kV, I_A = 2 mA, P = 30 μ Torr, and various magnetic field Strengths 161

E.15. Mode frequency versus inverse of the magnetic field strength 162

E.16. Mode frequency versus anode voltage 164

E.17. Experimental setup for the measurement of the effective collision frequency 169

E.18. Resonant absorption curve with an effective collision frequency of 7.5 MHz 170

LIST OF SYMBOLS

*Important parameters are underlined.
*SI units are used throughout the text.

α	Heating rate coefficient
α	Attenuation factor; Phase angle
$\alpha_{n\phi}$	Phase spectrum between density and potential fluctuations
β	Phase coefficient; Heating rate coefficient
γ	Phase factor; Heating rate
$\gamma_{n\phi}$	Coherency spectrum between density and potential fluctuations
γ^e_k	Instability growth rate
δ	Field modulation factor
ε_o	Permittivity of free space, 8.854×10^{-12} farad/m
ε	Electron energy
$\varepsilon(\omega)$	Complex dielectric function
η_ℓ	Phase shift of partial wave
θ	Azimuthal angle
Λ	Argument of Coulomb logarithm
λ	Characteristic exponent; Wave length
λ_D	Debye length
μ_o	Permeability of free space, $4\pi \times 10^{-7}$ henry/m
μ	Magnetic moment
μ	Refractive index
ν_c	Collision frequency
ν_{eff}	Effective collision frequency
π	3.14159
ρ	Resistivity
σ	Cross-section
τ	Characteristic time
ϕ	Electrostatic potential
ψ	Wave function
ω	Angular frequency
ω_p	Plasma frequency
Ω	Gyro frequency
A	Atomic weight
B	Magnetic induction
c	Speed of light, 2.998×10^8 m/sec.
E	Electric field
E	Expected value; Energy
$E_\parallel$	Component of the energy parallel to the magnetic field direction
$E_\perp$	Component of the energy perpendicular to the magnetic field direction.
e	Electronic charge, 1.602×10^{-19} coulomb
e^-	Electron
He	Helium
h	Planck's constant, 6.623×10^{-34} joule-sec
I	Electric current
I	Differential cross-section
k	Wave number
k	Boltzmann's constant, 1.380×10^{-23} joule/°C

L	Length
M	Mass; Target mass
m	Particle mass; Mode number
N	Equilibrium number density
n	Plasma number density
P	Magnetic pressure; Power
Q	Quadrature spectrum
Q	Quality factor
q	Electric charge
R	Resistance; Correlation function
r	Radius; Radial coordinate
S	Power spectral density; Distance
s	Skin depth
T	Kinetic temperature; Period
T	Transport spectral density
t	Time
V	Volume; Potential
$\bar{v}$	Mean thermal velocity
v	Velocity
$v_{\parallel}$	Component of the velocity parallel to the magnetic field
$v_{\perp}$	Component of the velocity perpendicular to the magnetic field
W	Energy
x	Cartesian coordinate
y	Cartesian coordinate
z	Cartesian coordinate
Z	Ionic charge number

CHAPTER I

INTRODUCTION AND SUMMARY

In controlled fusion experiments, it is necessary to heat the plasma to kinetic temperatures high enough that the ions overcome the Coulomb barrier and fuse. If a mixture of deuterium and tritium gas is used as the fuel in a fusion reactor, the kinetic temperature of the ions has to be at least 4.2 keV for the fusion reaction to be ignitable. Plasma heating is therefore crucial in the start-up and possibly the operation of fusion reactors. For this reason, a variety of methods to heat plasmas to thermonuclear temperatures have been suggested and experimentally tested. The adoption of a particular heating method is based on its technological practicality, on its efficiency, and on its economics. Some of the heating methods currently used in magnetic fusion are ohmic heating, electron and ion cyclotron heating, and neutral beam injection (Roth, 1986).

Magnetic pumping was first suggested as a heating method (for the Stellarator-C) by Spitzer et al. in the 1950's (Spitzer et al., 1953). A theoretical analysis was published by Berger et al. a few years later (Berger et al., 1958). These papers constitute most of the very limited early literature on this subject. This was so because heating by magnetic pumping was first a part of a classified project, and at last neglected due to the attention given to other more promising heating methods, such as ion-cyclotron resonance heating.

Magnetic pumping can be applied to a straight cylindrical section of a plasma, confined by an axial uniform steady state magnetic field B_0, by wrapping a coil around it and exciting the coil by an RF field. The confining

magnetic field thus has an RF perturbation superimposed on it. The change of the magnetic field in time generates an electric field, E, perpendicular to it which in turn produces an ExB_0 force. This force tends to compress and relax the plasma periodically. Under favorable conditions, the mechanical energy exerted by the compressing force would ultimately be absorbed by the plasma and lead to a heating of the charged particles. Depending on how the plasma parameters and the driving force relate to each other, different heating regimes are obtained. In the case of collisional magnetic pumping, which is the main interest of this dissertation, the collisions are the mediator between the RF field and the charged particles. To achieve heating by collisional magnetic pumping, the charged particles have to undergo many collisions before leaving the heating region. Mathematically, the following inequalities have to be satisfied:

$$\omega_{tr} << \nu_c \sim \omega << \omega_{cy}.$$

Where ω_{tr}, ν_c, ω, and ω_{cy} are respectively the transit frequency through the heating region, the collision frequency, the RF field frequency, and the particle gyrofrequency.

To study the process of the energy transfer between the RF field and the charged particles analytically, we start from the assumption that for a magnetic field slowly varying in time and space, the magnetic moment, defined as the ratio of the perpendicular component of the kinetic energy to the magnetic field, is a constant of motion. Then, we derive a general equation relating the change in the total energy of a particle to the change of the magnetic field. This equation is

$$\frac{d^2E}{dt^2} - \left[-\frac{3}{2}\nu_c + \frac{d^2B}{dt^2}\left(\frac{dB}{dt}\right)^{-1} \right] \frac{dE}{dt} - \frac{\nu_c}{B}\frac{dB}{dt}E = 0. \qquad \text{(I.1)}$$

This is an homogeneous, linear, second order differential equation with periodic coefficients which can go to infinity periodically. Such equations usually appear in astronomical studies, and their general solution was given by the French mathematician G. Floquet (Floquet, 1883). Using Floquet's theory and a perturbation treatment, Burger et al. derived the energy increase rate when a sinusoidal perturbation is applied (Berger et. al, 1958). The way Floquet's theory was used, and the mathematical steps leading to the solution, were not published. To verify the result given by Berger et al. for the particular case of a sinusoidal perturbation, and to fill in the missing mathematical steps, the solution for the energy increase rate is rederived and agreement with the result of Berger et al. is reached. The energy increase rate (or heating rate) in this case is

$$\frac{dE}{dt} = \frac{\delta^2}{6} \frac{v_c \omega^2}{\frac{9}{4} v_c^2 + \omega^2} E_o, \tag{I.2}$$

where δ is the field modulation factor defined as

$$\delta = \frac{\Delta B}{B_o} << 1. \tag{I.3}$$

Two parameters stand out in the expression of the heating rate. These are the field modulation factor δ, and the collision frequency v_c. The heating rate is maximum when $\omega = (3/2)\, v_c$, and is given by

$$\left.\frac{dE}{dt}\right|_{Max} = \frac{\delta^2 v_c}{12} E_o. \tag{I.4}$$

Equation (I.4) shows that the higher the collision frequency, the better is the energy absorption. But, because δ is a small number and the heating rate is proportional to δ^2, the energy absorption is small for δ values less than 10%.

Equation (I.1) is then solved for the general case where an arbitrary perturbation function is assumed. Such a result has not previously been

published. A condition for the achievement of a heating rate proportional to the first power of the field modulation factor, δ, is derived. It is found that a sawtooth perturbation satisfies the condition for first order heating, and the heating rate for this case is

$$\frac{dE}{dt} = \frac{\delta\omega}{3\pi} E_o . \qquad (I.5)$$

This can be an improvement of many orders of magnitude on the sinusoidal case, especially at very small values of δ ($\delta < 0.1$), where the perturbation treatment is valid. Small values of δ are also much easier to achieve experimentally.

A computational analysis of the equations describing the energy transfer process is also done. This analysis allows us to monitor the evolution in time of the parallel and perpendicular components of the energy when collisional magnetic pumping is applied. A parameter, called the "collisionality parameter" is defined. It is, $\nu_c T$, the product of the collision frequency and the period of the RF field. Different computational runs for several collisionality parameters and for several perturbation waveforms are made. From the plots of the two components of the energy and the total energy itself, the heating rate is computed, and the limitations of the method are revealed as a function of the collisionality parameter. A comparison between the analytical and the numerical results is then made, and good agreement demonstrated.

Two experimental setups have been achieved to apply collisional magnetic pumping to a weakly ionized plasma produced by a classical Penning discharge. The first experiment consists of the application of a sinewave perturbation to the background magnetic field. The effect on the energy of the particles is diagnosed by measurement of the electron and ion

kinetic temperatures with a Langmuir probe, by monitoring the particle's energy distribution with a retarding potential analyser, and by observing the changes in the plasma impedance. In the second experiment a state-of-the-art switching circuit has been designed and built to generate a current sawtooth of adjustable frequency and amplitude. When applied to the plasma this circuit adds a sawtooth-shaped perturbation to the background magnetic field. The effect on the energy of the particles is diagnosed as described above.

The material in this dissertation is arranged in the following manner. Chapter II presents the detailed theoretical treatment of collisional magnetic pumping. Chapter III presents the computational results. In Chapter IV we describe the experimental apparatus used to apply collisional magnetic pumping. An analysis of the experimental heating data follows. These three chapters are the main contribution of this work and they contain an innovative way to study this heating method. Therefore new understanding of the potential and limitations of collisional magnetic pumping is brought to light. In Chapter V the conclusions are presented.

CHAPTER II

THEORETICAL TREATMENT OF COLLISIONAL MAGNETIC PUMPING

II.1 Introduction

Magnetic pumping is achieved by wrapping an exciter coil around a cylindrical plasma and perturbing the confining magnetic field, $B = B_0(1 + \delta f(t))$, where B_0 is the uniform steady state background magnetic field, δ is the field modulation factor defined as $\delta = \Delta B/B_0$, and $f(t)$ is a periodic function of time. Fig II.1 represents such a situation.

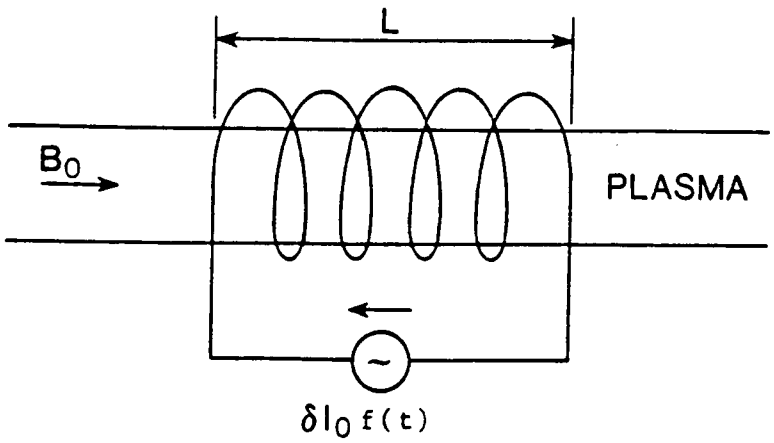

Fig II.1. Exciter coil around a cylindrical plasma.

Contrary to ohmic heating, where the electric field is parallel to the confining axial magnetic field, in magnetic pumping the oscillating electric field is produced by variation of the axial magnetic field and thus is perpendicular to it. This type of heating was called "Magnetic Pumping" due to the existence of a compressional wave propagating perpendicular to the

background magnetic field, causing the plasma to be cyclically compressed and relaxed by an alternating E x B force. This is illustrated in Fig II.2.

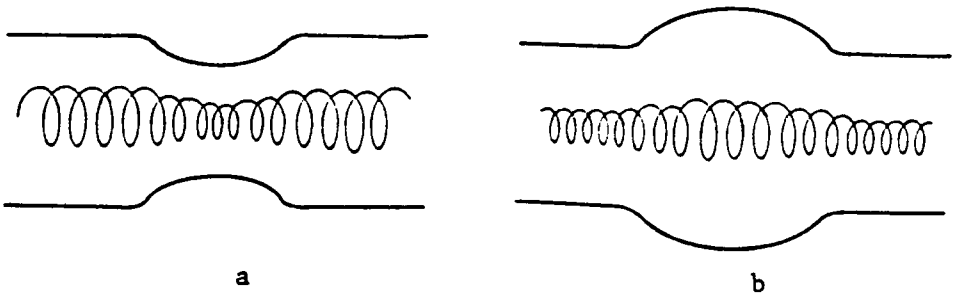

Fig II.2. a) Plasma compressed during the positive half cycle; b) Plasma relaxed during the negative half cycle.

The compressive wave is a magnetosonic wave (or magneto-acoustic wave). The latter is an extraordinary electromagnetic mode with a frequency well below the gyrofrequency. Contrary to Alfven waves, which travel along B_0, magnetosonic waves travel across B_0 at the Alfven speed $V_A = B_0 (1/\mu n_0 m_i)^{1/2}$, where n_0 is the charged particle (electrons or ions) density, m_i is the ion mass, and μ is the permeability of the plasma. Appendix A is an in-depth study of magnetosonic waves. When magnetic pumping is used, four characteristic times play a role in how the plasma is heated (Berger et. al, 1958). These are the gyration period τ_{cy}, the collision time τ_c, the period of the oscillating field τ_p, and the transit time of the particles through the heating region τ_{tr}. Depending on how these times relate to each other, different heating methods result. Four limiting cases appear to be possible ways to heat a plasma.

1. Cyclotron Resonance Heating

In this method of heating the following inequalities are required:

$$\tau_{cy} \sim \tau_f << \tau_{tr} << \tau_c . \qquad \text{(II.1)}$$

Since the frequency of the oscillating field is near the gyrofrequency, the velocities of the particles are always in phase with the electric field, leading to a continuous acceleration of the particles. This heating method is then very efficient. The maximum energy increase per cyclotron period is

$$\Delta E_\perp = \frac{nE\sqrt{2m E_\perp}}{B_0}, \qquad \text{(II.2)}$$

where $E_\perp$ is the perpendicular component of the energy, E is the electric field amplitude, and B_0 the magnetic field (Roth, 1986).

2. Transit Time Heating

The inequalities pertaining to this case are

$$\tau_{cy} << \tau_{tr} \sim \tau_f << \tau_c . \qquad \text{(II.3)}$$

In this heating method the particles cross the heating region without suffering a significant number of collisions. Since the period of the oscillating field is much larger than the gyration period, the magnetic moment of the particles is assumed to be a constant of motion. The magnetic moment of a particle gyrating around a magnetic field line is defined as

$$\mu = \frac{E_\perp}{B}, \qquad \text{(II.4)}$$

where $E_\perp$ is the perpendicular component of the kinetic energy of the particle, defined as

$$E_\perp = \frac{m v_\perp^2}{2}. \qquad \text{(II.5)}$$

The equation of motion in this case is

$$m \frac{d^2 z}{dt^2} = - \mu \frac{\partial B}{\partial z}, \qquad \text{(II.6)}$$

where μ is the magnetic moment, B the magnetic field, m the mass of the particle, and z is the axial direction. By assuming a magnetic field profile

$$B = B_0 + B_1 e^{-\left(\frac{z}{a}\right)^2} \cos(\omega t - \alpha), \tag{II.7}$$

and using a perturbation treatment, Burger et al. derived the following energy change (Berger et. al, 1958)

$$<\Delta E>_\alpha = \frac{\pi}{m}\left(\frac{\mu B_1 a\,\omega}{2 v_\parallel}\right)^2\left(\frac{\omega^2 a^2}{v_\parallel^2} - 2\right)\exp\left(-\frac{a^2\omega^2}{2 v_\parallel^2}\right), \tag{II.8}$$

where $<\Delta E>_\alpha$ is the energy change averaged over all possible phases, and $v_\parallel$ is the zeroth-order parallel velocity.

3. Acoustic Heating

To achieve this mode of heating the following inequalities have to be satisfied

$$\tau_{cy} << \tau_c << \tau_f \sim \tau_{tr}\,. \tag{II.9}$$

In highly turbulent or dense plasmas in which the effective mean free path of the particles is small, the oscillating field produces density variations which result in the propagation and dissipation of sound waves in the plasma.

4. Collisional Heating

This heating method is the main interest of this dissertation. The inequalities to be satisfied are

$$\tau_{cy} << \tau_c \sim \tau_f << \tau_{tr}\,. \tag{II.10}$$

In this case, the particles suffer many collisions while crossing the heating region, but since the period of the oscillating field is much larger than the gyration period, the magnetic moment of the particles is a constant of motion between collisions. The magnetic field assumes the form $B = B_0\,(1 + \delta f(t))$, where $\delta << 1$, so that the external oscillator provides a small perturbation on the original static magnetic field. If the heating region is of length L and the parallel velocity of the particles is $v_\parallel$, the above inequalities can also be

written as

$$\frac{v_{\parallel}}{L} << v_c \sim \omega << \omega_{cy} \qquad \text{(II.11)}$$

where $v_{c,}$ ω, and ω_{cy} are respectively the collision frequency, the driving frequency, and the gyrofrequency.

II.2 Theoretical Analysis

II.2.1 The equations and their first order solution

In the absence of collisions, the constancy of the magnetic moment makes it possible to obtain a relationship between the time rate of change of the perpendicular component of the energy and the time rate of change of the magnetic field. Thus, by taking the derivative of the magnetic moment, $\mu = E_{\perp}/B$, with respect to time we get

$$\frac{d\mu}{dt} = 0 = \frac{1}{B}\frac{dE_{\perp}}{dt} - \frac{E_{\perp}}{B^2}\frac{dB}{dt}, \qquad \text{(II.12)}$$

from which we obtain

$$\frac{dE_{\perp}}{dt} = \frac{E_{\perp}}{B}\frac{dB}{dt}. \qquad \text{(II.13)}$$

The total energy E of the ions is given by

$$E = E_{\parallel} + E_{\perp}, \qquad \text{(II.14)}$$

where $E_{\parallel}$ is the ion energy along the magnetic field lines, and $E_{\perp}$ is the ion energy perpendicular to the magnetic field lines, with two degrees of freedom.

If no collisions occur, the perpendicular component of the ion energy , $E_{\perp}$, oscillates with the frequency ω, and no net heating occurs. If collisions do occur, however, some of the energy in the perpendicular component is transferred to the parallel component $E_{\parallel}$. In kinetic equilibrium, the parallel component of the energy will be equal to one half the perpendicular component, as a result of equipartition. When the perpendicular component is

driven by magnetic pumping, a periodic departure from equipartition occurs, and energy can be transferred between the parallel and perpendicular components. This may be expressed mathematically by adding a collisional term to Equation (II.13), as follows

$$\frac{dE_\perp}{dt} = \frac{E_\perp}{B}\frac{dB}{dt} - \nu_c\left(\frac{E_\perp}{2} - E_\parallel\right), \tag{II.15}$$

and

$$\frac{dE_\parallel}{dt} = \nu_c\left(\frac{E_\perp}{2} - E_\parallel\right). \tag{II.16}$$

Now summing Equation (II.15) and (II.16) and using Equation (IV.14) one obtains:

$$\frac{dE}{dt} = \frac{E_\perp}{B}\frac{dB}{dt} = \mu\frac{dB}{dt}. \tag{II.17}$$

Thus, the rate of change of the total ion energy is proportional to the magnetic moment, and the time rate of change of the magnetic field.

The net energy transfer can be obtained by taking the second derivative of Equation (II.17) and then using Equation (II.15) and (II.16) to eliminate the first derivative of the parallel and perpendicular components of the energy. Further, using Equation (II.17) itself to eliminate the perpendicular component of energy, one obtains:

$$\frac{d^2E}{dt^2} - \left[-\frac{3}{2}\nu_c + \frac{d^2B}{dt^2}\left(\frac{dB}{dt}\right)^{-1}\right]\frac{dE}{dt} - \frac{\nu_c}{B}\frac{dB}{dt}E = 0. \tag{II.18}$$

Substituting for B the expression $B = B_0(1 + \delta f(t))$ into the above equation yields

$$\frac{d^2E}{dt^2} + \left(\frac{3}{2}\nu_c - \frac{\ddot{f}(t)}{\dot{f}(t)}\right)\frac{dE}{dt} - \nu_c\frac{\delta\dot{f}(t)}{1 + \delta f(t)}E = 0. \tag{II.19}$$

Let

$$A(t) = \frac{3}{2}\nu_c - \frac{\ddot{f}(t)}{\dot{f}(t)}, \tag{II.20}$$

and

$$g(t) = - v_c \frac{f'(t)}{1 + \delta f(t)} . \qquad (II.21)$$

Equation (II.19) can be written

$$\frac{d^2E}{dt^2} + A(t) \frac{dE}{dt} + \delta g(t) E = 0 . \qquad (II.22)$$

Equation (II.22) is an homogeneous linear differential equation of second order with periodic coefficients, describing the change in the total energy of the particles due to collisional magnetic pumping. Examples of such equations are Mathieu's equation and Hill's equation, which appear in astronomical and other applications where the stability and perturbation of periodic systems is at issue. The general solutions of these equations have been given by Floquet. Floquet's theory predicts a solution of the following form (Floquet, 1883)

$$E(t) = a_1 e^{\lambda_1 t} P_1(t) + a_2 e^{\lambda_2 t} P_2(t) . \qquad (II.23)$$

The parameters λ_1 and λ_2 are called the characteristic exponents and can be calculated from the characteristic equation associated with the differential equation, and $P_1(t)$ and $P_2(t)$ are periodic functions with a period equal to that of the coefficients of the differential equation. Since $\delta = \Delta B/B_0$ is a small quantity, Equation (II.22) can be solved using a perturbation treatment around the parameter δ. The characteristic exponents λ_1 and λ_2 can be represented by the following series (Laroussi, 1986)

$$\lambda_1 = - \frac{3}{2} v_c + \delta \ell_1 + \delta^2 \ell_2 + \ldots . \qquad (II.24)$$

$$\lambda_2 = \delta \ell_1 + \delta^2 \ell_2 + \ldots . \qquad (II.25)$$

The solution associated with λ_1 is damped in time since the first term dominates the series, and therefore does not represent steady state heating. For this reason, only the solution associated with λ_2, with positive coefficients ℓ_k,will be kept and used. The solution representing heating is then expressed as

$$E(t) = e^{\lambda_2 t} P_2(t). \tag{II.26}$$

$P_2(t)$ can be expanded as a series of the powers of δ as follows

$$P_2(t) = P_{20} + \delta P_{21}(t) + \delta^2 P_{22}(t) + \ldots., \tag{II.27}$$

Where $P_{2i}(t)$ are periodic functions. P_{20} is the initial value and is set equal to 1 for the sake of simplicity. Now, by using the solution predicted by Floquet's theory along with the above perturbation treatment, Equation (II.22) can be solved for the different powers of the parameter δ.

Solving for the first power of δ, g(t) can be expressed as

$$g(t) = - v_c f'(t), \tag{II.28}$$

and

$$E(t) = \ell_1 t + P_{21}(t). \tag{II.29}$$

Equation (II.22) is then reduced to

$$\frac{d^2 P_{21}(t)}{dt^2} + A(t) \frac{d P_{21}(t)}{dt} = K(t), \tag{II.30}$$

where

$$K(t) = - g(t) - \ell_1 A(t). \tag{II.31}$$

The detailed mathematical development required to solve the above equation is presented in Appendix B. The solution is

$$P_{21}(t) = C_1 + C_2 \int_0^t e^{-a(s)} ds + \left(\int_0^t e^{-a(u)} du \right) \left(\int_0^t e^{a(u)} K(u) du \right)$$

$$- \int_0^t e^{a(s)} \left(\int_0^s e^{-a(u)} du \right) K(s) ds, \qquad \text{(II.32)}$$

where

$$a(t) = \int_0^t A(u) du . \qquad \text{(II.33)}$$

Using the fact that $P_{21}(t)$ is periodic, the constant C_2 can be determined

$$C_2 = \frac{e^{-a(T)}}{1 - e^{-a(T)}} \int_0^t K(s) e^{a(s)} ds . \qquad \text{(II.34)}$$

Substituting this expresson for C_2 into the following equations

$$P_{21}(T) - P_{21}(0) = 0 , \qquad \text{(II.35)}$$

$$P'_{21}(T) - P'_{21}(0) = 0 , \qquad \text{(II.36)}$$

and letting

$$Q(s) = e^{a(s)} \left[\frac{1}{1 - e^{-a(T)}} \int_0^T e^{-a(u)} du - \int_0^s e^{-a(u)} du \right], \qquad \text{(II.37)}$$

leads to the result

$$\int_0^T K(s) Q(s) ds = 0 . \qquad \text{(II.38)}$$

Knowing that

$$K(t) = - g(t) - \ell_1 A(t) ,$$

the expression of ℓ_1 can be found

$$\ell_1 = - \frac{\int_0^T g(s) Q(s) ds}{\int_0^T A(s) Q(s) ds} . \qquad \text{(II.39)}$$

Substituting for A(t) and Q(t) their respective expressions in the denominator, and integrating by parts gives

$$\int_0^T A(s)Q(s)ds = T \ . \tag{II.40}$$

So

$$\ell_1 = -\frac{1}{T}\int_0^T g(s)Q(s)ds. \tag{II.41}$$

Now, by substituting the expressions for g(s) and Q(s) in the above equation, the coefficient ℓ_1 is found to be

$$\ell_1 = \frac{v_c}{T}\int_0^T \exp\left(\frac{3}{2}v_c s\right)\left\{\frac{1}{1-\exp\left(-\frac{3}{2}v_c T\right)}\int_0^T \exp\left(-\frac{3}{2}v_c u\right)f'(u)du\right.$$

$$\left. -\int_0^s \exp\left(-\frac{3}{2}v_c u\right)f'(u)du\right\}ds. \tag{II.42}$$

A detailed mathematical development showing all the steps of the above analysis is found in Appendix B. The coefficient ℓ_1 has the dimension 1/s. The energy increase per cycle for $\ell_1 \neq 0$ can be calculated by expanding E(t) as follows

$$E(t) = E_0 + \delta(\ell_1 t E_0 + P_{21}(t)) + \text{higher order terms in } \delta. \tag{II.43}$$

For a cycle $T = 2\pi/\omega$ the energy increase is

$$\Delta E = E(T) - E(0) = \delta\ell_1 \frac{2\pi}{\omega} E_0, \tag{II.44}$$

where $P_{21}(T)$ and $P_{21}(0)$ cancel each other due to the periodicity of $P_{21}(t)$. E_0 is the initial value of the total particle energy. The energy increase rate is

$$\frac{\Delta E}{T} = \delta\ell_1 E_0. \tag{II.45}$$

II.2.2 Application to a sinewave perturbation

Let us now assume that the background magnetic field has a sinusoidal perturbation superimposed on it, according to the expression

$$B = B_0(1 + \delta \cos \omega t) . \qquad \text{(II.46)}$$

Fig II.3 shows the waveform of the magnetic field.

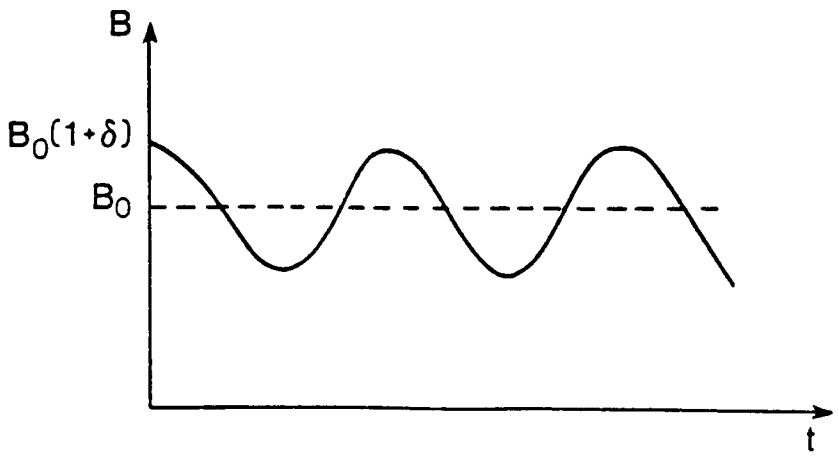

Fig II.3. Magnetic field waveform for a sinewave perturbation.

Plugging f(t) = cos ωt in Equation (II.42) for ℓ_1, it is easily shown that ℓ_1 = 0. In this case, the energy increase is proportional to a higher order of δ than the first. Another way of checking the above result, and at the same time calculating the next coefficient ℓ_2 in the expansion,is to go back to the initial differential equation and substitute cos ωt for f(t). Doing this, Equation (II.22) becomes

$$\frac{d^2E}{dt^2} - \left[-\frac{3}{2} v_c + \frac{\omega \cos \omega t}{\sin \omega t} \right] \frac{dE}{dt} + \frac{\delta v_c \sin \omega t}{1 + \delta \cos \omega t} E = 0 . \qquad \text{(II.47)}$$

Since $\delta << 1$, the term $(1 + \delta \cos \omega t)^{-1}$ can be expanded in a Taylor series,

$$(1 + \delta \cos \omega t)^{-1} \approx 1 - \delta \cos \omega t + \text{higher order terms.} \qquad \text{(II.48)}$$

Substituting Equation (II.48) into Equation (II.47) one obtains

$$\frac{d^2E}{dt^2} - \left[-\frac{3}{2} v_c + \frac{\omega \cos \omega t}{\sin \omega t} \right] \frac{dE}{dt} + \delta v_c \omega \sin \omega t (1 - \delta \cos \omega t) E = 0. \qquad \text{(II.49)}$$

The part representing heating in Floquet's solution is

$$E(t) = e^{\lambda_2 t} P_2(t). \qquad \text{(II.26)}$$

where

$$\lambda_2 = \delta \ell_1 + \delta^2 \ell_2 + \text{higher order terms in } \delta. \qquad \text{(II.25)}$$

and

$$P_2(t) = P_{20} + \delta P_{21}(t) + \delta^2 P_{22}(t) + \text{higher order terms in } \delta. \qquad \text{(II.27)}$$

Solving for the first power of δ, Equation (II.49) becomes

$$\frac{d^2P_{21}}{dt^2} + \left[\frac{3v_c}{2} - \omega \operatorname{ctn} \omega t \right] \frac{dP_{21}}{dt} = -\frac{3}{2} \ell_1 v_c + \ell_1 \omega \operatorname{ctn} \omega t - v_c \omega \sin \omega t, \qquad \text{(II.50)}$$

where P_{20} was set equal to 1 for the sake of simplicity.

The homogeneous solution of the above equation is

$$P_{21}(t) = C_1 e^{-\frac{3v_c}{2} t} \{a \cos \omega t + b \sin \omega t\} + C_2, \qquad \text{(II.51)}$$

where

$$a = \frac{-\omega}{\omega^2 + \frac{9}{4} v_c^2}, \qquad \text{(II.52)}$$

and

$$b = \frac{-\frac{3}{2} v_c}{\omega^2 + \frac{9}{4} v_c^2}. \qquad \text{(II.53)}$$

The particular solution of Equation (II.50) is:

$$P_{21}(t) = -\ell_1 t + v_c a \sin \omega t - v_c b \cos \omega t + \ell_1 a \operatorname{ctn} \omega t$$

$$+\left(\frac{-\ell_1}{\sin\omega t}-\frac{2}{3}\omega\right)\left(a\cos\omega t+b\sin\omega t\right). \qquad (II.54)$$

Now setting the secular term equal to zero (since $P_{21}(t)$ is periodic), provides the result $\ell_1 = 0$. This is in agreement with what was previously predicted. Solving for the second power of δ, Equation (II.49) becomes

$$\frac{d^2P_{22}}{dt^2}+\left[\frac{3}{2}v_c-\omega\,\mathrm{ctn}\,\omega t\right]\frac{dP_{22}}{dt}=-\frac{3}{2}\ell_2 v_c+\ell_2\,\omega\,\mathrm{ctn}\,\omega t$$

$$+v_c\ \omega\sin\omega t\cos\omega t-v_c\ \omega\sin\omega t\ P_{21}(t). \qquad (II.55)$$

As previously, the interesting part of the solution is the particular solution, and the important part of the particular solution is the part containing the secular term, P_{sec}. The latter is found to be

$$P_{sec}=\left(\frac{3}{2}\ell_2 v_c\ b+a\,\ell_2\omega-\frac{1}{6}v_c\ \omega a\right)t \qquad (II.56)$$

Setting this term equal to zero and solving for ℓ_2, we get

$$\ell_2=\frac{v_c\,\omega^2}{6(\omega^2+\frac{9}{4}v_c^2)}. \qquad (II.57)$$

To calculate the energy increase per cycle, the expression for the energy has to be expanded as follows

$$E(t)=e^{\lambda_2 t}P_2(t)=(1+\delta^2\ell_2 t+\ldots)(P_{20}(t)+\delta P_{21}(t)+\delta^2P_{22}(t)+\ldots). \qquad (II.58)$$

Retaining only up to the second order terms in δ, E(t) can be expressed as

$$E(t)=P_{20}(t)+\delta P_{21}(t)+\delta^2(P_{22}(t)+\ell_2 t\ P_{20}(t))+\text{higher order terms in }\delta. \qquad (II.59)$$

At $t = 2\pi/\omega$, the energy has increased by

$$\Delta E=\delta^2\ell_2\frac{2\pi}{\omega}E_0. \qquad (II.60)$$

Inserting the expression for ℓ_2 in the above equation gives

$$\Delta E = \delta^2 E_0 \frac{\pi}{3} \frac{v_c \omega}{\frac{9}{4} v_c^2 + \omega^2} \quad \text{Joules/cycle.} \tag{II.61}$$

The energy increase rate is found by dividing ΔE by $\Delta t = 2\pi/\omega$ seconds/cycle, and taking the differential limit,

$$\frac{dE}{dt} = \frac{\delta^2}{6} \frac{\omega^2 v_c}{\frac{9}{4} v_c^2 + \omega^2} E_0 \quad \text{Joules/second.} \tag{II.62}$$

This result agrees with the one found by Berger et al. (1958). Equation (II.62) can be written as

$$\frac{dE}{dt} = \frac{E_0}{\tau_H} = \alpha E_0 \,, \tag{II.63}$$

where τ_H is the heating time defined as

$$\tau_H \equiv 6 \frac{\left(\frac{9}{4} v_c^2 + \omega^2\right)}{\delta^2 \omega^2 v_c} \,, \tag{II.64}$$

and $\alpha \equiv 1/\tau_H$ is the heating rate coefficient. The optimum frequency, at which the heating rate coefficient is maximum, is

$$\omega_{opt} = \frac{3}{2} v_c \,, \tag{II.65}$$

and the value of α at this frequency is

$$\alpha_{max} = \frac{\delta^2 v_c}{12} \,. \tag{II.66}$$

For a highly collisional plasma, $v_c >> \omega$, and the heating rate can be approximated by

$$\frac{dE}{dt} \approx \frac{2}{27} \frac{\delta^2 \omega^2}{v_c} E_0 \,. \tag{II.67}$$

On the other hand, for a relatively collisionless plasma, $v_c << \omega$, and the heating rate can be expressed as

$$\frac{dE}{dt} \approx \frac{\delta^2 \nu_c}{6} E_0 . \qquad \text{(II.68)}$$

As seen in the above analysis, the heating rate is proportional to ν_c in the low collisionality case, and to ν^{-1}_c in the highly collisional case. Fig II.4 is a schematic plot of the heating rate coefficient, α, the inverse of Equation (II.64), versus collision frequency.

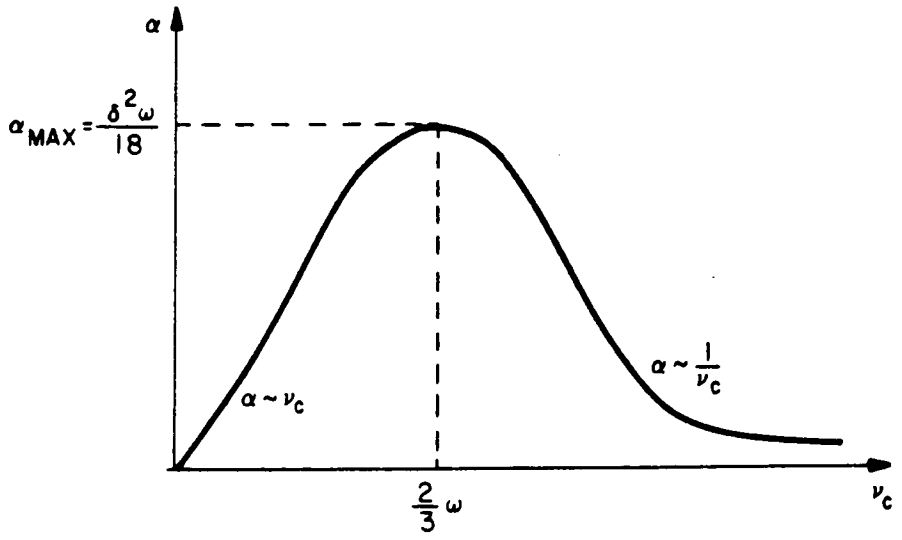

Fig II.4. Heating rate coefficient versus collision frequency.

To get a feeling for how different the rates of energy increase are in the above two cases, let's consider a plasma of fusion interest operating at the following parameters: $T_i = 2$ keV; $A = 2$; $n = 10^{19}/m^3$; $L = 0.5$ m; $B_0 = 2.0$ T. The binary particle collision frequency in this case is $\nu_c = \nu_{ii} = 1/\tau_{ii} \approx 313$ Hz leading to a heating rate coefficient

$$\alpha = \frac{\delta^2 \nu_c}{6} = 52\ \delta^2/\text{sec} .$$

Now if anomalous resistivity is present in the plasma, the collision frequency due to turbulence, etc. can be on the order of 5 MHz, leading to a maximum heating rate coefficient of

$$\alpha_{max} = \frac{\delta^2 \nu_c}{12} = 4.2\,10^5\,\delta^2/\text{sec}\ .$$

From the above two examples, it can be seen that the collisionality of the plasma can make a big difference to the efficiency of this heating method. If the plasma is turbulent, particles not only collide among themselves (binary collisions or Coulomb collisions) but also scatter off the fluctuating electric field associated with the turbulence. Due to this latter process, an anomalous momentum loss is created which enhances the collision frequency. This enhanced collision frequency, called the "effective collision frequency", is found to be 10 to 20 times higher than the binary collision frequency (Roth et al., 1987b). Appendix E contains an indepth description of the effective collision frequency.

The dependence of the heating rate coefficient on the square of the field modulation factor, δ, constitutes a major disadvantage for the application of a sinewave perturbation. This is because δ is a small number, which makes δ^2 even smaller, and therefore a relatively small energy increase is achieved. Intuitively, a heating rate coeficient proportional to the first power of the field modulation factor would be an improvement. To accomplish this, a perturbation function satisfying Equation (II.38) has to be found. Various modulation waveforms for B(t) have been tried. The choice of these had the physical basis that a undirectional flow of energy has to be maintained. This is in contrast with the sinusoidal case, where the magnetic field in the heating region is cyclically above and below the background value. This leads to a

half cycle. Any heating is therefore a second order effect, resulting from small differences of large numbers. Also important in the choice of the perturbation function is the ability to pump the plasma adiabatically for repetitive periods of time separated by very short durations when the plasma is not allowed to relax. A sawtooth perturbation has been found to be the answer to the above requirements.

II.2.3 Application to a Sawtooth Perturbation

If a sawtooth perturbation is applied, the total magnetic field expression takes the following form:

$$B = B_0\left(1 + \frac{\delta t}{T}\right) \text{ for } nT \le t < (n+1)T .$$

For the rest of this section, the time $t = T^-$ is defined as the time just before the magnetic field sharply decreases ($B(T^-) = B_0(1+\delta)$), and the time $t = T^+$ is defined as the time at which the magnetic field is equal to its background value, B_0. Fig II.5 shows the waveform assumed by the magnetic field.

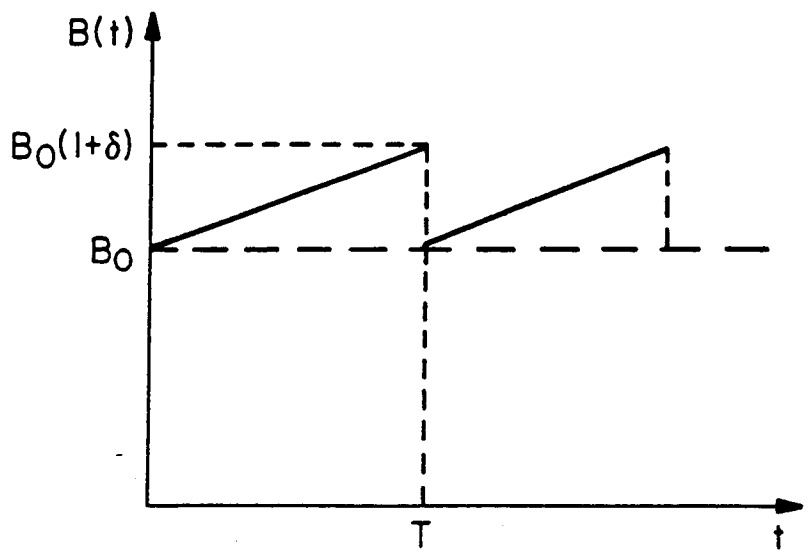

Fig II.5. Magnetic field waveform for a sawtooth perturbation.

The perturbation function is a repetitive ramp with a period equal to T = T^+. Since an instantaneous drop of the current generating this perturbation of the magnetic field is not feasible, an appropriate assumption would be that the fall time of the current is shorter than the collision time.

The differential equation describing the change of energy during the time interval [0, T^-] is given by

$$\frac{d^2E}{dt^2} + \frac{3}{2} v_c \frac{dE}{dt} - v_c \frac{\frac{\delta}{T}}{1 + \frac{\delta t}{T}} E = 0 \,. \qquad \text{(II.69)}$$

The term $(1 + \delta\, t/T)^{-1}$ can be expanded as

$$\left(1 + \frac{\delta t}{T}\right)^{-1} = 1 - \frac{\delta t}{T} + \ldots . \qquad \text{(II.70)}$$

Substituting Equation (II.70) into equation (II.69), one obtains

$$\frac{d^2E}{dt^2} + \frac{3}{2} v_c \frac{dE}{dt} - v_c \frac{\delta}{T}\left(1 + \frac{\delta t}{T} + \ldots\right) E = 0. \qquad \text{(II.71)}$$

Keeping only the terms in first order of δ, to solve for first order heating, Equation (II.71) becomes

$$\frac{d^2E}{dt^2} + \frac{3}{2} v_c \frac{dE}{dt} - v_c \frac{\delta}{T} E = 0. \qquad \text{(II.72)}$$

The solution of Equation (II.72) is

$$E(t) = C_1 e^{r_1 t} + C_2 e^{r_2 t}, \qquad \text{(II.73)}$$

where r_1 and r_2 are given by

$$r_1 = \frac{3}{4} v_c \left(-1 + \left(1 + \frac{16}{9} \frac{\delta}{v_c T}\right)^{1/2}\right), \qquad \text{(II.74)}$$

and

$$r_2 = \frac{3}{4} v_c \left(-1 - \left(1 + \frac{16}{9} \frac{\delta}{v_c T}\right)^{1/2}\right). \qquad \text{(II.75)}$$

The term $(1 + 16/9\ \delta/v_c T)^{1/2}$ can be expanded as

$$\left(1 + \frac{16}{9}\frac{\delta}{v_c T}\right)^{1/2} = 1 + \frac{8}{9}\frac{\delta}{v_c T} + \text{higher order terms}. \qquad (II.76)$$

Plugging Equation (II.76) into the expressions for r_1 and r_2 and keeping only the first order terms in δ, we get

$$r_1 = \frac{2}{3}\frac{\delta}{T}, \qquad (II.77)$$

and

$$r_2 = -\frac{3}{4} v_c \left(2 + \frac{8}{9}\frac{\delta}{v_c T}\right). \qquad (II.78)$$

The initial conditions are given by

$$E(o) = E_o, \qquad (II.79)$$

and

$$\left.\frac{dE}{dt}\right|_{t=o} = \frac{\delta}{T}\frac{2}{3} E_o. \qquad (II.80)$$

Applying these initial conditions to the expression of E(t) and solving for C_1 and C_2 yields

$$C_1 = E_o,$$

and

$$C_2 = 0.$$

The solution of Equation (II.72) subject to the above initial conditions is

$$E(t) = E_o e^{\frac{2}{3}\delta\frac{t}{T}}. \qquad (II.81)$$

This solution is only good in the time interval $0 \leq t < T$ and for $\delta/v_c T << 1$. At $t = T^-$, the energy is

$$E \sim E_o e^{\frac{2}{3}\delta} \sim E_o (1 + \frac{2}{3}\delta), \qquad (II.82)$$

which yields

$$\Delta E = E(T^-) - E(0) = \frac{2}{3}\delta E_o. \qquad (II.83)$$

Now let us examine what happens to the energy during the sharp fall of the magnetic field between T^- and T^+. During this time, the assumption of the constancy of the adiabatic invariant may be violated, so we have

$$\frac{d\mu}{dt} = \frac{1}{B}\frac{dE_\perp}{dt} - \frac{E_\perp}{B^2}\frac{dB}{dt}. \qquad \text{(II.84)}$$

Equation (II.84) can be written

$$\frac{dE_\perp}{dt} = \mu\frac{dB}{dt} + B\frac{d\mu}{dt}. \qquad \text{(II.85)}$$

Since no collisions occur between T^- and T^+, we have

$$\frac{dE_\parallel}{dt} = 0. \qquad \text{(II.86)}$$

Summing Equation (II.85) and Equation (II.86), we get

$$\frac{dE}{dt} = \mu\frac{dB}{dt} + B\frac{d\mu}{dt}. \qquad \text{(II.87)}$$

Equation (II.87) can also be written as

$$\frac{\Delta E}{\Delta t} = \mu\frac{\Delta B}{\Delta t} + B\frac{\Delta\mu}{\Delta t}, \qquad \text{(II.88)}$$

or

$$\Delta E = \mu\,\Delta B + B\,\Delta\mu. \qquad \text{(II.89)}$$

The change in magnetic moment, $\Delta\mu$ is given by

$$\Delta\mu = \mu(T^+) - \mu(T^-), \qquad \text{(II.90)}$$

with

$$\mu(T^-) = \frac{E_\perp(T^-)}{B_0(1+\delta)}, \qquad \text{(II.91)}$$

and

$$\mu(T^+) = \frac{E_\perp(T^+)}{B_0}. \qquad \text{(II.92)}$$

Since no collisions occur between T^- and T^+, we assume that no appreciable change in the perpendicular energy occurs. Thus we have

$$E_{\perp}(T^{+}) \approx E_{\perp}(T^{-}) = (1 + \delta)\, E_{\perp}(o). \qquad \text{(II.93)}$$

Due to equipartition we have

$$E_{\perp}(0) = \frac{2}{3} E_0,$$

which yields

$$\Delta\mu = \frac{2}{3}\,\delta\,\frac{E_o}{B_o}. \qquad \text{(II.94)}$$

Inserting Equation (II.94) into Equation (II.89) and substituting ΔB by $(-\delta B_0)$ we get

$$\Delta E = -\mu(T^{-})\,\delta B_o + B(T^{-})\,\frac{2}{3}\,\delta\,\frac{E_o}{B_o}. \qquad \text{(II.95)}$$

Using the fact that

$$\mu(T^{-}) = \frac{2}{3}\,\frac{E_o}{B_o}, \qquad \text{(II.96)}$$

and

$$B(T^{-}) = (1 + \delta)\, B_o, \qquad \text{(II.97)}$$

Equation (II.95) becomes

$$\Delta E = \frac{2}{3}\,\delta^2 E_o. \qquad \text{(II.98)}$$

Summing Equation (II.98) and (II.83) the energy increase per cycle is found to be

$$\Delta E = \frac{2}{3}\,\delta\,(1 + \delta) E_o. \qquad \text{(II.99)}$$

Since $\delta << 1$, Equation (II.99) can be approximated as

$$\Delta E = \frac{2}{3}\,\delta\, E_o. \qquad \text{(II.100)}$$

The heating rate dE/dt is given by

$$\frac{dE}{dt} = \frac{\delta\omega}{3\pi} E_o, \qquad \text{(II.101)}$$

where the period of the sawtooth is taken as $T = 2\pi/\omega$.

Equation (II.101) suggests that first order heating is achievable with a sawtooth perturbation and that the heating rate is independent of the collision frequency. This is an interesting result and of key importance for fusion machines where the mean free path is larger than the plasma length. To check this result, the generalized theory for first order heating already presented in Section II.2.1 is applied. Substituting f'(t) by its value for a sawtooth perturbation in Equation (II.42) yields the value of the coefficient ℓ_1

$$\ell_1 = \frac{\omega}{3\pi}. \tag{II.102}$$

Using Equation (II.45), the heating rate is found to be

$$\frac{dE}{dt} = \delta \ell_1 E_o = \frac{\delta\omega}{3\pi} E_o = \beta E_o, \tag{II.103}$$

where β is the heating rate coefficient given by

$$\beta = \frac{\delta\omega}{3\pi}, \tag{II.104}$$

This is in agreement with the result of Equation (II.101).

II.2.4 Comparison between first order heating rate and other plasma heating processes.

In order to have a quantitative idea on how beneficial it is to achieve first order heating by collisional magnetic pumping, we have to answer the following question: How does this heating rate compare to other plasma heating methods?

First let's compare the two heating rate coefficients obtained when sinusoidal and sawtooth perturbations are applied to collisional magnetic pumping. For this, the ratio of the two coefficients given by Equations (II.104) and the inverse of (II.64) is taken

$$\frac{\beta}{\alpha} = \frac{\delta\omega}{3\pi} \frac{6\left(\frac{9}{4} v_c^2 + \omega^2\right)}{\delta^2 \omega^2 v_c}, \qquad \text{(II.105)}$$

where β and α are respectively the heating rate coefficients for a sawtooth and a sinusoidal perturbation. Assuming that the RF driving frequency and the field modulation factor, δ, are the same for both cases the above ratio becomes

$$\frac{\beta}{\alpha} = \frac{\frac{9}{2} v_c^2 + 2\omega^2}{\pi\delta\,\omega\, v_c}. \qquad \text{(II.106)}$$

If the plasma is highly collisional we have $v_c >> \omega$ and Equation (II.105) becomes

$$\frac{\beta}{\alpha} = \frac{9}{2\pi} \frac{v_c}{\delta\,\omega}. \qquad \text{(II.107)}$$

The above ratio is much larger than unity. For a small δ and a large collision frequency to driving frequency ratio, β can be as much as three orders of magnitude larger than α.

If the plasma is collisionless, we have $\omega >> v_c$ and Equation (II.106) becomes

$$\frac{\beta}{\alpha} = \frac{2}{\pi} \frac{\omega}{\delta\, v_c}. \qquad \text{(II.108)}$$

As in the above case, this ratio is much larger than unity and for a small value of δ and a large ω/v_c, β can be two to three orders of magnitude larger than α.

The ratio β/α is minimum when $\omega = (3/2)\, v_c$. It is given by

$$\frac{\beta}{\alpha} = \frac{6}{\pi\delta}. \qquad \text{(II.109)}$$

This is still a number greater than one. For a field modulation factor of 1%, we have

$$\beta = 191\,\alpha. \qquad \text{(II.110)}$$

It therefore appears that in all cases first order heating is an improvement on second order heating. It provides a heating rate coefficient at least one order of magnitude larger than otherwise possible with second order heating.

Ion cyclotron resonant heating is one of the most efficient and widely used heating methods in fusion experiments. The maximum energy increase per cyclotron period obtained by this method is given by (Roth, 1986)

$$\Delta E_{\perp} = \frac{\pi E (2m E_{\perp})^{1/2}}{B_0}, \qquad (II.2)$$

where E is the electric field amplitude of the wave, B_0 the background magnetic field, and $E_{\perp}$ the perpendicular component of the energy whose equipartitioned value is equal to 2/3 of the total energy. The energy increase rate is given by

$$\gamma = \frac{\Delta E_{\perp}}{\tau_c} = q E \left(\frac{E_{\perp}}{2m} \right)^{1/2}, \qquad (II.111)$$

where τ_c is the cyclotron period given by

$$\tau_c = \frac{2\pi m}{q B}. \qquad (II.112)$$

To compare the above energy increase rate to the one obtained by first order heating with collisional magnetic pumping, their ratio is taken,

$$\frac{\beta E_0}{\gamma} = \frac{\delta \omega (2m)^{1/2}}{3\pi q E} \frac{E_0}{E_{\perp}^{1/2}}. \qquad (II.113)$$

To acquire a quantitative idea of the above ratio, typical values of the involved parameters are taken. Let $\omega = 2\pi\ 10^7$ rad/s, $\delta = 10^{-2}$, $E = 100$ V/cm, $E_0 =$ 1keV, and helium gas. The value of $\beta E_0/\gamma$ in percent is

$$\frac{\beta E_0}{\gamma} = 7.45\%.$$

Keeping in mind that the above ratio is taken for the maximum value the ICRH heating rate, γ, can reach, it can be concluded that first order collisional

magnetic pumping is a heating method that can be competitive with other widely used methods, such as ICRH.

II.3 Conclusion

In this chapter the equations describing the rate of change of the energy of the particles in a plasma adiabatically pumped with collisional magnetic pumping are presented. A general solution for first order heating along with particular solutions to the energy increase rate for two specific magnetic field perturbations are derived. This is a new treatment of this heating method which greatly extends any previous work done on this subject.

When a sinusoidal perturbation is superimposed on the background magnetic field, a heating rate proportional to the second power of the field modulation factor, δ, is obtained. This is in agreement with the result published without derivation by Berger et al. This heating rate is also strongly dependent on the collisionality of the plasma. A maximum heating rate is achieved when the driving RF frequency is 1.5 times larger than the collision frequency.

The application of a sinusoidal perturbation has two major drawbacks. The first is the dependence of the heating rate on the second power of the field modulation factor, δ. This number is less than unity and its square is even smaller. The second is the strong dependence of the heating rate on the collision frequency. This is especially disadvantageous for a fusion-grade plasma, where the mean free path is larger than the plasma length. These two drawbacks result in a small energy increase rate. In the past, these factors led researchers to neglect investigating this heating method any further.

In the search for more satisfactory results, a heating rate proportional to the first power of the field modulation factor and indirectly dependent on the collision frequency had to be found. A sawtooth perturbation proved to be a good alternative. The heating rate for this case is two to three orders of magnitude larger than that for second order heating, and is comparable to other widely used plasma heating methods.

CHAPTER III

COMPUTATIONAL TREATMENT

III.1 Introduction

The theoretical treatment of the preceding chapter provides us with solutions to the energy increase rate and how it relates to the collisionality in the plasma, but fails to give us a picture of the evolution of the energy with time from the instant that collisional magnetic pumping is turned on. For this purpose, a numerical solution to the energy transfer equation is sought. This solution provides us with numerical values of the energy for each time increment. This series of numbers can be plotted on an energy-time diagram. The energy increase rate can be easily extracted from such a diagram and compared with the analytical predictions.

The equations describing the variations of the parallel and perpendicular components of the energy are given by

$$\frac{dE_{\parallel}}{dt} = \nu_c\left(\frac{E_{\perp}}{2} - E_{\parallel}\right), \tag{III.1}$$

and

$$\frac{E_{\perp}}{dt} = \frac{E_{\perp}}{B}\frac{dB}{dt} - \nu_c\left(\frac{E_{\perp}}{2} - E_{\parallel}\right). \tag{III.2}$$

Since the total energy is the sum of $E_{\parallel}$ and $E_{\perp}$, we also have

$$\frac{dE}{dt} = \frac{dE_{\parallel}}{dt} + \frac{dE_{\perp}}{dt}. \tag{III.3}$$

The magnetic field is given by

$$B = B_o(1 + \delta f(t)), \tag{III.4}$$

which gives

$$\frac{1}{B}\frac{dB}{dt} = \frac{\delta f'(t)}{1 + \delta f(t)}. \tag{III.5}$$

Let

$$E_{\parallel} = x,$$

$$E_{\perp} = y,$$

and

$$F(t) = \frac{\delta f'(t)}{1 + \delta f(t)}.$$

Equations (III.1) and (III.2) can be written as

$$\frac{dx}{dt} = -v_c x + 0.5\, v_c y, \tag{III.6}$$

and

$$\frac{dy}{dt} = -v_c x - 0.5\, v_c y + y\, F(t), \tag{III.7}$$

For a given value of the collision frequency, v_c, a perturbation function f(t), and initial value x_0 and y_0, numerical values of x and y are computed and tabulated for each time step. A plotting routine furnishes the plots of x vs t and y vs t. The total energy is also plotted as $z = x + y$. The Fortran program for this computation is listed in Appendix C. The program has the flexibility of entering the values of the collision frequency, v_c, the period of the RF waveform, T, the field modulation factor, δ, the initial values of the energy components, and the time step size. The y-axis of the plots represents energy in electron-volts and the x-axis represents time in units of the period of the RF waveform, T. The number of periods plotted can be changed, allowing one to follow the evolution of the energy far enough in time to observe any transient period, along with any steady state reached.

Three waveforms have been studied. These are a triangular waveform, a sinusoidal waveform, and a sawtooth waveform. These waveforms can be implemented experimentally. This not only allows a comparison between theory and experiment, but also gives a sense of practicality to this work.

Since the collision frequency and how it relates to the RF frequency is an important factor that affects the heating rate, we define a *collisionality parameter*, v_cT, given by the product of the collision frequency and the period of the RF wave. The collisionality parameter is a dimensionless number which indicates how many collisions occur during one RF period. By varying v_cT, different regimes are obtained and the resulting heating rates are computed from the plots of the energy versus time.

III.2 Application to a Triangular Waveform

A triangular waveform of adjustable shape was first selected to study collisional magnetic pumping computationally, because it is a general case, one limit of which is a sawtooth waveform. Fig III.1 shows the magnetic field when a triangular perturbation is applied.

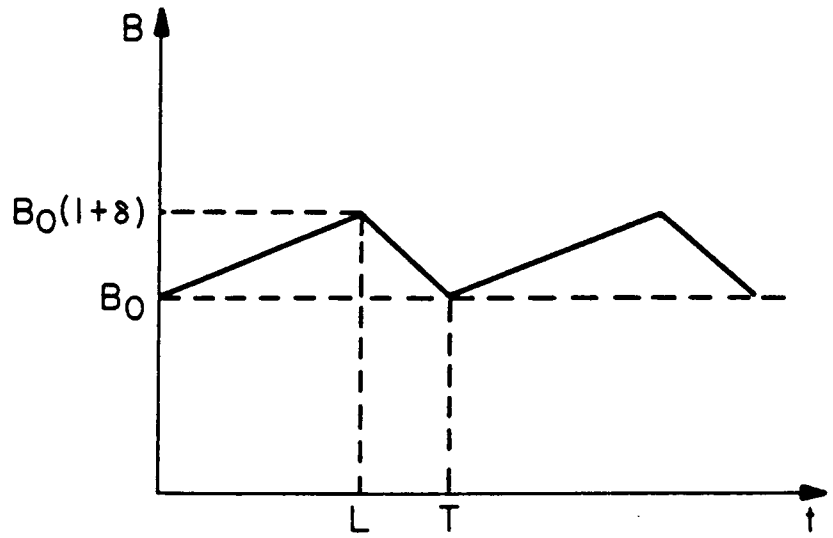

Fig III.1. Magnetic field waveform for a triangular perturbation.

If the ramping down time, (T-L), is gradually reduced until it becomes zero, a transition to a sawtooth waveform is achieved. This allows one to write a simple algorithm capable of showing the change in the energy waveform when the transition between triangular and sawtooth waveforms occurs.

First, a symmetrical triangular waveform and a collisional case is applied by setting the collisionality parameter, v_cT, equal to 10. This implies ten collisions per field period. A field modulation factor, δ, of 0.1 is chosen. As seen in Fig III.2 through Fig III.4, the parallel, perpendicular, and total energy oscillate with the field but their average values increase with time. The total energy increase per cycle for a particle with an initial energy of 300 eV is about 0.12 eV.

Now if the collisionality parameter is equal to 0.1, a low collisional case is obtained for which one collision occurs each ten field periods. As shown in Fig III.7, the total energy oscillates with the field but its average value does not increase with time. The explanation of this can be seen in Fig III.5, which shows the parallel component of the energy as a function of time. For a transient period lasting approximately 15T, where T is the period of the driving RF waveform, the parallel energy increases, but soon reaches a saturation plateau. As the field pumps the plasma further, no energy transfer between the perpendicular component of the energy and its parallel component occurs, which results in zero energy gain.

Setting the collisionality parameter equal to 20, an energy increase is also obtained, but of smaller magnitude than the $v_cT = 10$ case. This indicates that the energy increase rate has a maximum at some optimum value of the collisionality parameter. Fig III.8 shows a plot of the energy

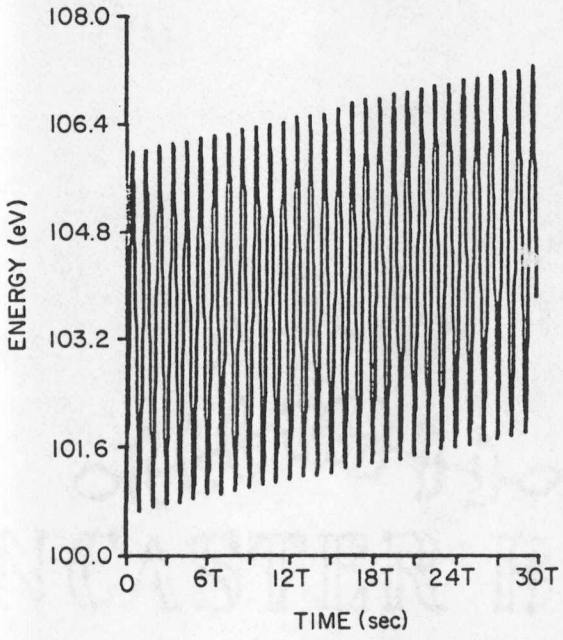

Fig III.2. Parallel component of the energy versus time for $\delta = 0.1$, $v_c T = 10$, $E_0 = 300$ eV, and a triangular perturbation.

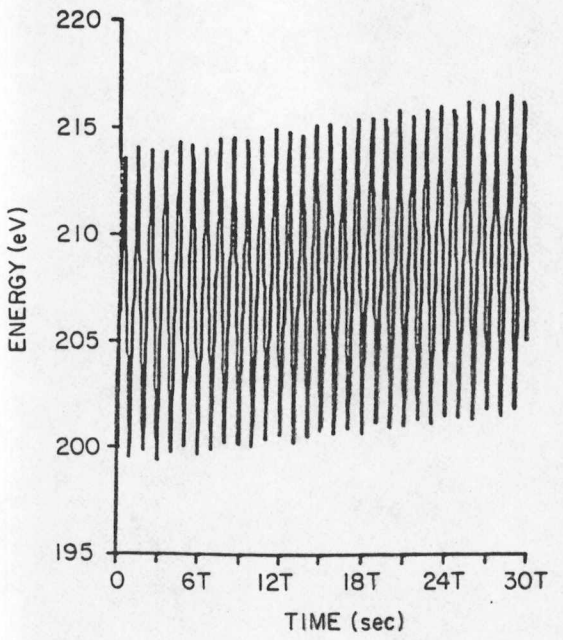

Fig III.3. Perpendicular component of the energy versus time for $\delta = 0.1$, $v_c T = 10$, $E_0 = 300$ eV, and a triangular perturbation.

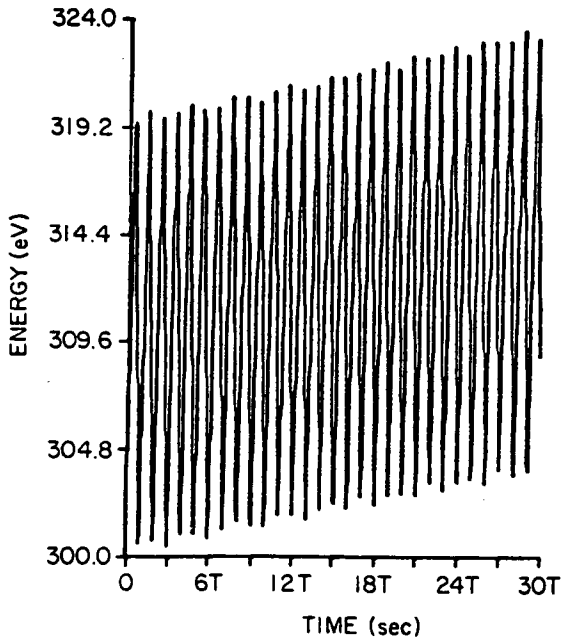

Fig III.4. Total energy versus time for $\delta = 0.1$, $v_c T = 10$, $E_0 = 300$ eV, and a triangular perturbation.

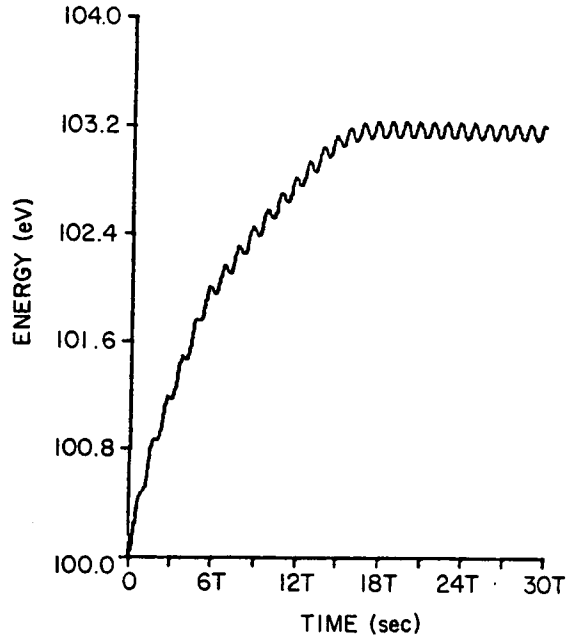

Fig III.5. Parallel component of the energy versus time for $\delta = 0.1$, $v_c T = 0.1$, $E_0 = 300$ eV, and a triangular perturbation.

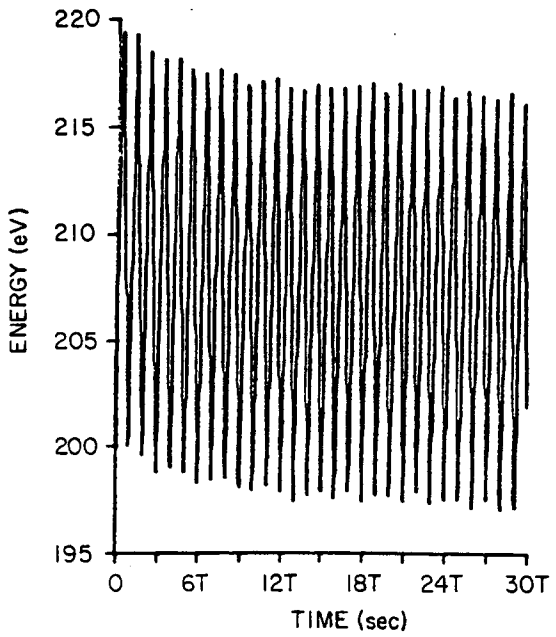

Fig III.6. Perpendicular component of the energy versus time for $\delta = 0.1$, $v_c T = 0.1$, $E_0 = 300$ eV, and a triangular perturbation.

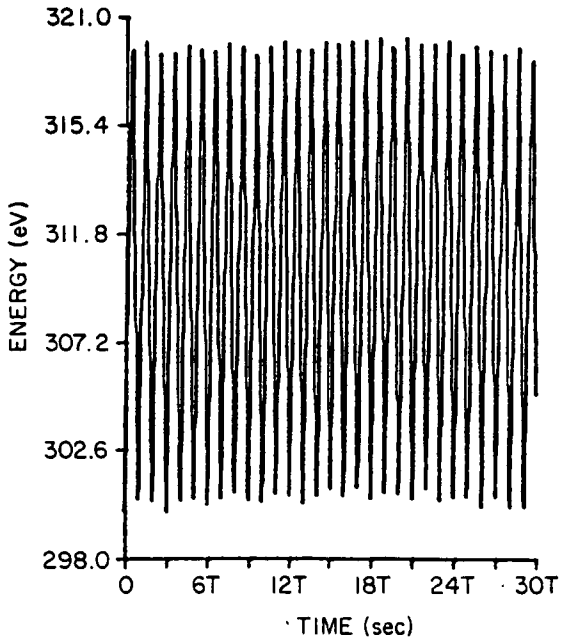

Fig III.7. Total energy versus time for $\delta = 0.1$, $v_c T = 0.1$, $E_0 = 300$ eV, and a triangular perturbation.

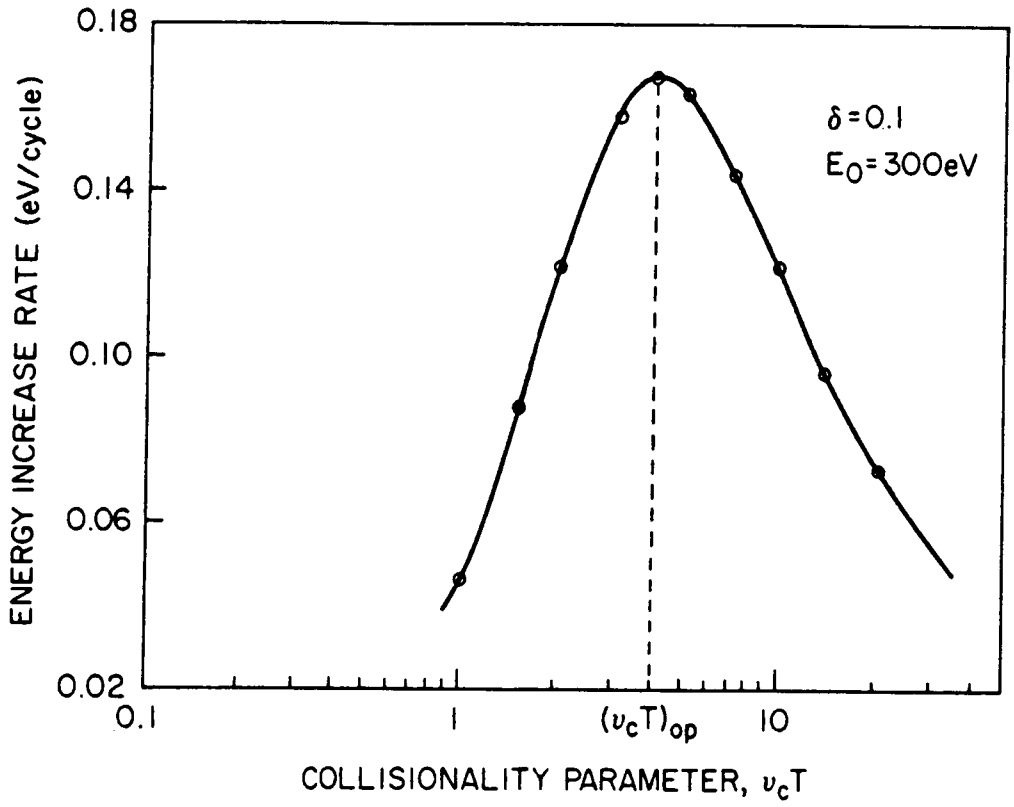

Fig III.8. Energy increase rate versus collisionality parameter for $\delta = 0.1$, $E_0 = 300$ eV, and a triangular perturbation.

increase rate versus collisionality parameter at a field modulation factor of δ = 0.1, and an initial value of the energy of E_0 = 300eV.

The energy increase rate has been plotted against the field modulation factor on a log-log scale for several values of the collisionality parameter. For all values of the collisionality parameter, it has been found that the energy increase rate is proportional to the second power of the field modulation factor. This is illustrated in Fig III.9. The above analysis has been done for several non-zero ramping down times but no quantitative effects on the energy increase rate have been observed.

III.3 Application to a Sinewave

When a sinewave perturbation is applied, results similar to the previous section are obtained. Fig III.10 shows the waveform of the magnetic field assumed.

For a "collisionless" plasma ($\nu_c T$ = 0.2), the total energy of a particle oscillates with the field with only a very small increase in its average value. This is consistent with the lack of energy transfer between the two components of the energy. These results are illustrated in Fig III.11 and Fig III.12. The values of the field modulation factor, δ, and of the initial energy, E_0, are chosen to be respectively 0.1 and 300eV. Fig III.11 shows that after a transient period of about 12T, where T is the period of the driving RF waveform, the parallel component of the energy reaches a plateau at a level less than its initial value.

For a collisional plasma ($\nu_c T$ = 6), Fig III.13 and Fig III.14 show that the average value of the energy increases with time at a rate of about 0.85 eV/cycle.

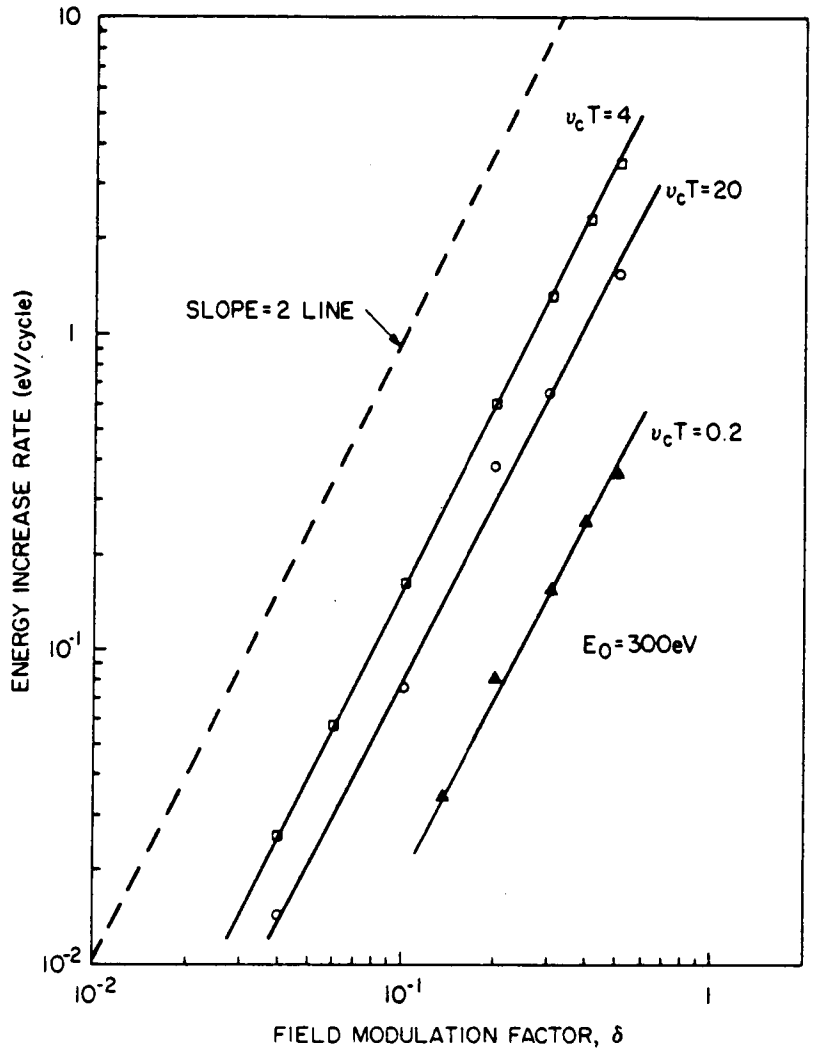

Fig III.9. Energy increase rate versus field modulation factor for E_0 = 300 eV, several collisionality parameters, and a triangular perturbation.

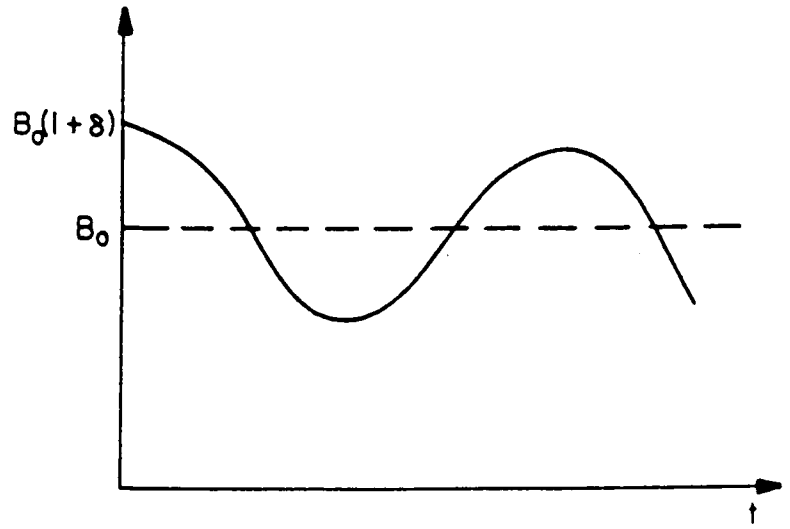

Fig III.10. Magnetic field waveform for a sinusoidal perturbation.

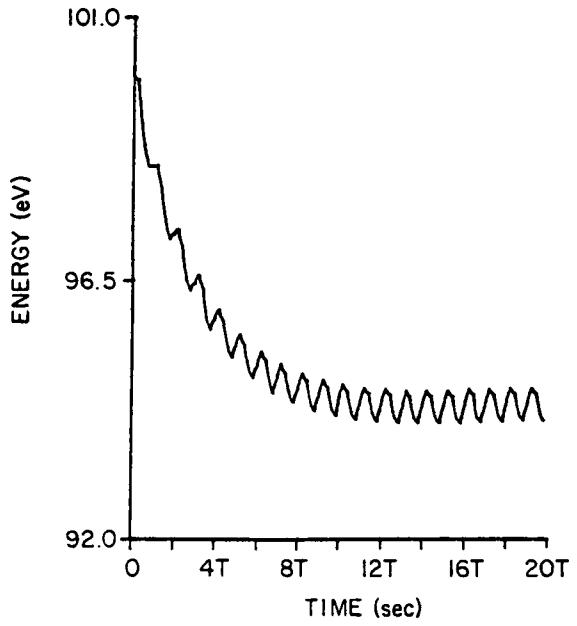

Fig III.11. Parallel component of the energy versus time for $\delta = 0.1$, $v_c T = 0.2$, $E_0 = 300$ eV, and a sinusoidal perturbation.

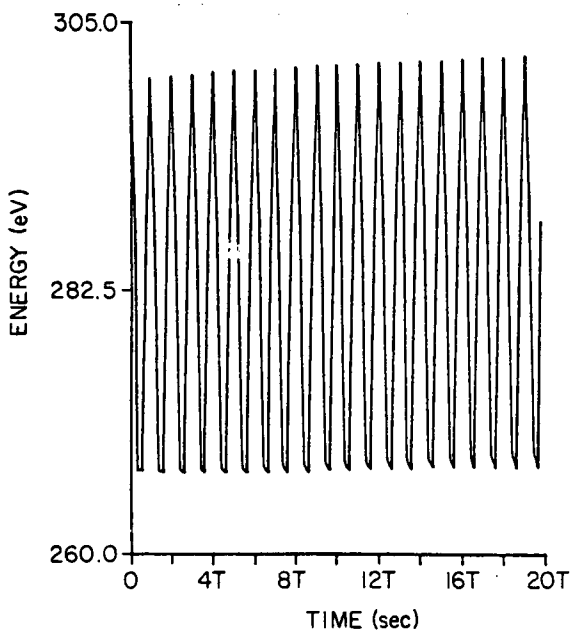

Fig III.12. Total energy versus time for $\delta = 0.1$, $v_c T = 0.2$, $E_0 = 300$ eV, and a sinusoidal perturbation.

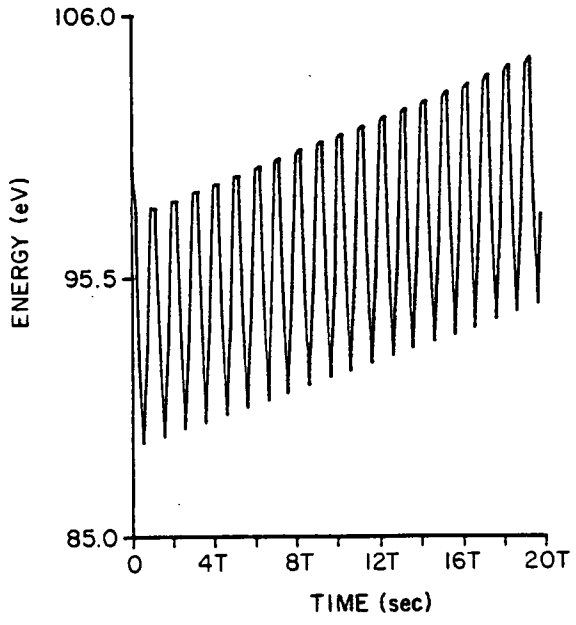

Fig III.13. Parallel component of the energy versus time for $\delta = 0.1$, $v_c T = 6$, $E_0 = 300$ eV, and a sinusoidal perturbation.

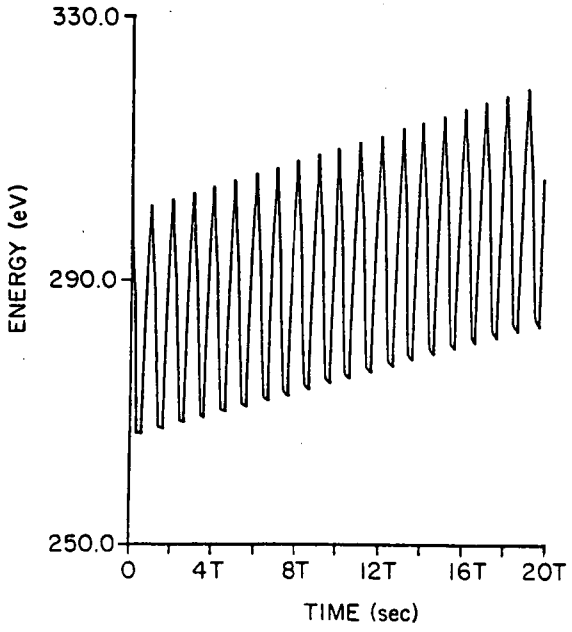

Fig III.14. Total energy versus time for $\delta = 0.1$, $v_c T = 6$, $E_0 = 300$ eV, and a sinusoidal perturbation.

In Fig III.15, the energy increase rate is plotted against the collisionality parameter, $v_c T$, at a field modulation factor of $\delta = 0.1$ and an initial value of the energy of 300eV. The solid dots represent analytical results obtained using Equation (II.62), while the triangles represent the computational results obtained from the energy plots. Both results show good agreement with each other. The energy increase rate has a resonant behavior with a maximum at an optimum value of the collisionality parameter of about 4.2.

Fig III.16 is a plot on a log-log scale, of the energy increase rate as a function of the field modulation factor for several values of the collisionality parameter, and an initial value of the energy of 300eV. A slope of 2 indicates that the energy increase rate is proportional to the second power of the field modulation factor.

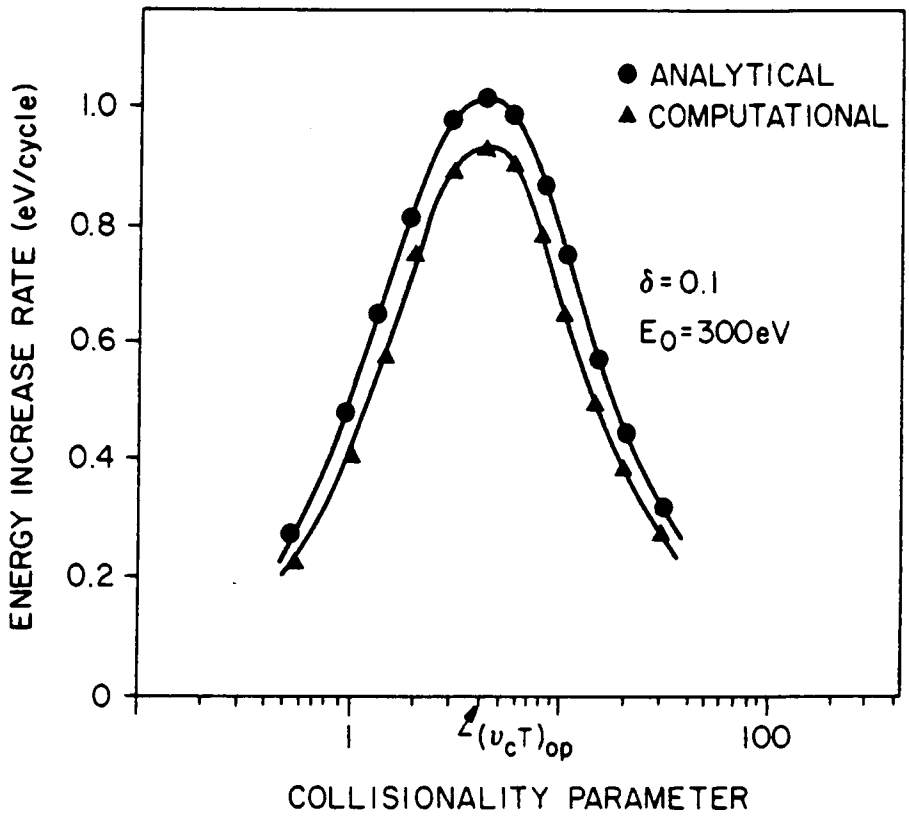

Fig III.15. Energy increase rate versus collisionality parameter for $\delta = 0.1$, $E_0 = 300$ eV, and a sinusoidal perturbation.

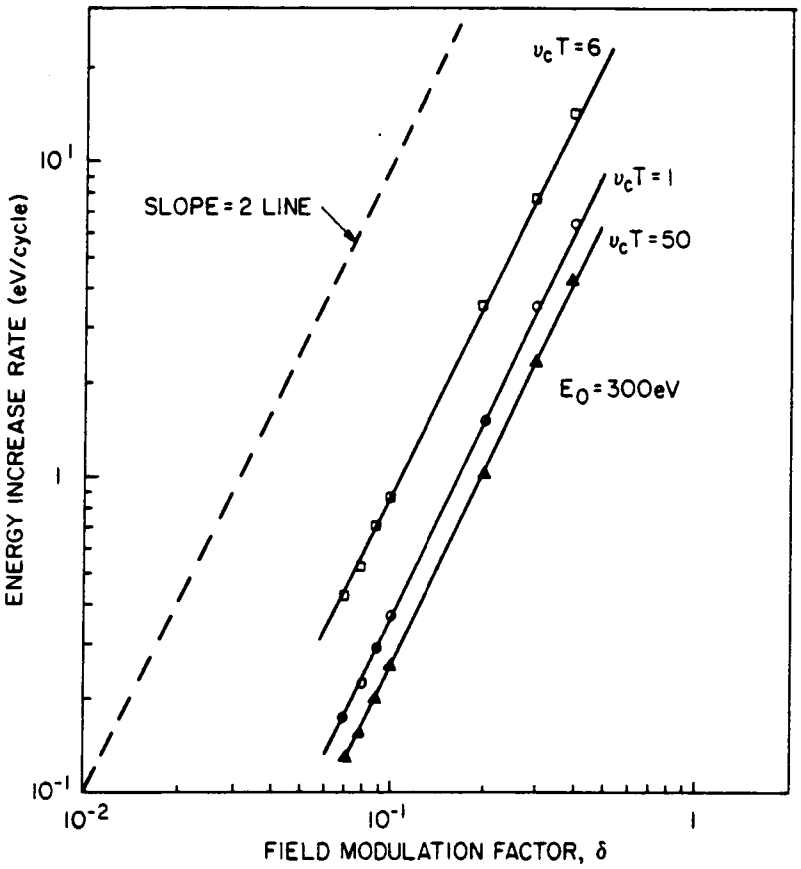

Fig III.16. Energy increase rate versus field modulation factor for E_0 = 300 eV, several collisionality parameters, and a sinusoidal perturbation.

III.4 Application to a Sawtooth Waveform

When a sawtooth perturbation is applied to collisional magnetic pumping, the magnetic field assumes the waveform shown in Fig III.17.

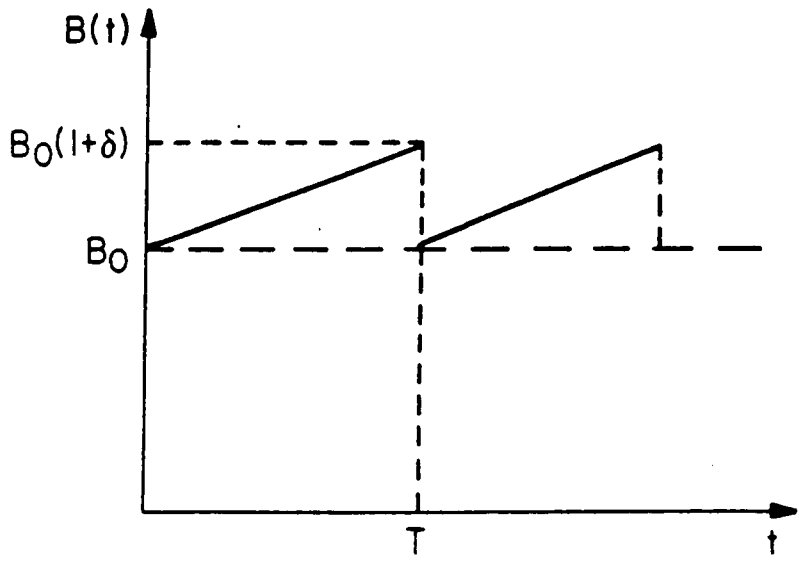

Fig III.17. Magnetic field waveform for a sawtooth perturbation.

Many collisionality regimes have been tried but the energy increase rate was similar for all cases, as predicted by Equation (II.103). Contrary to the triangular waveform case, the energy does not oscillate, but keeps increasing with time, at a rate of 2eV/cycle when a particle of 300eV initial energy and a field modulation factor, δ, of 0.01 are assumed. Fig III.18 through Fig III.20 show the behavior with time of the parallel, perpendicular, and total energy for a collisionless plasma ($\nu_c T = 0.2$). Fig III.21 shows the energy versus time for a collisional plasma ($\nu_c T = 6$).

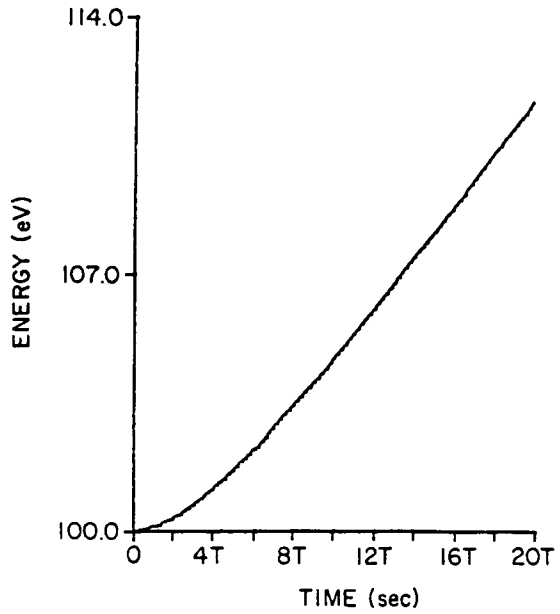

Fig III.18. Parallel component of the energy versus time for $\delta = 0.01$, $v_c T = 0.2$, $E_0 = 300$ eV, and a sawtooth perturbation.

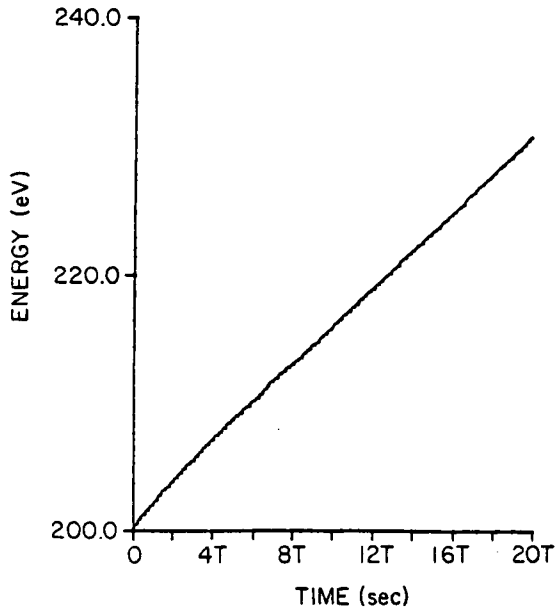

Fig III.19. Perpendicular component of the energy versus time for $\delta = 0.01$, $v_c T = 0.2$, $E_0 = 300$ eV, and a sawtooth perturbation.

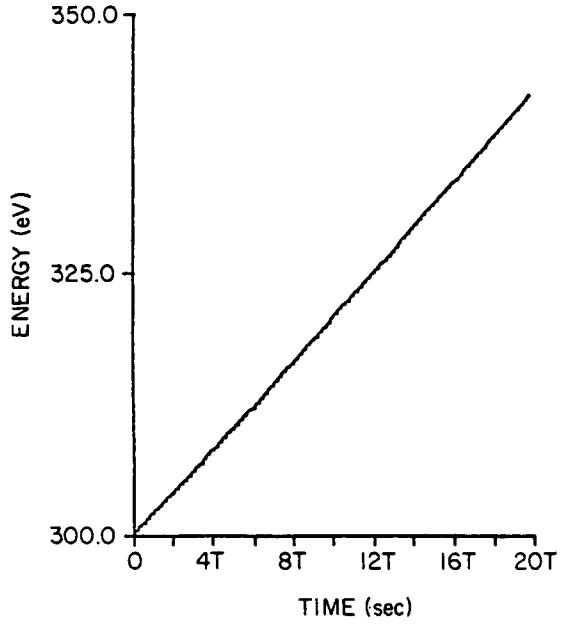

Fig III.20. Total energy versus time for $\delta = 0.01$, $v_c T = 0.2$, $E_0 = 300$ eV, and a sawtooth perturbation.

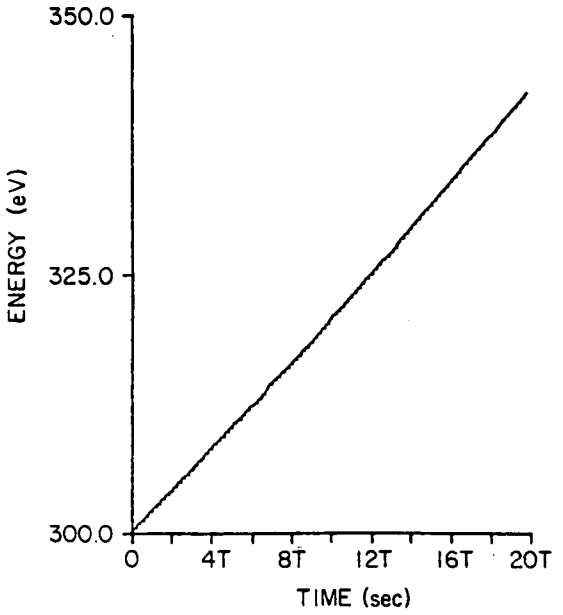

Fig III.21. Total energy versus time for $\delta = 0.01$, $v_c T = 6$, $E_0 = 300$ eV, and a sawtooth perturbation.

The energy increase rate versus the collisonality parameter is plotted in Fig III.22, for a field modulation factor of 0.01 and an initial energy of 300eV. The solid dots represent analytical results obtained using Equation (II.101), and the triangles represent computational results obtained from the energy plots. Both results are in agreement with each other, and confirm the fact that the energy increase rate is independent of the plasma collisionality.

The log-log plot of the energy increase rate versus the field modulation factor, δ, is shown in Fig III.23. It shows that for $\delta \leq 0.15$, the relationship is linear with a slope of 1, but for $\delta > 0.15$ the slope is no longer unity (it is about 2.27). This is consistent with the analytical result of Equation (II.99) which predicts first order heating only for small field modulation factors.

III.5 Conclusion

The above analysis shows that the plasma collisionality plays an important role in the viability of collisional magnetic pumping as a plasma heating method if triangular or sinewave perturbing waveforms are used. It also confirms that to achieve the best heating performance, in these cases, operation at an optimum collisionality is required. The optimum collisionality parameter, $v_c T$, is $4\pi/3$. Outside this interval, the energy increase rate decreases rapidly, leading to a lower heating performance.

The computational analysis shows that the energy increase rate is indeed independent of the collisionality parameter when a sawtooth perturbation is applied. It also confirms that first order heating is achievable for small values of the field modulation factor, less than 0.15. The energy increase rate in this case is many orders of magnitude larger than the one obtained when a sinewave perturbation is used.

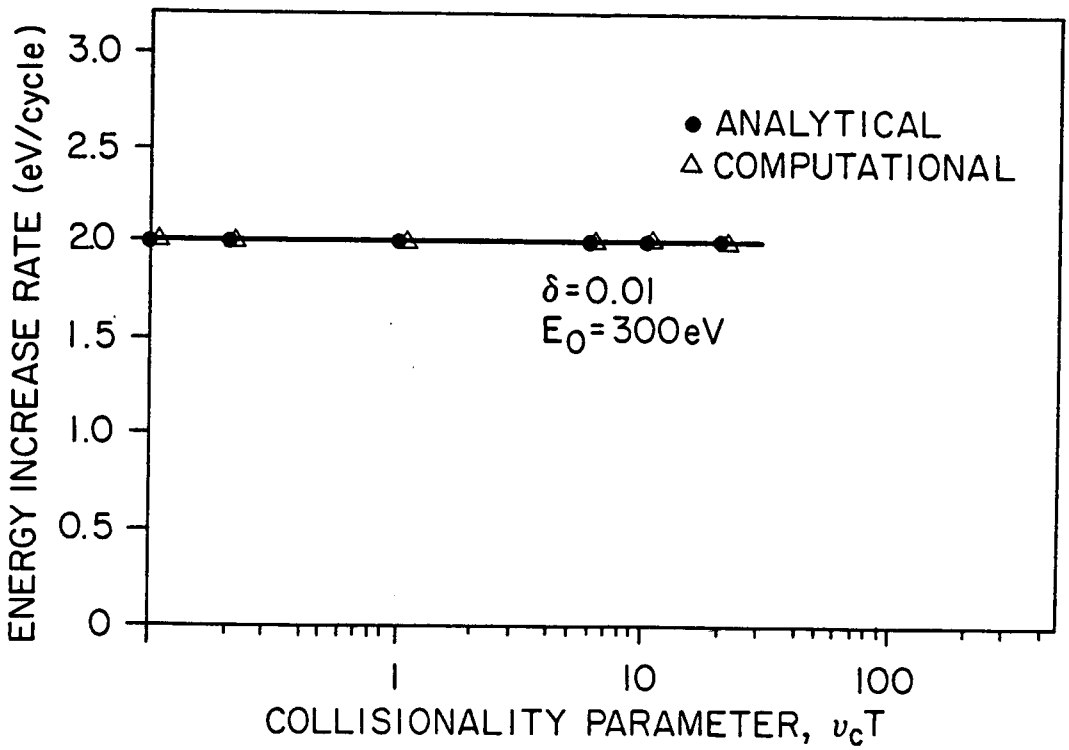

Fig III.22. Energy increase rate versus collisionality parameter for $\delta = 0.01$, $E_0 = 300$ eV, and a sawtooth perturbation.

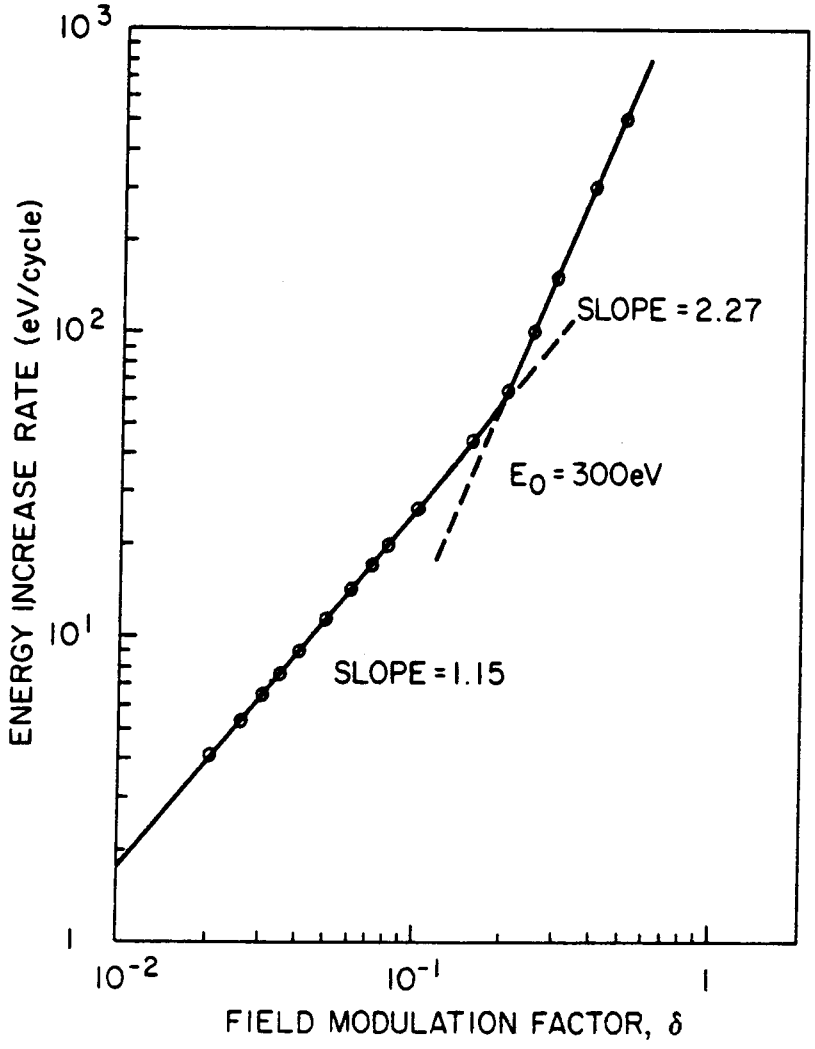

Fig III.23. Energy increase rate versus field modulation factor for E_0 = 300 eV and a sawtooth perturbation.

CHAPTER IV

EXPERIMENTAL APPLICATION OF COLLISIONAL MAGNETIC PUMPING TO A CLASSICAL PENNING DISCHARGE PLASMA

IV.1 Introduction

This chapter contains a description of two different experimental setups designed and used to heat, by collisional magnetic pumping, a cylindrical plasma produced by a classical Penning discharge (a detailed description of this apparatus is presented in Appendix D). A discussion of experimental heating data is also presented.

The material in this chapter is organized in the following way. The first section discusses the design and implementation of the exciter coil. A proper design of this coil is essential due to the presence of high current levels at relatively high frequencies. The second section discusses the design, implementation, and testing of the high Q resonant circuit used to generate a sinusoidal perturbation of the background magnetic field. In the third section, the design, implementation and testing of the circuit generating a sawtooth perturbation is discussed. Finally, in the last section, the heating data collected in the sinusoidal and sawtooth cases is presented and discussed.

IV.2 Design and Implementation of the Exciter Coil

The exciter coil is a solenoid wrapped around the plasma, through which an RF current flows to generate a magnetic perturbation of the background magnetic field. The physical shape and size of the exciter coil is determined by the shape of the vacuum vessel on which it is wound, and by the size of the plasma. The vessel is a straight cylindrical glass tube whose outer diameter is 12.52 cm. The length of the plasma is about 64 cm. A single-layer cylindrical

solenoid 50 cm long, 6.26 cm in radius, and with 8 turns was constructed. The inductance of such a solenoid is given by (Welsby, 1960)

$$L = \frac{4\pi^2 r^2 N^2}{\ell} 10^{-9} H, \qquad \text{(IV.1)}$$

where r, ℓ, and N are respectively the radius in centimeters, the length of the coil in centimeters, and the number of turns. For the chosen dimensions the calculated value of the inductance is L = 1.97 μH.

In the range of frequencies at which the exciter coil is used, one takes into account the skin effect and its influence on the series resistance of the coil. At high frequencies the current in a conductor is mainly confined to a region very close to the surface. The current density reduces exponentially with depth. The distance in which a current I through the conductor is reduced to I/e is defined as the skin depth. This quantity, s, is given by (Terman, 1947) as

$$s = 5033\left(\frac{\rho}{\mu f}\right)^{1/2} \text{cm}, \qquad \text{(IV.2)}$$

where ρ is the resistivity of the conductor in ohm - centimeters, f is the frequency in hertz, and μ is the magnetic permeability of the core material. For a copper conductor and an air-core, Equation (IV.2) is reduced to

$$s = \frac{6.62}{\sqrt{f}} \text{cm}. \qquad \text{(IV.3)}$$

As the effective thickness of the current-carrying conductor is reduced, due to the skin effect, the effective resistance of the coil increases. This is also aggravated by the fact that adjacent turns influence each other's current density distribution, which leads to a further increase of the series resistance. This is known as the proximity effect. An expression for the effective resistance of a coil which accounts for the above effects is given by (Welsby, 1960)

$$R = \frac{1}{4} R_{dc} \left(1 + \frac{u}{2} \frac{d^2}{c^2}\right) \frac{d}{s}, \qquad \text{(IV.4)}$$

where R_{dc} is the value of the resistance at 0 Hz, d is the thickness of the conductor, s is the skin depth, c is the separation between the midlines of two neighboring turns, and u is a numerical factor.

An important factor that limits the frequency range over which a solenoid can be used in a resonant circuit is the distributed capacitance. This capacitance is the sum of small capacitances existing between adjacent turns, non adjacent turns, and between the terminal leads. Empirical curves giving the self-capacitance of a solenoid versus its physical dimensions can be found in standard sources (Welsby, 1960).

Taking into account the above considerations, the solenoid is constructed from a 0.1 mm thick sheet of copper cut into a 3.6 m long and 6 cm wide strip. As already mentioned, the solenoid is 50 cm long and has 8 turns. The measured inductance of the solenoid with its termination leads is L = 2.6 μH. The effective series resistance at 3 MHz is calculated to be R = 0.01 Ω. The shunt capacitance is C = 11pF, which restricts the coil to resonant frequencies below 29 MHz. A Faraday shield connected to ground is introduced between the exciter coil and the plasma to short out the electric field of the RF wave and allow only the magnetic field to pass through.

IV.3 Design, Implementation, and Testing of the High Q Resonant Circuit

The magnetic field inside an infinitely long solenoid has its direction along the axis and a magnitude given by

$$B = \mu N I, \qquad \text{(IV.5)}$$

where μ is the permeability of the core material, N is the number of turns per meter and I is the magnitude of the electric current flowing through the conductor. Since μ and N are fixed parameters in our application, the only way to get an appreciable magnetic field strength is to generate a relatively high RF current. This can be achieved using a tunable high Q parallel resonant circuit. At a selected resonance frequency, such a circuit acts as a current amplifier by establishing a current through the inductor equal to Q times the current furnished by the sinusoidal source. This is illustrated in Fig IV.1.

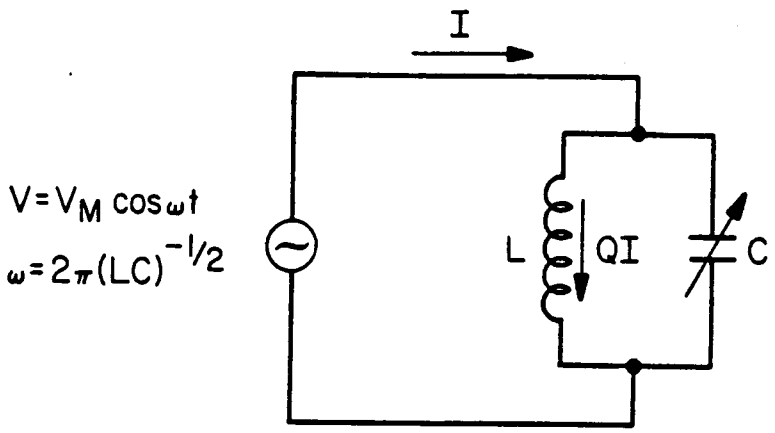

Fig IV.1. L-C parallel resonant circuit driven by a sinusoidal source.

The capacitor used to form the resonant circuit is a tunable vacuum capacitor that can be varied between 31pF-9nF and is able to withstand up to 7.5 kV. A quality factor, Q, of 350 at about 2.5 MHz has been measured. Fig IV.2 through Fig IV.4 show the logarithmic amplitude, the real part, and the imaginary part of the impedance of the circuit as seen by the source, versus frequency. At the resonance frequency, the magnitude of the impedance seen by the power source is Q times larger than the inductor impedance. So for

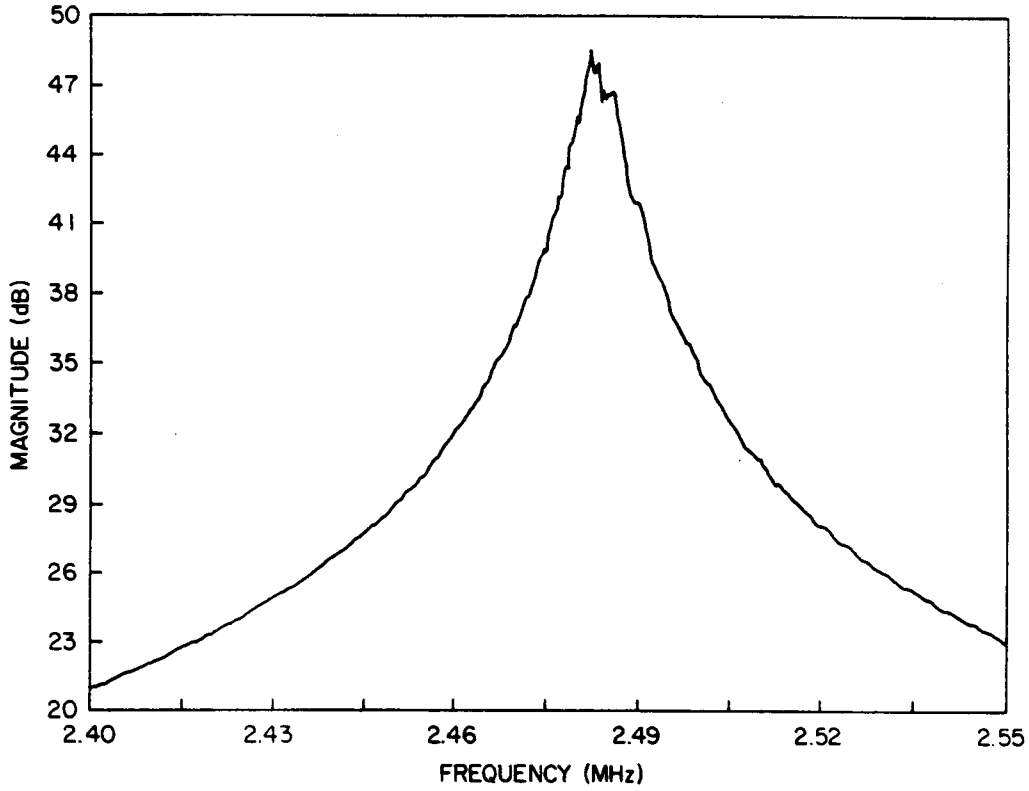

Fig IV.2. Logarithmic magnitude of the impedance versus frequency.

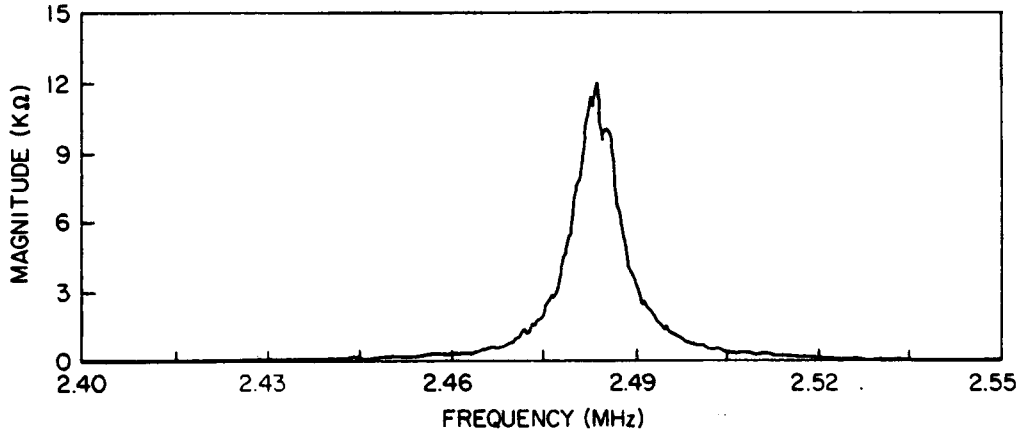

Fig IV.3. Magnitude of the real part of the impedance versus frequency.

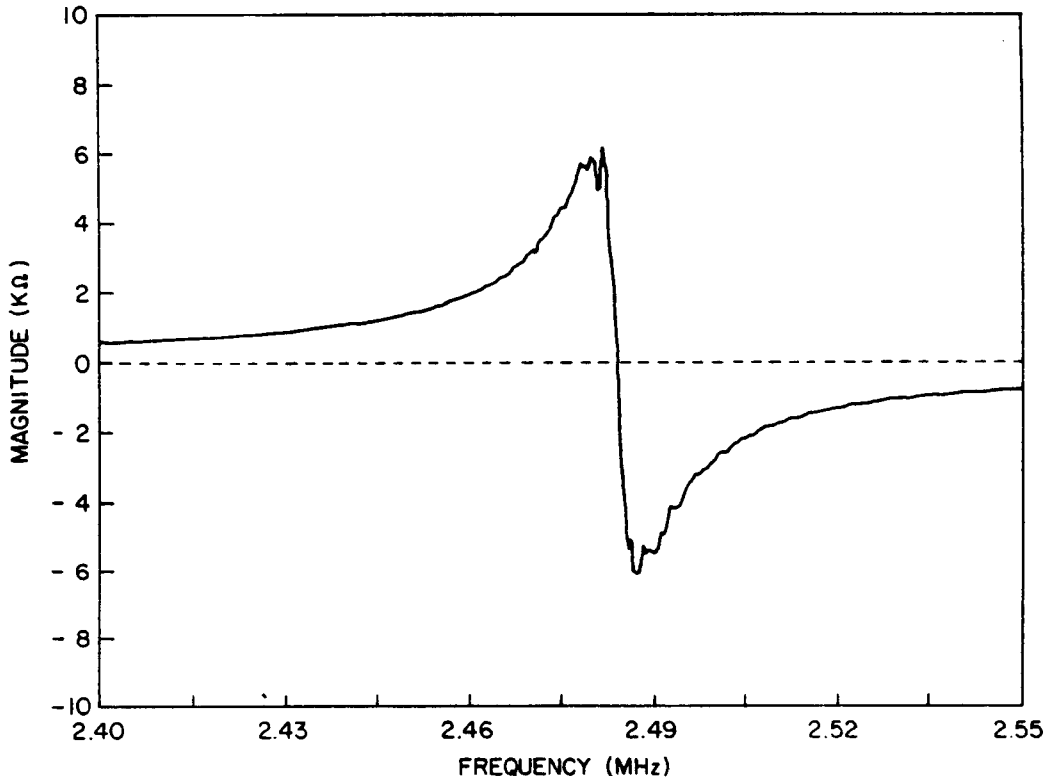

Fig IV.4. Magnitude of the imaginary part of the impedance versus frequency.

maximum power transfer, an impedance matching transformer has been fabricated and inserted between the resonant circuit and the source, which has a 50Ω output impedance. The sinusoidal source used is the frequency-swept output of an HP 3577A network analyzer, which at the same time monitors the characteristics of the resonant circuit such as impedance, reflection ratio, etc. The HP 3577A network analyzer is an instrument capable of measuring the transfer function of any network and furnishing its magnitude and phase plots. The network analyzer operates over the 5 Hz-200 MHz frequency range. The signal out of the network analyzer is fed to a 100L Amplifier Research power amplifier. The 100L has a flat frequency response in the frequency range 10 kHz- 220 MHz and is capable of furnishing up to 100 watts of power. The signal thus amplified is fed to the impedance matching transformer, and ultimately to the L-C resonant circuit, through a DC 2000 dual directional coupler. Fig IV.5 shows the experimental setup described above. Currents up to 40 amperes peak to peak have been achieved. This implies that an 8 G (0.0008 Tesla) peak-to-peak perturbation can be superimposed on the background magnetic field, typical value of which is B_o = 450 G (0.045 Tesla).

IV.4 Design, Implementation, and Testing of the MOS Switching Circuit

The principle behind generating a sawtooth-shaped current through an inductor is taken from the nature of the relationship between the current and voltage across it,

$$V = L \frac{dI}{dt}. \qquad \text{(IV.6)}$$

Integrating (IV.6) and solving for the current we get

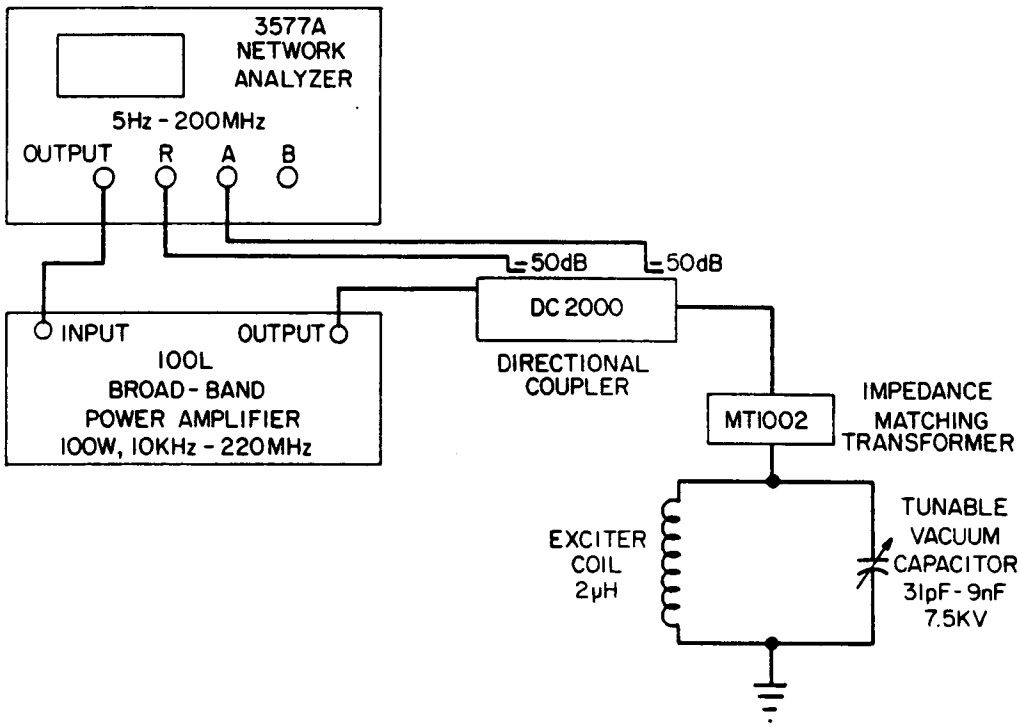

Fig IV.5. Experimental setup for generating a sinusoidal perturbation.

$$I(t) = \frac{1}{L} \int_{-\infty}^{t} V(t)\,dt. \qquad \text{(IV.7)}$$

If V(t) is a constant, Equation (IV.7) can be written as

$$I(t) = \frac{E}{L} t + I_0. \qquad \text{(IV.8)}$$

wehre I_0 is the inital value of the current, and E is a constant. An obvious approach to produce a linear current-time relationship would be to connect an inductor across an ideal DC voltage source. This is shown in Fig IV.6.

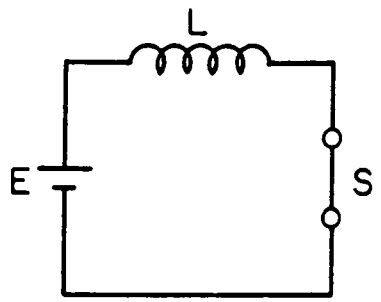

Fig IV.6. Ideal DC voltage source driving an inductor.

If the switch S opens, the current through the inductor would vanish, and a sawtooth shaped current would be generated if the switch S would periodically open and close. The only flaw in the above analysis is that a current through an inductor cannot vanish instantaneously without inducing high transient voltages that would damage the switch (this is also due to the nature of the current-voltage relationship for an inductor). The solution to the above problem is simple and consists of offering a path other than the switch, through which the current can flow and damp out. Fig IV.7 shows a circuit achieving such a configuration.

Let's assume that the switch is closed from t = 0 to t = t_0 and open from t = t_0 to t = t_1, then the current through the inductor satisfies the following equations

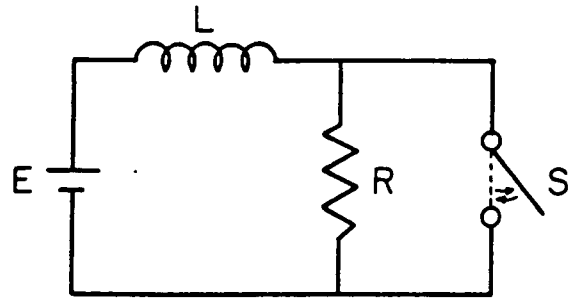

Fig IV.7. Ideal DC voltage source driving an inductor with a damping resistor.

$$I_L(t) = \frac{E}{L} t + I_0 \qquad 0 \le t \le t_0, \tag{IV.9}$$

and

$$I_L(t) = \left(I(t_0) - \frac{E}{R} \right) e^{-\frac{R}{L}(t - t_0)} + \frac{E}{R} \qquad t_0 \le t \le t_1, \tag{IV.10}$$

Fig IV.8 is a schematic drawing of the switch control voltage and the respective current waveform. To approach a sawtooth waveform the following condition has to be satisfied

$$\frac{L}{R} < (T - t_R) << t_R. \tag{IV.11}$$

To accomplish a sawtooth perturbation superimposed on the background magnetic field, a circuit equivalent to Fig IV.7 has been designed, constructed, and tested. The inductor is the exiter coil, the constant voltage source is a Lambda DC regulated power supply, and the switch is a Motorola TMOS 2N6770 transistor. The selection of this transistor is based on its high voltage standoff (500 V), low series on resistance (0.4 Ω), high switching speed (80 ns turn-on time and 220 ns turn-off time), and high current capabilities (25 A in pulsed mode). Because of their positive temperature coefficient, these devices tend to share currents in a balanced fashion permitting themselves to be easily paralleled. This is advantageous if high current levels are to be used.

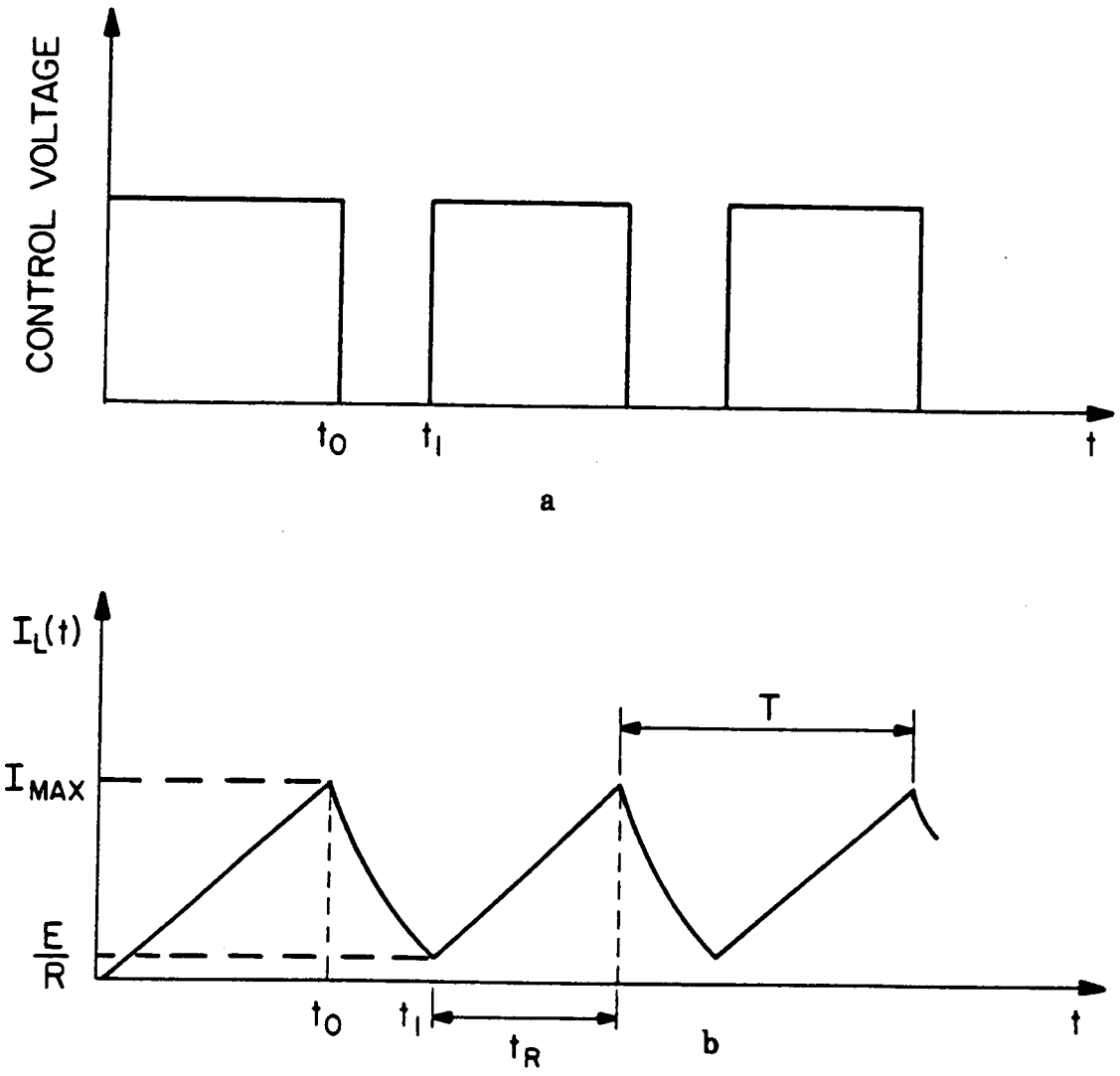

Fig IV.8 a) Switch control voltage; b) Current waveform.

Fig IV.9 is a schematic diagram of the circuit actually used to generate the sawtooth-shaped current through the exciter coil. This circuit consists of two parts, the switching arm and the driving stage. The switching arm consists of the DC power source, the exciter coil, the switch (Transistor T_1), and the damping resistor R. It is through this arm that the current ramps up and damps out periodically. The driving stage is the part of the circuit which provides the periodic nature of the current waveform, its frequency, and its amplitude.

The operation of the driving stage is quite simple. It consists of a control signal fed into a current buffer which drives two complementary MOS switches. When the control signal is low, transistor T_2 (MTP 8P10) is on and transistor T_3 (IRF 510) is off. This automatically puts 10 volts between the gate and the source of transistor T_1, consequently turning it on. Fig IV.10 illustrates the state of each transistor during this regime. As soon as T_1 turns on, the current starts ramping up through the inductor until the control voltage changes state, at which time the current reaches its maximum value. As the control voltage goes high, T_2 turns off, T_3 turns on, consequently grounding the gate of T_1 and turning it off. At this time, the current stops flowing through the transistor and starts flowing through the damping resistor R. Fig IV.11 illustrates the state of each transistor during this regime.

Transistors T_2 and T_3 work in an on-off basis. They are needed to allow the input capacitance of T_1 (3000pF) to charge up and discharge through a very low resistance (0.5 Ω). This is essential if high speed switching is to be achieved. The current buffer (CD4050) is introduced between the control

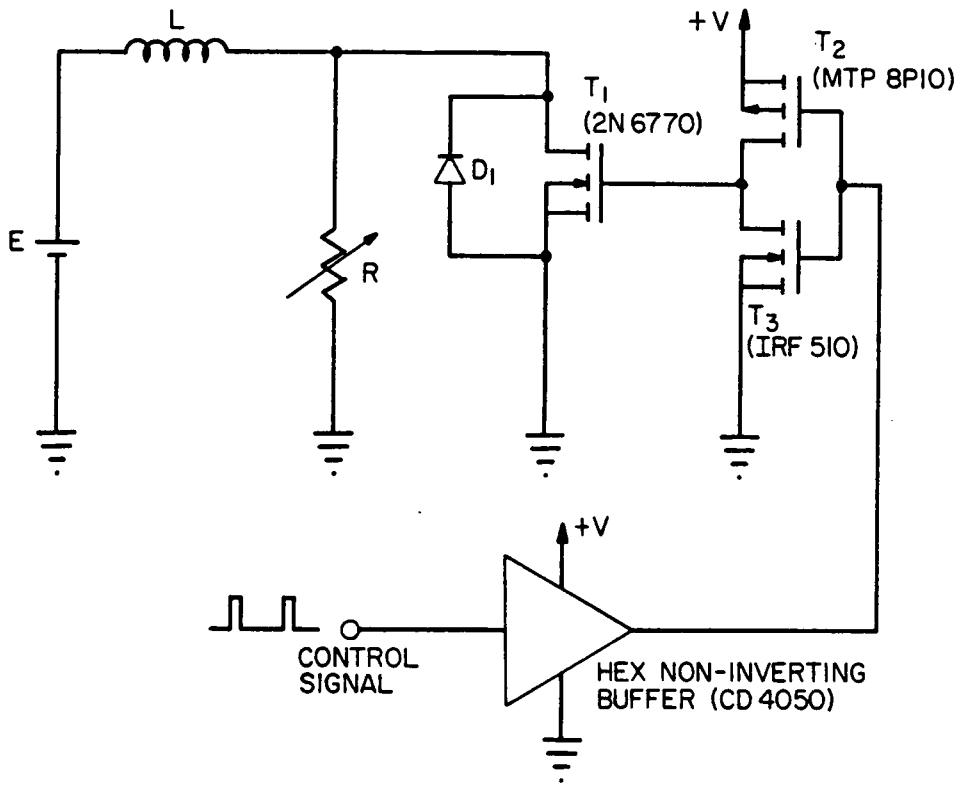

Fig IV.9. Circuit generating a periodic current sawtooth through the exciter coil.

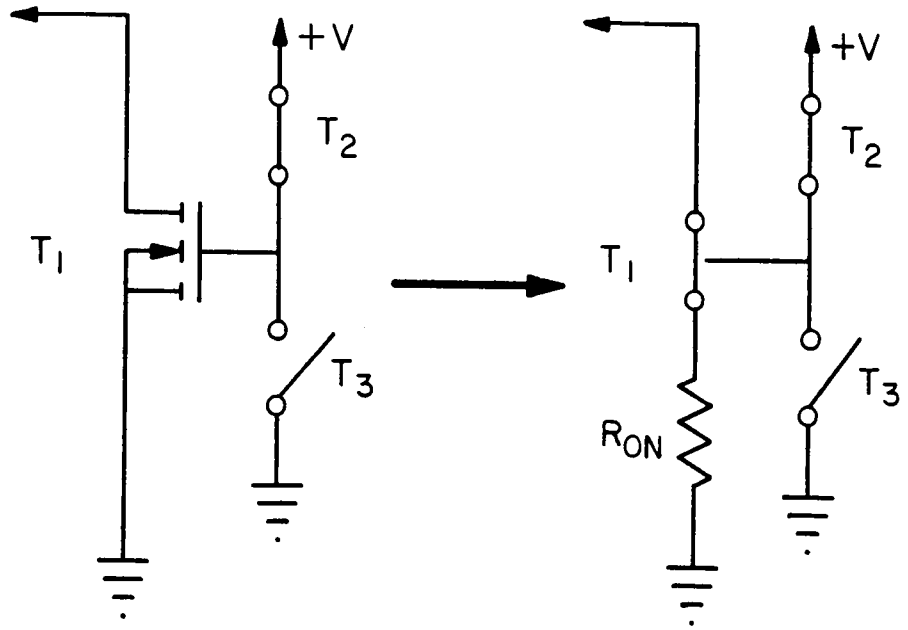

Fig IV.10. State of the transistors when the switch is on.

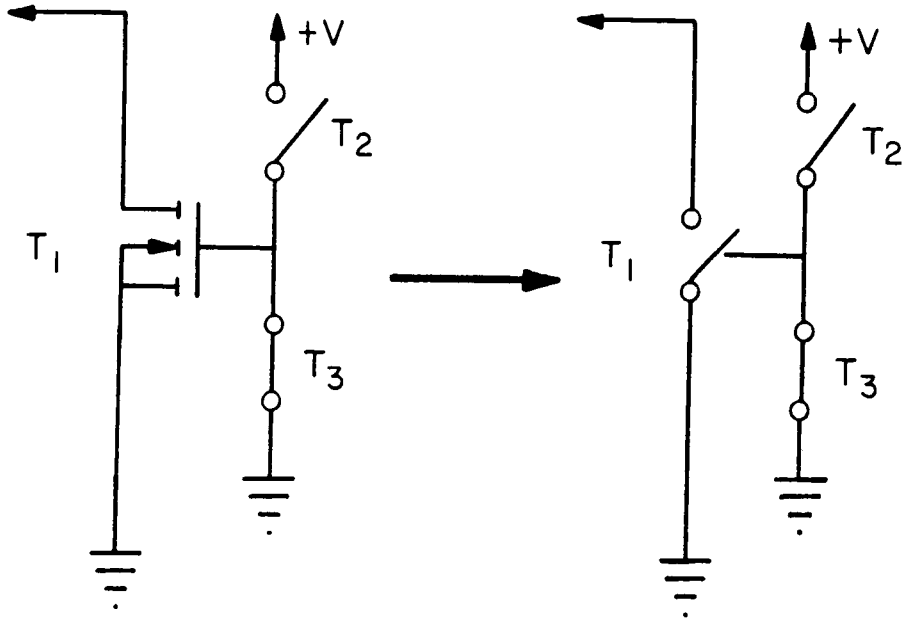

Fig IV.11. State of the transistors when the switch is off.

signal and the gates of T_2 and T_3 to help provide sufficient current at the switching times.

The maximum value of the current is determined by the duty cycle of the control signal and magnitude of the DC voltage delivered by the power source. The minimum time alloted for the current to damp out is determined by the sum of all the response times of the devices involved. This sets a limit on the maximum value of the duty cycle, and consequently on the maximum value of the time constant L/R. This time constant should be at last 3 times smaller than the time during which transistor T_1 is off. This condition, along with the maximum voltage restriction across T_1 permits the selection of resistor R. Currents up to 25 amperes and driving frequencies up to 200 kilohertz have been achieved.

IV.5 Experimental Data Analysis

IV.5.1 Second order heating data

To study second order heating experimentally a sinewave perturbation is applied to the background magnetic field. The magnitude of this perturbation can be varied up to 8 G peak to peak, which yields a maximum field modulation factor of $\delta = 0.01$ for a background magnetic field of $B_0 = 400$ G.

The first experimental step is to check if the RF magnetic field penetrates the plasma. Theoretically, the MHD skin depth of a collisional plasma is given by (Heald and Wharton, 1978)

$$s = \left(\frac{2 v_c c^2}{v_{pe}^2 v} \right)^{1/2}, \qquad \text{(IV.12)}$$

where ν_c, ν_{pe}, ν, and c are respectively the collision frequency, the electron plasma frequency, the RF driving frequency, and the speed of light. Plugging typical values into Equation (IV.12), skin depths between 20 cm and 1 m are found. This is an indication that the RF magnetic field should be able to penetrate the plasma, whose diameter is about 10 cm, without attenuation. This has been checked experimentally by inserting a B-probe and comparing the output signal when the plasma is on and off. No substantial attenuation has been observed.

The second step undertaken is to make sure that only the magnetic component of the RF wave penetrates the plasma. This is ensured by inserting a Faraday shield between the exciter coil and the plasma. This Faraday shield is made out of a 0.12 mm thick sheet of copper wrapped around the vacuum vessel. A 0.5 cm open axial slit along the entire length of the shield is cut to eliminate any closed circular path for RF currents induced in the shield. This allows the magnetic component of the RF wave to pass through to the plasma. The Faraday shield is then grounded. An interesting fact worth mentioning at this point is that if no Faraday shield is used (or if the shield is not grounded), an RF plasma can be generated. If the DC discharge is turned on along with the RF circuitry, an enhancement or damping of the background electrostatic turbulence is observed. This is an important observation and of use to turbulence studies, since researchers are interested in manipulating the level of turbulence either to study it or to eliminate it and consequently minimize any chaotic plasma behavior.

The diagnostic instruments used to measure the change in energy of the particles due to collisional magnetic pumping are a Langmuir probe, inserted axially into the plasma; a retarding potential energy analyser, positioned at

one end of the vessel with its axis aligned with the cathode axis; and a network analyser. The Langmuir probe is used to measure the electron kinetic temperature and density. The retarding potential energy analyser monitors the energy distribution of the ions escaping out the end. The network analyser monitors the S-parameters of the RF circuit.

As expected, no appreciable change in the energy of the ions or electrons have been observed. The effect of collisional magnetic pumping with a sinusoidal waveform on the plasma characteristics have been too small to observe. Fig IV.12 shows that the electron kinetic temperature has hardly changed for any value of the field modulation factor, δ. Fig IV.13 and Fig IV.14 show that the energy distribution of the ions is virtually the same with or without pumping. Finally Fig IV.15 shows that the reflection ratio coefficient (converted into impedance) has not changed. This means that negligible energy absorption has occured.

The above observations agree with the theoretical predictions. The maximum energy increase rate for second order heating is given by

$$\frac{dE}{dt} = \frac{\delta^2 \nu_c}{12} E_o. \qquad \text{(IV.13)}$$

For $\delta = 0.01$, $\nu_c = 10$ MHz, and $E_o = 10$ eV, the maximum energy increase rate is

$$\frac{dE}{dt} = 833 \text{ eV/s}.$$

The electron containment time is given by

$$\tau_c = \frac{en_e V_p}{I_A}, \qquad \text{(IV.14)}$$

where n_e, V_p and I_A are respectively the electron density, the plasma volume, and the discharge current. A typical value of τ_c is 100 μs. This leads to an

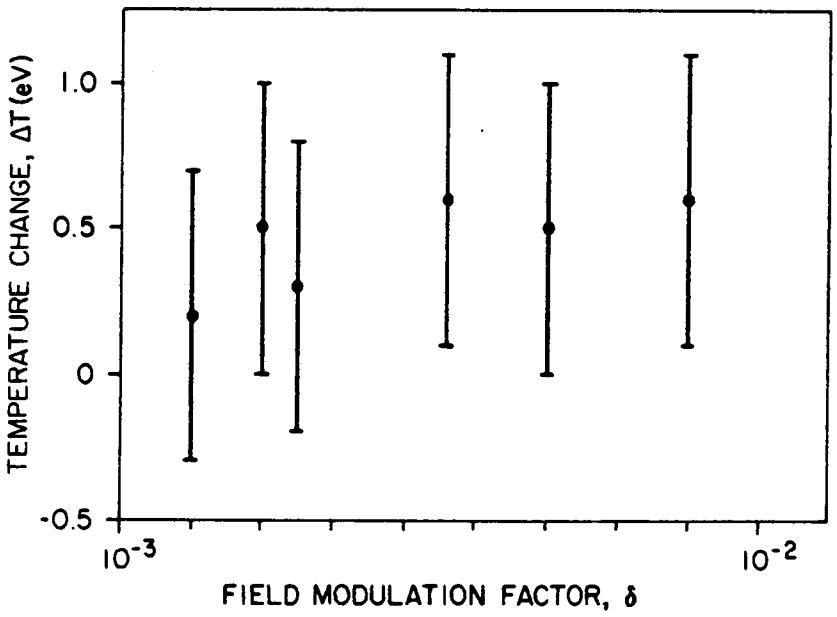

Fig IV.12. Electron kinetic temperature increase versus field modulation factor for a sinewave perturbation.

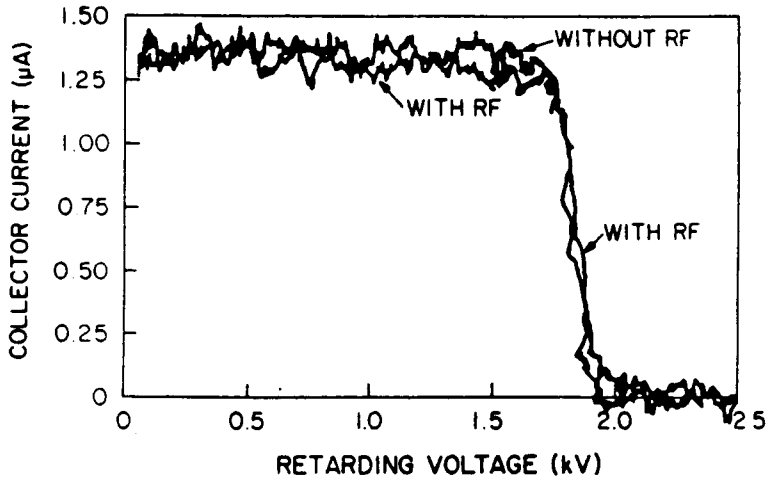

Fig IV.13. Ion energy distribution with and without magnetic pumping for V_A = 1.9 kV, I_A = 12 mA, P = 60 μ Torr, δ = 0.002, and a sinusoidal perturbation.

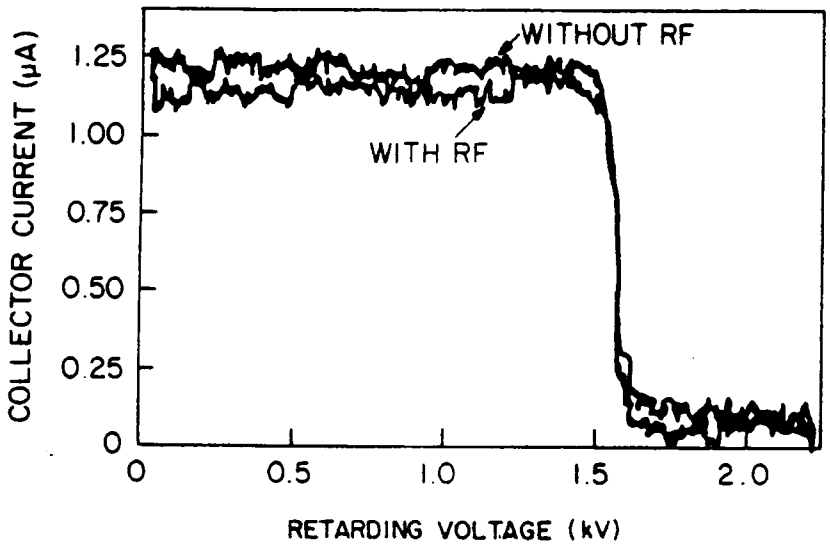

Fig IV.14. Ion energy distribution with and without magnetic pumping for V_A = 1.6 kV, I_A = 18 mA, P = 66 μ Torr, δ = 0.003, and a sinusoidal perturbation.

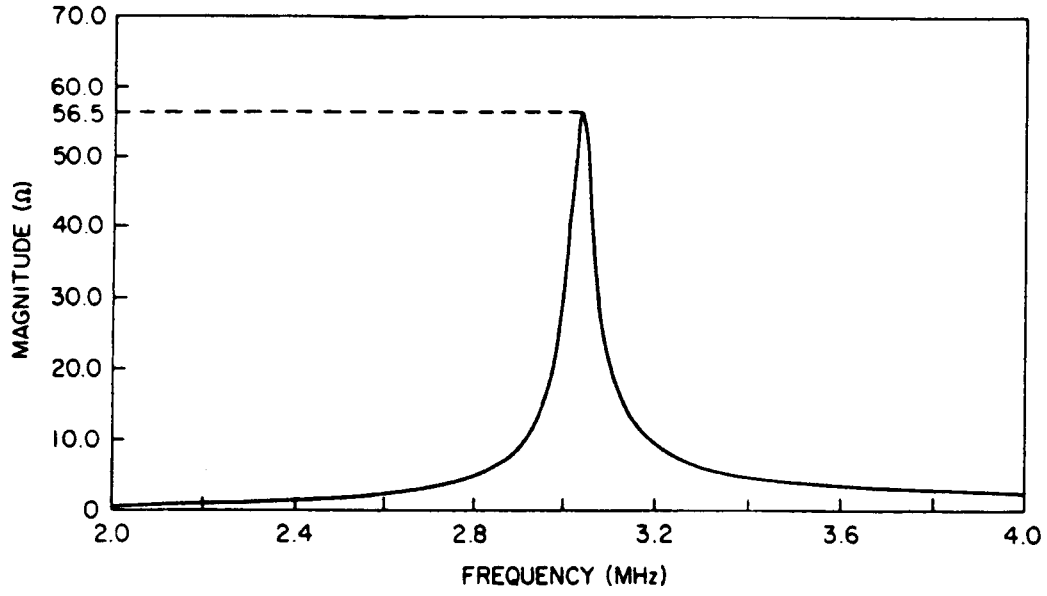

a

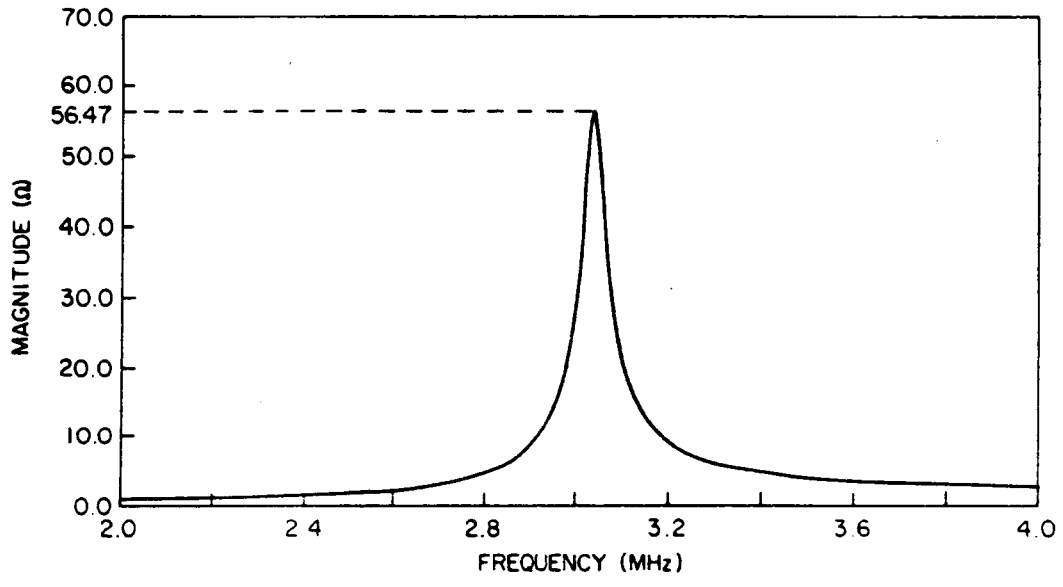

b

Fig IV.15. a) Reflection coefficient converted into impedance when plasma is off; b) Reflection coefficient converted into impedance when plasma is on.

increase in electron energy of

$$\Delta E = 0.083\,eV.$$

The above energy increase is only about 0.83 percent of the initial energy value. The ions' dwell time under the heating region is typically 2 μs. The maximum energy increase rate for an ion with an initial energy of 1000eV is

$$\frac{dE}{dt} = 833\,10^4\,eV/s,$$

which gives

$$\Delta E = 0.166\,eV.$$

The above energy increase is only 0.016 percent of the initial energy value. From the above results, it is seen that for an open-ended apparatus, like the classical Penning discharge, where the containment time is very small, and at the RF power level available for this experimental attempt, it is extremely difficult to observe changes in the energy of the particles due to second order heating by collisional magnetic pumping.

IV.5.2 First order heating data

To achieve first order heating a sawtooth perturbation is superimposed on the background magnetic field. This is done by using the switching circuit shown in Fig IV.9. The DC source used is capable of delivering up to 80 A. The selected voltage is 5 V. The damping resistor, R, is chosen to be 25 Ω. The total inductance of the circuit, including the inductance of the exciter coil and of all the leads, amounts to 6 μH. The response time of the circuit during the on regime is 365 ns and during the off regime is 620 ns. For a proper operation, the current ramp-up time should be many times larger than the turn-on time. The time alloted for the current to decrease to a small value should be much larger than the time constant, L/R, which is about 200 ns. The

above considerations require that an operating frequency less than a few hundreds of kilohertz be used if any substantial perturbation is to be applied. This is good performance, considering that currents of many amperes are switched on and off in a few microseconds through an inductor. Fig IV.16 and Fig IV.17 show the control signal and current waveforms achieved at various operating frequencies

The power generated by the switching circuit can be calculated as follows. During the current ramp-up time, between $t = 0$ and $t = t_o$, the voltage across the exciter coil is constant and equal to E, and the current is given by

$$i(t) = \frac{E}{L}t \qquad o \le t \le t_o. \tag{IV.15}$$

The energy stored in the inductor during this period is

$$W = \int_o^{t_o} V(t)\, i(t)\, dt \tag{IV.16}$$

Plugging the expresions of V(t) and i(t) in Equation (IV.16) yields

$$W = \int_o^{t_o} \frac{E^2}{L} t\, dt, \tag{IV.17}$$

which gives

$$W = \frac{E^2}{2L} t_o^2. \tag{IV.18}$$

The power is given by

$$P = \frac{W}{t_o} = \frac{E^2}{2L}\, t_o. \tag{IV.19}$$

The power stored in the inductor is then damped in resistor R between $t = t_o$ and $t = T$. This can be checked as follows. The energy damped in resistor R is given by

$$W = \int_o^T V_R(t)\, i_R(t)\, dt, \tag{IV.20}$$

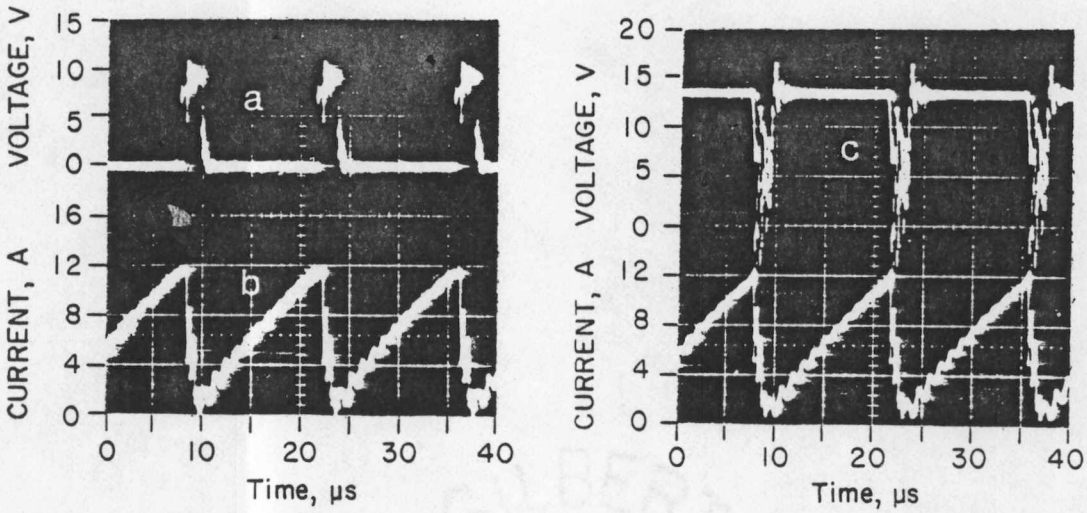

Fig IV.16. a) Scope trace of the control signal with 5 μs/division on the horizontal axis (f = 75 KHz) and 5 volts/division on the vertical axis; b) Current trace with 5 μs/division horizontally and 4 amperes/division vertically; c) Gate voltage trace with 5 μs/division horizontally and 5 volts/division vertically.

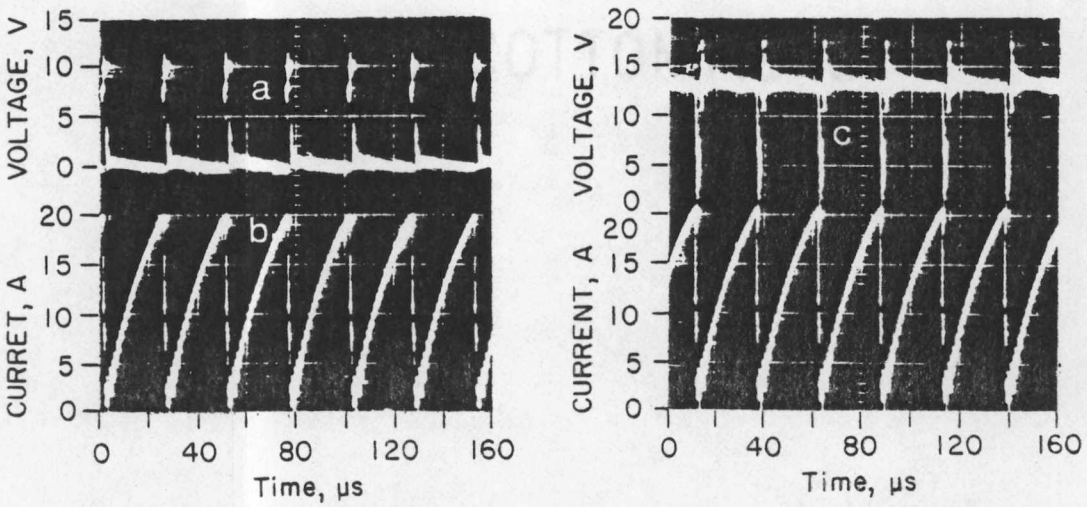

Fig IV.17. a) Scope trace of the control signal with 20 μs/division on the horizontal axis (f = 40 kHz) and 5 volts/division on the vertical axis; b) Current trace with 20 μs/division horizontally and 5 amperes/division vertically; c) Gate voltage trace with 20 μs/division horizontally and 5 volts/division vertically.

where $V_R(t)$ and $i_R(t)$ are given by

$$V_R(t) = o \qquad o \le t < t_o,$$

$$V_R(t) = \left(\frac{RE}{L} t_o - E \right) e^{-\frac{R}{L}(t - t_o)} + E \quad t_o \le t \le T \tag{IV.21}$$

and

$$i_R(t) = o \qquad o \le t < t_o,$$

$$i_R(t) = \left(\frac{E}{L} t_o - \frac{E}{R} \right) e^{-\frac{R}{L}(t - t_o)} + \frac{E}{R} \quad t_o \le t \le T \tag{IV.22}$$

Plugging into Equation (IV.20) and assuming that $T - t_o >> L/R$ gives

$$W \approx \frac{E^2}{2L} t_o^2 + \frac{E^2}{R} T - \frac{3}{2} \frac{E^2}{R^2} L. \tag{IV.23}$$

The power is given by

$$P = \frac{W}{T} \approx \frac{E^2}{2L} t_o + \frac{E^2}{R} - \frac{3}{2} \frac{E^2}{R^2} \frac{L}{T}, \tag{IV.24}$$

but since $T >> L/R$, Equation (IV.24) can be written as

$$P \approx \frac{E^2}{2L} t_o + \frac{E^2}{R} \tag{IV.25}$$

This is in agreement with Equation (IV.19). At an operating frequency of 100 kHz, a power of about 48 watts is generated by the RF circuit. This RF power is comparable to the DC power needed to run the gas discharge to which collisional magnetic pumping is applied.

The diagnostic instruments used to observe the changes in the plasma characteristics are, as in the last subsection, a Langmuir probe and a retarding potential energy analyser. The power absorption is checked by monitoring the change in the RF power as compared to the change of the discharge power when collisonal magnetic pumping is turned on.

Power coupling between the RF wave and the plasma has been successfully achieved. This has been observed by monitoring the discharge

DC power along with the RF power. The change in the DC power is observed by noting the decrease in the discharge current when the RF circuit is turned on. The change in the RF power is observed by noting the change of the power damped in resistor R. This is easily calculated from the voltage decrease across R. Fig IV.18.a and Fig IV.18.b show the current and the voltage across R waveforms when the plasma is off and when the plasma is on. Fig IV.18.c and Fig IV.18.d are 10 times magnification of the peak of the voltage across R. It shows that when the plasma is on a decrease of 10 volts occurs. Both power changes are found to be comparable in magnitude and are between 10 and 20 percent of their respective nominal values. They also show the same functional dependence on the operating parameters, such as the RF driving frequency and the plasma density. Fig IV.19 shows the plot of the changes in the RF power and the DC power versus the operating frequency. This is an important result, since it shows that the power absorbed by the plasma depends linearly on the driving RF frequency. The theoretical analysis predicts that the energy increase rate for first order heating depends linearly on the RF frequency. So an increase in the RF driving frequency has a two-fold effect: An increase in power absorption and an increase in the energy increase rate. Fig IV.20 and Fig IV.21 support this observation. They show that an increase of the electron kinetic temperature occurs and is linearly proportional to the amount of absorbed RF power and consequently to the RF driving frequency. The increase in the electron kinetic temperature is, however, 2 to 4 times larger than theoretically predicted. The analytical expression for the energy increase rate is given by Equation (II.103) as

$$\frac{dE}{dt} = \frac{\delta\omega}{3n} E_o$$

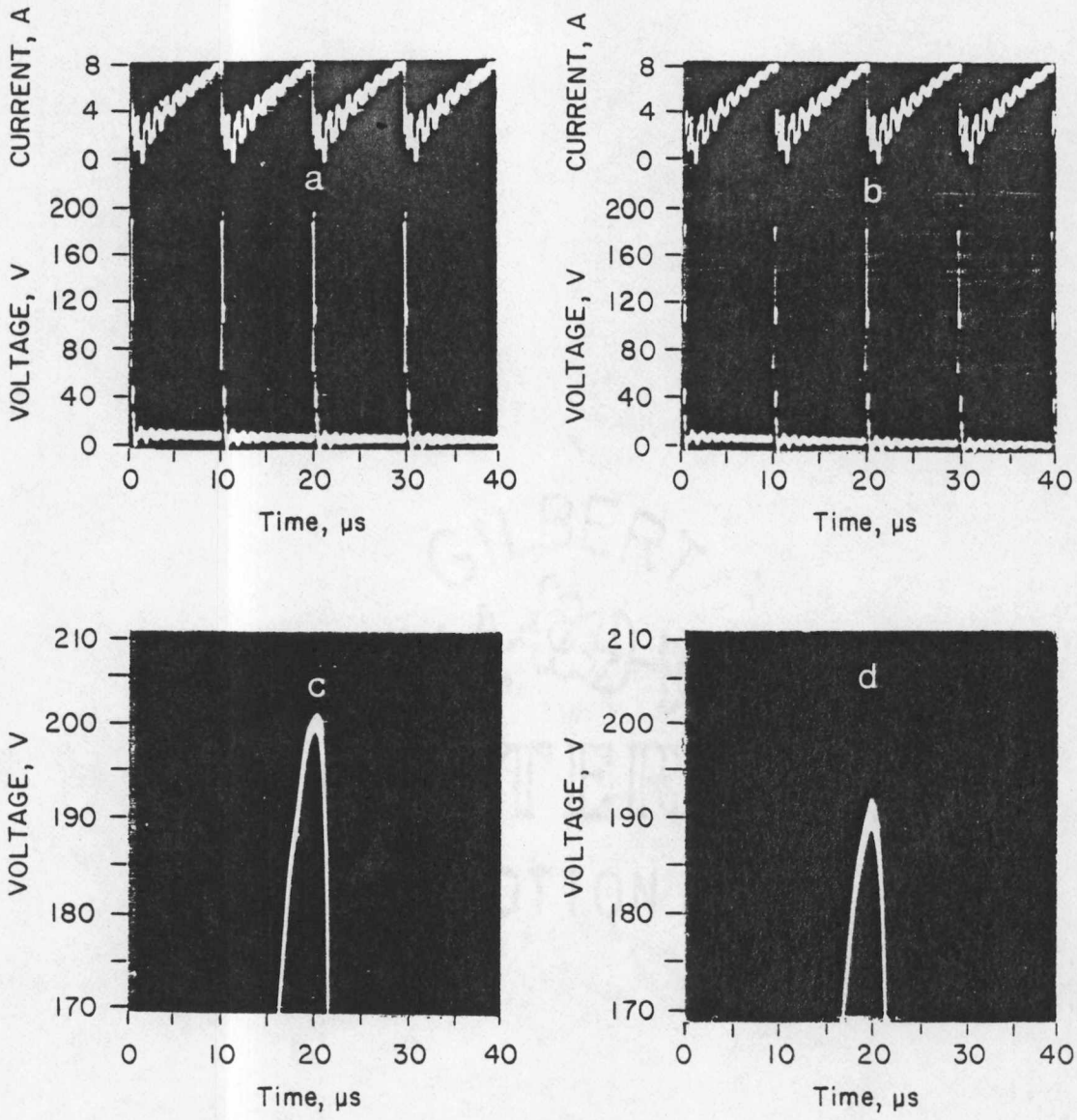

Fig IV.18. Scope trace of inductor current and resistor voltage (f = 100 kHz) when a) Plasma is off; b) Plasma is on; c) Peak of resistor voltage, with 5 μs/division horizontally and 5 volts/division vertically, when plasma is off; d) When plasma is on.

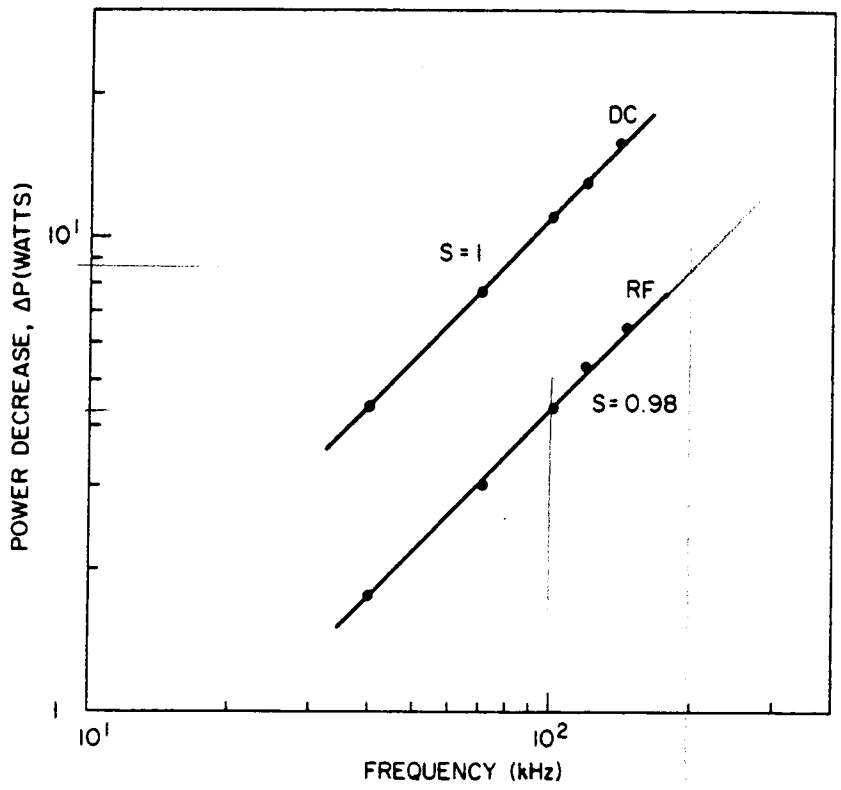

Fig IV.19. DC and RF power decrease versus driving frequency.

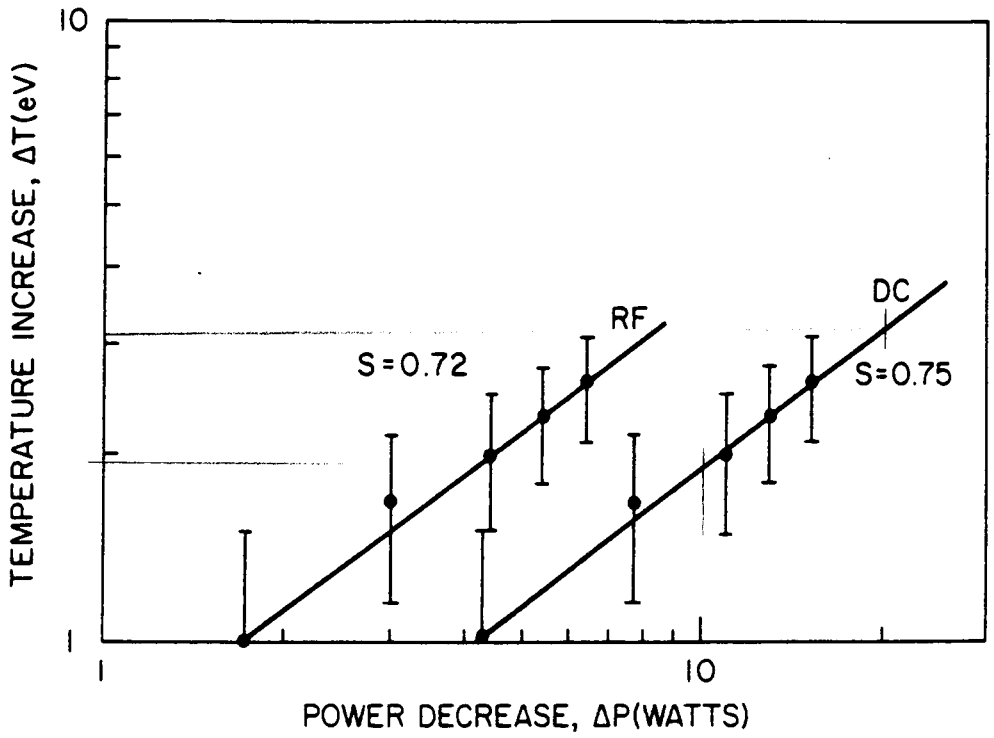

Fig IV.20. Electron kinetic temperature increase versus power decrease for a sawtooth perturbation.

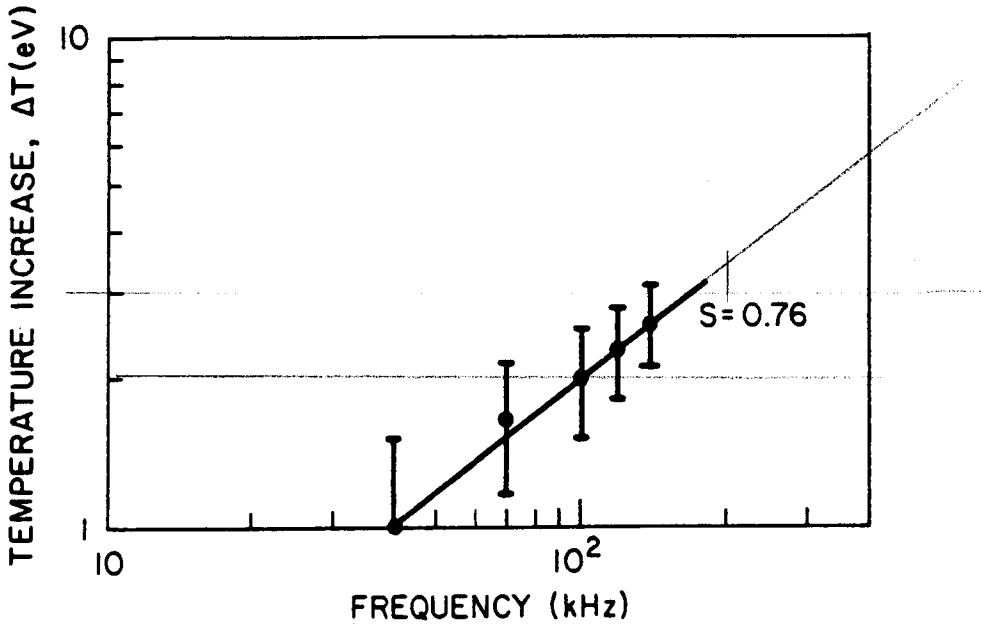

Fig IV.21. Electron kinetic temperature increase versus driving frequency for a sawtooth perturbation.

For a field modulation factor of $\delta = 0.005$, a driving RF frequency of 100 kHz, an electron with an initial energy of $E_o = 10$ eV, and a containment time of 100μs, the increase in energy is

$$\Delta E = 0.33 \text{ eV}$$

The measured value is 2 eV ± 0.5 eV.

Fig IV.21 establishes the fact that the increase in the electron kinetic temperature is proportional to the RF driving frequency. This is in agreement with the theoretical result of Equation (II.103).

The power generated by the RF circuit, as given by Equation (IV.19), is inversely proportional to the RF driving frequency

$$P = \frac{E^2}{2L}\frac{1}{f}. \tag{IV.26}$$

On the other hand, the amount of RF power absorbed by the plasma is linearly dependent on the RF driving frequency

$$P_{abs} = K_1 f, \tag{IV.27}$$

where K_1 is a constant whose value is calculated from Fig IV.19 and is equal to 4×10^{-5} watt-second. Taking the ratio of Equation (IV.27) to (IV.26) gives

$$\frac{P_{abs}}{P} = \frac{2LK_1}{E^2} f^2, \tag{IV.28}$$

or

$$P_{abs} = \frac{2LK_1}{E^2} f^2 P. \tag{IV.29}$$

As shown in Fig IV.20, the increase in electron kinetic temperature is linearly proportional to the RF absorbed energy, which gives the following relationship

$$\Delta T = K_2 P_{abs}, \tag{IV.30}$$

where K_2 is a constant whose value is calculated from Fig IV.20 to be 0.5 eV/watt. Substituting Equation (IV.29) into Equation (IV.30) gives

$$\Delta T = \frac{2LK_1K_2}{E^2} f^2 P. \qquad \text{(IV.31)}$$

The RF power, P, can be expressed as

$$P = \frac{EI_{Max}}{2}, \qquad \text{(IV.32)}$$

where I_{Max} is given by

$$I_{Max} = \frac{E}{L} t_o. \qquad \text{(IV.33)}$$

Substituting Equation (IV.32) into Equation (IV.31) gives

$$\Delta T = \frac{K_1K_2L}{E} f^2 I_{Max}. \qquad \text{(IV.34)}$$

The field modulation factor, δ, is given by

$$\delta = \frac{\Delta B}{B_o} = \frac{\mu_o N I_{Max}}{B_o}, \qquad \text{(IV.35)}$$

which yields the following relationship between δ and I_{Max}

$$I_{Max} = K_3 \delta, \qquad \text{(IV.36)}$$

where K_3 is given by

$$K_3 = \frac{B_o}{\mu_o N}.$$

Substituting Equation (IV.36) into Equation (IV.34) gives

$$\Delta T = \frac{K_1K_2K_3}{E} L f^2 \delta. \qquad \text{(IV.37)}$$

Equation (IV.37) establishes that the increase in the electron kinetic temperature is proportional to the first power of the field modulation factor. As an example, For an RF driving frequency of 100 kHz and a background magnetic field B_o = 450 gauss, the value of the field modulation factor is 0.004. Plugging these values along with the empirical values of constants K_1 and K_2 into Equation (IV.37) gives

$$\Delta T \sim 1.9 \text{ eV},$$

which is about equal to the actual measured value.

The ion energy distribution, on the other hand, does not undergo a significant change. This is due to the fact that the ion dwell time under the heating region is very short. Fig IV.22 shows that the energy distribution of the ions as monitored by a retarding potential energy analyser does not change substantially when magnetic pumping is turned on.

IV.6 Conclusion

Two experimental apparatus have been successfully designed, built, and operated to collect data for second and first order heating. Second order heating is achieved by adding a sinusoidal perturbation to the background magnetic field. The data collected in this case is not conclusive because of instrument limitations and the very low values (less than 1eV) of the energy increase to be expected. These limitations include the low RF power level available and the short containment times of the charged particles in the plasma.

First order heating is achieved by adding a sawtooth perturbation to the background magnetic field. For this, a state of the art switching circuit has been successfully designed and operated. The data collected shows qualitative agreement with the theoretical predictions. This suggests that first order heating can effectively be implemented experimentally, and if the RF power achievable is scaled up to relatively high values this heating method could be a competitive alternative.

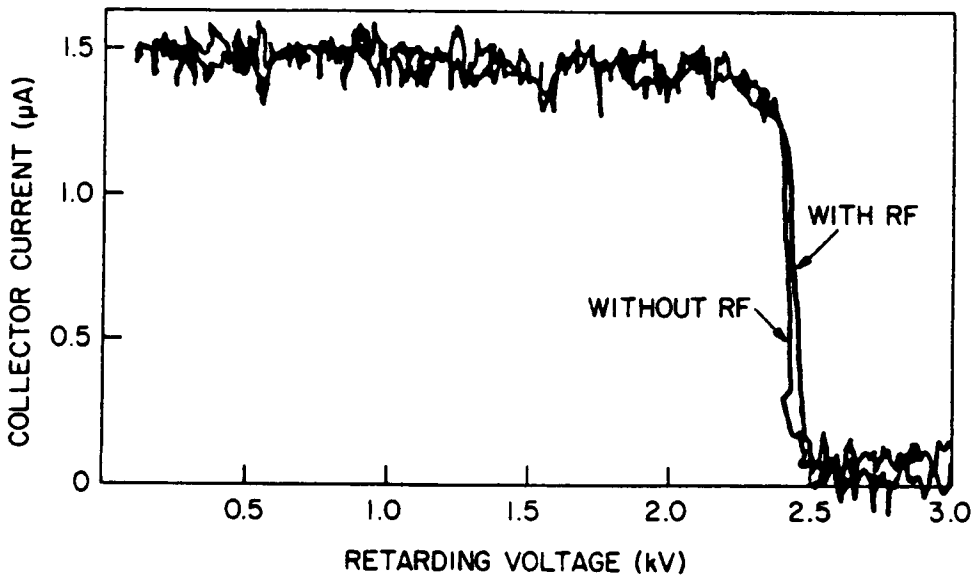

Fig IV.22. Ion energy distribution with and without magnetic pumping for V_A = 2.2 kV, I_A = 32 mA, P = 110 μ Torr, f = 100 kHz, and a sawtooth perturbation.

CHAPTER V

CONCLUSIONS

In this dissertation, collisional magnetic pumping as a plasma heating method has been studied theoretically, computationally and experimentally. In the theoretical part, the equations describing the change in the parallel, perpendicular, and total energy of the particles (ions or electrons) due to collisional magnetic pumping are presented, and a solution for the energy increase rate (or heating rate) is obtained. It has been found that if a sinusoidal perturbation is superimposed on the background magnetic field that confines the plasma, a heating rate proportional to the second power of the field modulation factor, δ, and strongly dependent on the plasma collisionality, is obtained. These two factors result in a small energy increase rate, which makes this approach to plasma heating inefficient. In the search for higher efficiency, a solution for the energy increase rate proportional to the first power of the field modulation factor, δ, is obtained. This solution is given for a general case, where the perturbation is any periodic function that satisfies a specific condition. This condition is given by Equation (II.38). A sawtooth function has been found to be a promising waveform for efficient plasma heating. The heating rate for this particular case is derived and compared to other heating rates. For a sawtooth perturbation, the energy increase rate is not only linearly dependent on the field modulation factor, but also independent of the plasma collisionality. This is especially advantageous for a fusion-grade plasma where the mean free path is longer than the plasma dimensions.

The computational treatment yields the parallel, perpendicular, and total energy versus time. It allows one to get a picture of the behavior of the different components of the energy as time progresses from the instant collisional magnetic pumping is turned on. Also, assuming a particular intial value of the energy, the energy increase rate is easily extracted from the energy-time plots, and compared with the theoretical results. Good agreement in both the sinusoidal and the sawtooth cases is obtained.

Two experimental apparatus have been fabricated to study heating when a sinusoidal or a sawtooth perturbation is applied. In the sinusoidal case, the heating data collected is not conclusive. The effects of collisional magnetic pumping in this case are too small to observe. This is mainly due to the characteristics and configuration of the plasma used and to the limited RF power available. In the case when a sawtooth perturbation is applied, enough RF power absorption occurs to allow conclusive measurements. The experimental results in this case show qualitative agreement with the theoretical predictions. They confirm that the energy increase rate is linearly dependent on the field modulation factor and on the RF driving frequency.

The results achieved in this work are a first step toward finding ways to improve this heating method. Experimentally, much more work can be done. First, the RF power available has to be scaled up to much higher levels. Second, a closed ended device, like a toroidal machine, would be a better candidate for the application of collisional magnetic pumping. Based on the preliminary results found in this work, more promising results are expected.

BIBLIOGRAPHY

BIBLIOGRAPHY

1. Alexeff, I., J. R. Roth, J. D. Birdwell, and R. Mallavarpu (1981), "Electromagnetic Emission and Anomalous Resistivity from Equal and Oppositely Directed Electron Beams", Phys. Fluids, Vol. 24, No. 7, pp. 1348-1350.

2. Baylor, L. R., J. R. Roth, P. Dehkordi, and M. Laroussi (1984), "Anomalous Drift Waves Detected with Microwave Scattering in an Electric Field Dominated Plasma", APS Bulletin, Vol. 29, No. 8, p. 1197.

3. Berger, J. M., W. A. Newcomb, J. M. Dawson, E. A. Friedman, R. M. Kulsrud, and A. Lenard (1958), "Heating of a Confined Plasma by Oscillating Electromagnetic Fields", Phys. Fluids, Vol. 1, No. 4, pp. 301-307.

4. Basu, A., A. S. Sharma, and A. C. Das (1985), "Spectrum of Turbulent Ion Acoustic Waves in a Magnetic Field", Plasma Phys. and Controll. Fusion, Vol. 27, No. 4, pp. 433-445.

5. Brenning, N. (1981), "Experiments on the Critical Ionization Velocity Interaction in Weak Magnetic Fields", Plasma Physics, Vol. 23, No. 10, pp. 967-977.

6. Baranga, A. B., G. Benford, D. Tzach, and K. Kato (1985), "Diagnosis of Strong Beam-Plasma Turbulence Conditions from Electromagnetic Emission", Phys. Rev. Lett., Vol. 54, No. 13, pp. 1377-1380.

7. Cap, F. F., Handbook on Plasma Instabilities, Academic Press, New York, 1976.

8. Chen, F. F. (1965), "Spectrum of Low-β Plasma Turbulence", Phys. Rev. Lett, Vol. 15, No. 9, pp. 381-383.

9. Chen, J. and T. C. Marshall (1985), "Current Drive in a High Beta Tokamak Using Magnetic Pumping", Plasma Phys. and Controll. Fusion, Vol. 27, No. 1, pp. 55-67.

10. Christophorou, L. G., Atomic and Molecular Radiation Physics, Wiley-Interscience, 1971.

11. Christophrou, L. G., Electron Molecule Interactions and Their Applications, Academic Press, new York, 1984.

12. Floquet, M. G. (1883), 'Sur les Equations Differentielles Lineaires", Annales E.N.S, T. 12, pp. 47-88.

13. Fyfe, D. and D. Montgomery (1979), "Possible Inverse Cascade Behavior for Drift-Wave Turbulence", Phys. Fluids, Vol. 22, No. 2, pp. 246-248.

14. Ghayspoor, R., Univ. Tenn, M. S. Thesis, 1986.

15. Gottlieb, M. B. (1963), "Magnetic Pumping for the Model C Stellarator", Tech. Memo. No. 173, Princeton Plasma Physics Laboratory.

16. Hasegawa, A. and K. Mima (1977), "Stationary Spectrum of Strong Turbulence in Magnetized Non-Uniform Plasma", Phys. Rev. Lett, Vol. 39, No. 4, pp. 205-208.

17. Hasegawa, A. and K. Mima (1977), "Pseudo-Three Dimensional Turbulence in Magnetized Non-Uniform Plasma", Phys. Rev. Lett, Vol. 21, No. 1, pp. 87-92.

18. Heald, M. A. and C. B. Wharton, Plasma Diagnostic with Microwaves, Krieger Publ, New York, 1978.

19. Hong, J., E. J. Powers, C. M. Singh, and J. R. Roth (1976), "Fluctuation Spectra in the NASA Lewis Bumpy Torus", APS Bulletin, Vol. 21, p. 1069.

20. Horton, W. (1985), "Onset of Stochasticity and the Diffusion Approximation in Drift Waves", Plasma Phys. and Controll. Fusion, Vol. 27, No. 9, pp. 937-956.

21. Huussen, F., S. Ikezwawa, and H. Dekluiver (1985), "Experimental Observation of Low-Frequency Spectra in the Turbulently-Heated TORTUR Tokamak Plasma", Plasma Phys. and Controll. Fusion, Vol. 27, No. 4, pp. 447-456.

22. Ince, E. L., Ordinary Differential Equations, Dover Pub., New York, 1956.

23. Ishihara, O. and A. Hirose (1985), "Wave-Particle Resonance Broadening in a Langmuir Turbulence", Phys. Fluids, Vol. 28, No. 7, pp. 2159-2161.

24. Jackson, J. D., Classical Electrodynamics, 2d ed., Wiley, 1975.

25. Kammash, T., Fusion Reactor Physics, Ann Arbor Science Pub., Ann Arbor, MI, 1975.

26. Kim, Y. C. and E. J. Powers (1977), "Effects of Frequency Averaging on Estimates of Plasma Wave Coherence Spectra", IEEE Trans. on Plasma Sci., PS-2, pp. 31-.

27. Kim, Y. C., J. M. Beall, and E. J. Powers (1980), "Bispectrum and Nonlinear Wave Coupling", Phys. Fluids, Vol. 23, No. 2, pp. 258-263.

28. Krawczonek, W. M., J. R. Roth, C. E. Boyd, J. Y. Hong, and E. J. Powers (1977), "A Data Acquisition and Handling System for the Measurement of Radial Plasma Transport Rates", Proc. of the Seventh Symp. on Engineering Problems of Fusion Research, Vol. 1, p. 392.

29. Krawczonek, W. M. and J. R. Roth (1970), "Paired Comparison Tests of the Relative Signal Detected by Capacitive and Floating Langmuir Probes in Turbulent Plasma from 0.2 to 10 MHz", APS Bulletin, Vol. 15, p. 1413.

30. Larraza, A., S. Putterman, and P. H. Roberts (1985), A Universal 1/f Power Spectrum as the Accumulation Point of Wave Turbulence", Phys. Rev. Lett., Vol. 55, No. 9, pp. 897-900.

31. Laroussi, M. P. D. Spence, D. Rosenberg, R. Ghayspoor, and J. R. Roth (1985), "RF Emission Power Measurement and Anomalous Drift Wave Study in a Classical Penning Discharge", APS Bulletin, Vol. 30, No. 9, p. 1397.

32. Laroussi, M. (1986), "Plasma Heating by Collisional Magnetic Pumping", Proc. of Southeastern Symp. on System Theory, ISSN 0094-2898, pp. 475-479.

33. Laroussi, M. and J. R. Roth (1987), "Collisional Magnetic Pumping as an Efficient Way to Heat a Plasma", AIP Conf. Proc., No. 159, pp. 438-441.

34. Magnus, W. and S. Winkler, Hill's Equation, Dover Pub., New York, 1979.

35. Miyamoto, K., Plasma Physics for Nuclear Fusion, MIT Press, Cambridge, MA, 1980.

36. Morse, P. M. and H. Feshbach, Methods of Theoretical Physics, Vol. I, McGraw-Hill, 1953.

37. McDaniel, E. W., Collision Phenomena in Ionized Gases, Wiley, 1964.

38. Mott, N. F. and H. S. W. Massey, The Theory of Atomic Collisions, 3d ed., Oxford, Clarendon Press, 1965.

39. Nayfeh, A. H., Introduction to Perturbation Techniques, Wiley, 1981.

40. Nicholson, D. R., Introduction to Plasma Physics, Wiley, 1983.

41. Pastel, R. L., J. R. Roth, and P. D. Spence (1982), "Parallel Electric Fields and Anomalous Resistivity in a Classical Penning Discharge", APS Bulletin, Vol. 27, No. 8, Pt. II, p. 1106.

42. Pastel, R. L. and J. R. Roth (1983), "Axial Electric Fields and Electron Number Density Profiles in a Classical Penning Discharge", APS Bulletin, Vol. 28, No. 8, pp. 1256-1257.

43. Pecseli, H. L., T. Mikkelsen, and S. E. Larsen (1983), "Drift Wave Turbulence in Low-β Plasmas", Plasma Phys., Vol. 25, No. 11, pp. 1173-1197.

44. Pecseli, H. L., J. J. Rasmussen, and K. Thomsen (1984), "Nonlinear Interaction of Convective Cells in Plasmas", Phys. Rev. Lett., Vol. 52, No. 24, pp. 2148-2151.

45. Penning, F. M. and K. Nienhuis (1949), "Construction and Application of a New Design of the Philips Vacuum Gauge", Philips Tech. Rev., Vol. 11, No. 116, pp. 116-122.

46. Powers, E. J., J. Y. Hong, Y. C. Kim, J. R. Roth, and W. M. Krawczonek (1978), "An FFT Fluctuation-Induced Plasma-Transport Diagnostic", APS Bulletin, Vol. 23, p. 905.

47. Ritz, Ch.P., R. D. Bengtson, S. J. Levinson, and E. J. Powers (1984), "Turbulent Structure in the Edge Plasma of the TEXT Tokamak", Phys. Fluids, Vol. 27, No. 12, pp. 2956-2959.

48. Rosenbluth, M. N. and R. Z. Sagadeev, General Editors, Basic Plasma Physics II, North Holland Pub., 1984.

49. Rose, D. J. and M. Clark, Jr., Plasmas and Controlled Fusion, MIT Press and Wiley, New York, 1961.

50. Roth, J. R., Introduction to Fusion Energy, InPrint Pub., Charlottesville, VA, 1986.

51. Roth, J. R. (1970), "Spectral Index and Sense of Energy Cascading in Turbulent, Hot-Ion Plasma", APS Bulletin, Vol. 15, p. 1427.

52. Roth, J. R., W. M. Krowczonek, E. J. Powers, Y. C. Kim, and J. Y. Hong (1981a), "Fluctuation and Turbulence in an Electric Field Bumpy Torus Plasma", J. Appl. Phys., Vol. 52, No. 4, pp. 2705-2713.

53. Roth, J. R., W. M. Krowczonek, E. J. Powers, J. Y. Hong, and Y. C. Kim (1981b), "The Role of Fluctuation-Induced Transport in a Toroidal Plasma with Strong Radial Electric Fields", Plasma Physics, Vol. 23, No. 65, pp. 509-514.

54. Roth, J. R. (1971), "Experimental Study of Spectral Index, Mode Coupling, and Energy Cascading in a Turbulent, Hot-Ion Plasma", Phys. Fluids, Vol. 14, No. 10, pp. 2193-2202.

55. Roth, J. R. (1966), "Modification of Penning Discharge Useful in Plasma Physics Experiments", Rev. Sci. Inst., Vol. 37, No. 8, pp. 1100-1101.

56. Roth, J. R. (1969), "Experimental Observation of Contunity Equation Oscillations in Slightly Ionized Deuterium, Neon, and Helium Gas", Plasma Phys., Vol. 11, pp. 763-777.

57. Roth, J. R. and P. D. Spence (1987), Measurement of the Effective Momentum Collision Frequency in a Turbulent, Weakly Ionized Plasma", The 18th Int. Conf. on Phenomena in Ionized Gases, Vol. 4, pp. 614-615.

58. Roth, J. R. and M. Laroussi (1987), "Plasma Heating by Collisional Magnetic Pumping for Possible Low Pressure Industrial Application", The 8th International Symposium on Plasma Chemistry, Vol. 4, pp. 2405-2410.

59. Schmidt, G., Physics of High Temperature Plasma, 2d ed., Academic Press, 1979.

60. Sardei, F. and H. K. Wimmel (1981), "Imporved Formulas for Trapped-Ion Anomalous Transport in Tokamak Without and With Shear", Plasma Physics, Vol. 23, No. 9, pp. 793-811.

61. Salz, F., R. G. Meyerand, Jr., E. C. Lary, and A. P. Walch (1961), "Electrostatic Potential Gradient in a Penning Discharge", Phys. Rev. Lett., Vol. 6, No. 10, pp. 523-525.

62. Smith, D. E. and E. J. Powers (1973), "Experimental Determination of the Spectral Index of a Turbulent Plasma from Digitally Computed Power Spectra", Phys. Fluids, Vol. 16, No. 8, pp. 1373-1374.

63. Smith, D. E., E. J. Powers, and G. S. Caldwell (1974), "Fast-Fourier-Transform Spectral-Analysis Techniques as a Plasma Fluctuation Diagnostic Tool", IEEE Trans. on Plasma Sci., PS-2, p. 263.

64. Spitzer Jr., L., and L. Witten (1953), "On the Ionization and Heating of a Plasma", AEC Research and Development Report, Princeton, NJ.

65. Spitzer Jr., L, Physics of Fully Ionized Gases, Interscience Pub., New York, 1956.

66. Tchen, C. M., H. L. Pecseli, and S. E. Larsen (1980), "Strong Turbulence in Low-β Plasmas", Plasma Physics, Vol. 22, pp. 817-829.

67. Tchen. C. M. (1976), "Repeated-Cascade Theory of Strong Turbulence in a Magnetized Plasma", Plasma Phsics, Vol. 18, pp. 609-626.

68. Terman, F. E., Radio Engineering, 3d ed., McGraw-Hill, 1947.

69. TFR Group, and A. Truc (1984), "Turbulent Spectrum Analysis in TFR Tokamak Plasma", Plasma Phys. and Controll. Fusion, Vol. 26, No. 9, pp. 1045-1062.

70. Welsby, V. G., The Theory and Design of Inductance Coils, 2d ed., New York, Wiley, 1960.

71. Whittaker, E. T. and G. N. Watson, A Course of Modern Analysis, 4th ed., Cambridge, 1958.

APPENDIXES

Appendix A

Magnetosonic Waves

Magnetosonic waves are low frequency electromagnetic modes which travel across the confining magnetic field (Nicholson, 1983). By low frequency we mean that the frequency of the wave, ω, is much smaller than the ion gyro-frequency,ω_{ci}.

To study these modes let's assume the following situation. As shown in Fig A.1 the background magnetic field B_0, and the magnetic field of the wave $\tilde{B}_1$ are in the z-direction, the electric field of the wave $\tilde{E}_1$ is in the x-direction, and the direction of propagation is along the y-axis. We also have the following conditons

$$k \cdot B_0 = 0,$$

$$k \cdot \tilde{E}_1 = 0,$$

and

$$\tilde{E}_1 \cdot B_0 = 0.$$

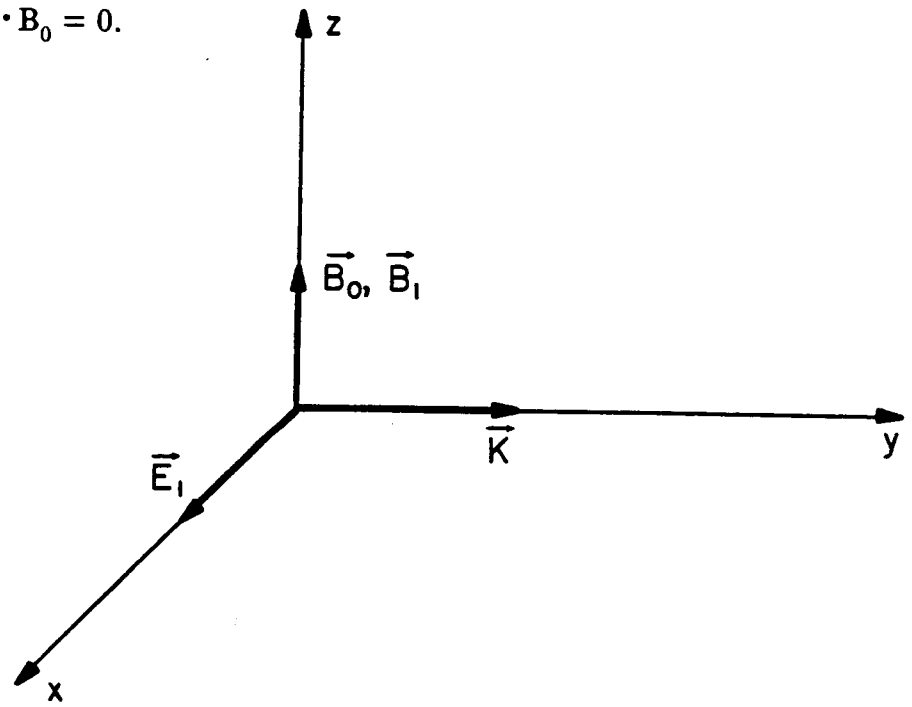

Fig A.1. Vector orientation for a magnetosonic wave.

The $\tilde{E}_1 \times B_0$ drift gives rise to electron and ion currents along the y-direction which cancel each other. If the electron mass is neglected compared to the ion mass, a polarization drift of ions along the x-axis gives rise to a polarization current in that direction. It is this current which generates the magnetic field of the wave $\tilde{B}_1$. Maxwell's equations and the momentum equation relevant to this case are

$$\nabla \times \tilde{E}_1 = - \frac{\partial \tilde{B}_1}{\partial t}, \tag{A.1}$$

$$\nabla \times \tilde{B}_1 = \mu_0 J + \mu_0 \varepsilon_0 \frac{\partial \tilde{E}_1}{\partial t}, \tag{A.2}$$

and

$$\frac{\partial v}{\partial t} = \frac{e}{m} (\tilde{E}_1 + v \times B). \tag{A.3}$$

Let

$$\tilde{E}_1 = E_1 e^{i(ky - \omega t)}, \tag{A.4}$$

$$B = B_0 + B_1 e^{i(ky - \omega t)}, \tag{A.5}$$

and

$$J = n_0 e (v_i - v_e), \tag{A.6}$$

where n_0 is the number density, v_i the ion drift velocity, and v_e the electron drift velocity. Substituting the above expressions into Equations (A.1), (A.2), and (A.3), and linearizing, the following set of equations is obtained

$$ik E_1 = - i\omega B_1, \tag{A.7}$$

$$ik B_1 = \mu_0 n_0 e v_{ix} - \mu_0 \varepsilon_0 i\omega E_1, \tag{A.8}$$

$$-i\omega m_i v_{ix} = e E_1 + e B_0 v_{iy}, \tag{A.9}$$

and

$$-i\omega m_i v_{iy} = -e v_{ix} B_0 , \tag{A.10}$$

where v_{ix} and v_{iy} are respectively the components of the ion velocity in the x-direction and the y-direction. The mass of the electron has been neglected in the above expressions.

From Equation (A.10) one gets

$$v_{iy} = -\frac{i\omega_{ci}}{\omega} v_{ix} , \tag{A.11}$$

where ω_{ci} is the ion cyclotron frequency.

Inserting (A.11) in (A.9) gives

$$v_{ix}\left(i\frac{\omega_{ci}}{\omega} e B_0 - i\omega m_i\right) = e E_1, \tag{A.12}$$

which yields

$$v_{ix} = \frac{e/m_i}{i\omega_{ci}^2/\omega - i\omega} E_1 . \tag{A.13}$$

Inserting Equation (A.13) into Equation (A.8) and using the fact that $B_1 = -k/\omega E_1$ gives

$$\frac{k^2}{\omega} = \mu_0 n_0 e \frac{(e/m_i)\omega}{\omega_{ci}^2 - \omega^2} + \mu_0 \varepsilon_0 \omega , \tag{A.14}$$

or

$$\frac{1}{\mu_0 \varepsilon_0} \frac{k^2}{\omega^2} - \frac{\omega_{pi}^2}{\omega_{ci}^2 - \omega^2} = 1 , \tag{A.15}$$

where ω_{pi} is the ion plasma frequency. Neglecting ω with respect to ω_{ci} gives

$$\omega^2 = \frac{1}{\mu_0 \varepsilon_0} \frac{k^2}{1 + \omega_{pi}^2/\omega_{ci}^2} . \qquad (A.16)$$

Knowing that

$$\omega_{pi}^2 = \frac{e^2 n_0}{m_i \varepsilon_0} ,$$

$$\omega_{ci}^2 = \frac{e^2 B_0^2}{m_i^2} ,$$

$$\frac{1}{\mu_0 \varepsilon_0} = c^2 ,$$

and letting

$$V_A = \frac{B_0}{(\mu_0 n_0 m_i)^{1/2}} , \qquad (A.17)$$

Equation (A.16) can be written as follows

$$\omega^2 = \frac{k^2 c^2}{1 + c^2/V_A^2} , \qquad (A.18)$$

or

$$\omega^2 = \frac{k^2 V_A^2}{1 + V_A^2/c^2} , \qquad (A.19)$$

where c is the speed of light. Equation (A.19) is the dispersion relation of magnetosonic waves traveling across the magnetic field with the velocity V_A given by Equation (A.17). V_A is the Alfven velocity. If the expression for the magnetic pressure given by

$$P_M = \frac{B_0^2}{2\mu_0}, \tag{A.20}$$

is inserted into Equation (A.17), V_A can be expressed as

$$V_A = \left(\frac{2P_M}{n_0 m_i}\right)^{1/2}. \tag{A.21}$$

Assuming that $V_A << c$, Equation (A.19) can be written as

$$\omega^2 = k^2 V_A^2. \tag{A.22}$$

This is an accoustic dispersion relation. Therefore, magnetosonic waves are similar to acoustic waves, but traveling against a magnetic pressure instead of a gas pressure.

Appendix B

Derivation of ℓ_1

The differential equation for the change in energy due to collisional magnetic pumping is

$$\frac{d^2E}{dt^2} - \left[\frac{d^2B}{dt^2}\left(\frac{dB}{dt}\right)^{-1} - \frac{3}{2}\nu_c\right]\frac{dE}{dt} - \frac{\nu_c}{B}\frac{dB}{dt}E = 0, \tag{B.1}$$

where E is the total energy, B is the magnetic field, and ν_c is the collision frequency. Let B assume the following form $B = B_0(1 + \delta f(t))$ where B_0 is the static magnetic field, δ is the field modulation, and f(t) a periodic function of period T. Substituting the above expression for B, Equation (B.1) becomes

$$\frac{d^2E}{dt^2} + \left(\frac{3}{2}\nu_c - \frac{f''(t)}{f'(t)}\right)\frac{dE}{dt} - \nu_c\frac{\delta f'(t)}{1 + \delta f(t)}E = 0. \tag{B.2}$$

Since $\delta << 1$ and a solution in the first order of δ is sought, the term $[1 + \delta f(t)]$ is approximated by 1. Let

$$A(t) = \frac{3}{2}\nu_c - \frac{f''(t)}{f'(t)},$$

and

$$g(t) = -\nu_c f'(t).$$

Equation (B.2) can be expressed as

$$\frac{dE^2}{dt^2} + A(t)\frac{dE}{dt} + \delta g(t)E = 0, \tag{B.3}$$

where A(t) and g(t) are periodic functions of period T. For a small field modulation factor δ the energy E(t) can be expanded as follows,

$$E(t) = E_0(t) + \delta E_1(t) + \delta^2 E_2(t) + \ldots \tag{B.4}$$

The solution of Equation (B.3) according to Floquet's theory is

$$E(t) = a_1 e^{\lambda_1 t} P_1(t) + a_2 e^{\lambda_2 t} P_2(t)\,, \tag{B.5}$$

where λ_1 and λ_2 can be expressed as

$$\lambda_1 = -\frac{3}{2} v_c + \delta \ell_1 + \delta^2 \ell_2 + \ldots.,$$

and

$$\lambda_2 = \delta \ell_1 + \delta^2 \ell_2 + \ldots$$

Since heating means an increase in time of the average energy, the first term of Equation (B.5) will not be considered further in the following development. Only the part of the solution associated with λ_2 can represent heating. Thus the solution of interest is

$$E(t) = e^{\lambda_2 t} P_2(t)\,, \tag{B.6}$$

where $P_2(t)$ is a periodic function of period T. The function $P_2(t)$ can be expanded as follows

$$P_2(t) = P_{20} + \delta\, P_{21}(t) + \delta^2 P_{22}(t) + \ldots \tag{B.7}$$

Also $e^{\lambda 2t}$ takes the expression

$$e^{\lambda_2 t} = 1 + \ell_1 t\, \delta + \left(\frac{1}{2} \ell_1^2 t^2 + \ell_2 t\right)\delta^2 + \ldots \tag{B.8}$$

Substituting Equations (B.7) and (B.8) into Equation (B.6) and comparing with Equation (B.4), the following expressions are found

$$E_0 = P_{20},$$

$$E_1 = \ell_1 t\, P_{20} + P_{21}(t),$$

$$E_2 = P_{20}\left(\frac{1}{2}\ell_1^2 t^2 + \ell_2 t\right) + \ell_1 t\, P_{21}(t) + P_{22}(t),$$

.

.

.

.

.

Equation (B.3) can now be decomposed into many sub-equations for different powers of δ. For the zero order of δ, Equation (B.3) becomes

$$\frac{d^2E_0}{dt^2} + A(t)\frac{dE_0}{dt} = 0. \tag{B.9}$$

For the sake of simplicity let $E_0 = P_{20} = 1$.

The equation associated with the first order of δ is

$$\frac{d^2E_1}{dt} + A(t)\frac{dE_1}{dt} = -g(t), \tag{B.10}$$

substituting $E_1 = \ell_1 t\, P_{20} + P_{21}$, Equation (B.10) becomes

$$\frac{d^2P_{21}}{dt^2} + A(t)\frac{dP_{21}}{dt} = -g(t) - \ell_1 A(t). \tag{B.11}$$

Let

$$K(t) = -g(t) - \ell_1 A(t). \tag{B.12}$$

The homogeneous equation associated with Equation (B.11) is

$$\frac{d^2P_{21}}{dt^2} + A(t)\frac{dP_{21}}{dt} = 0 \ . \qquad \text{(B.13)}$$

Multiplying by the integrating factor

$$\exp\left(\int_0^t A(u)du\right),$$

Equation (B.13) becomes

$$\frac{d}{dt}\left[\exp\left(\int_0^t A(u)du\right)\frac{dP_{21}}{dt}\right] = 0 \ ,$$

which leads to the solution

$$P_{21}(t) = C_1 + C_2\int_0^t e^{-a(s)}ds, \qquad \text{(B.14)}$$

where

$$a(t) = \int_0^t A(u)du \ . \qquad \text{(B.15)}$$

The general solution of Equation (B.11) is calculated as follows. Multiplying Equation (B.11) by the integrating factor $e^{a(t)}$ and integrating once, the following expresion is found

$$P_{21}'(t) = C_2 e^{-a(t)} + e^{-a(t)}\int_0^t K(s)\,e^{-a(s)}ds \ . \qquad \text{(B.16)}$$

Integrating (B.16) gives

$$P_{21}(t) = C_1 + C_2\int_0^t e^{-a(s)}\,ds + \int_0^t e^{-a(s)}\left(\int_0^s K(u)e^{a(u)}\right)ds. \qquad \text{(B.17)}$$

The second integral in Equation (B.17) is integrated by parts and is

$$\left(\int_0^t e^{-a(u)}du\right)\left(\int_0^t K(u)e^{a(u)}du\right)-\int_0^t\left(\int_0^s e^{-a(u)}du\right)K(s)e^{a(s)}ds.$$

Equation (17) becomes

$$P_{21}(t) = C_1 + C_2\int_0^t e^{-a(s)}ds + \left(\int_0^t e^{-a(u)}du\right)\left(\int_0^t e^{a(u)}K(u)du\right)$$

$$-\int_0^t e^{a(s)}\left(\int_0^s e^{-a(u)}du\right)K(s)ds. \qquad \text{(B.18)}$$

The fact that $P_{21}(t)$ is a periodic function gives the following conditions

$$P_{21}(T) - P_{21}(0) = 0,$$

and (B.19)

$$P'_{21}(T) - P'_{21}(0) = 0.$$

Substituting (B.18) in conditions (B.19) leads to

$$C_2\int_0^T e^{-a(u)}du + \left(\int_0^T e^{-a(u)}du\right)\left(\int_0^T K(u)e^{a(u)}du\right)$$

$$-\int_0^T\left(e^{a(s)}\int_0^s e^{-a(u)}du\right)K(s)ds = 0, \qquad \text{(B.20)}$$

and

$$C_2\left(e^{-a(T)} - e^{-a(o)}\right) + e^{-a(T)}\int_0^T K(s)\,e^{a(s)}ds = 0. \qquad \text{(B.21)}$$

Note that $e^{-a(o)} = 1$. Equation (B.21) gives

$$C_2 = \frac{e^{-a(T)}}{1 - e^{-a(T)}}\int_0^T K(s)\,e^{a(s)}ds. \qquad \text{(B.22)}$$

Substituting (B.22) into (B.20) and letting

$$Q(s) = e^{a(s)} \left[\frac{1}{1 - e^{-a(T)}} \int_0^T e^{-a(u)} du - \int_0^s e^{-a(u)} du \right], \qquad \text{(B.23)}$$

leads to the condition

$$\int_0^T K(s)\, Q(s)\, ds = 0 . \qquad \text{(B.24)}$$

Substituting $K(t) = - g(t) - \ell_1 A(t)$ into Equation (B.24) gives

$$\ell_1 = - \frac{\int_o^T g(s)Q(s)ds}{\int_o^T A(s)Q(s)ds} . \qquad \text{(B.25)}$$

Substituting A(t) and Q(t) by their expressions into the denominator and integrating by parts gives

$$\int_o^T A(s)Q(s)ds = T,$$

so

$$\ell_1 = - \frac{1}{T} \int_o^T g(s)\, Q(s) ds . \qquad \text{(B.26)}$$

Knowing that

$$g(t) = - v_c f'(t),$$

$$A(t) = \frac{3}{2} v_c - \frac{f''(t)}{f'(t)},$$

and

$$a(t) = \frac{3}{2} v_c t - \ell n \left(\frac{f'(t)}{f'(o)} \right),$$

the final expression for ℓ_1 is

$$\ell_1 = \frac{v_c}{T}\int_0^T \exp\left(\frac{3}{2}v_c s\right)\left\{\frac{1}{1-\exp\left(-\frac{3}{2}v_c T\right)}\int_0^T \exp\left(-\frac{3}{2}v_c u\right)f'(u)du\right.$$

$$\left. - \int_0^s \exp\left(-\frac{3}{2}v_c u\right)f'(u)du\right\}ds. \qquad \text{(B.27)}$$

The part representing heating in Floquet's solution is

$$E(t) = e^{\lambda_2 t}\, P_2(t), \qquad \text{(B.6)}$$

where

$$\lambda_2 = \delta\,\ell_1 + \delta^2\ell_2 + \ldots,$$

and

$$P_2(t) = P_{2_0}(t) + \delta\, P_{21}(t) + \delta^2 P_{22}(t) + \ldots$$

After expanding $e^{\lambda 2t}$, Equation (B.6) takes the following form

$$E(t) = E_o + \delta(\ell_1\, t\, E_o + P_{21}(t)) + \text{higher order terms.} \qquad \text{(B.28)}$$

The energy increase in a period $T = 2\pi/\omega$ is

$$\Delta E = \delta\,\ell_1 \frac{2\pi}{\omega} E_o. \qquad \text{(B.29)}$$

Appendix C

Programs Used for the Numerical Computations

Triangular perturbation

```
      COMMON I,L,SIGMA,T
      REAL*4 L
      OPEN(10,FILE='X.DAT',TYPE='NEW')
      OPEN(11,FILE='Y.DAT',TYPE='NEW')
      OPEN (12,FILE='Z.DAT',TYPE='NEW')
      WRITE(5,10)
10    FORMAT(2X,'ENTER E=, E+, E, SIGMA, NC, T, L, DELTA')
      READ(5,*)X,Y,Z,SIGMA,FREQ,I,L,DELTA
      TIME=0
      WRITE(10,*)TIME,X,Y,Z
      WRITE(11,*)TIME,Y
      WRITE(12,*)TIME,Z
      NUM=30*T/DELTA
      N=0
      DO 20 J=1,NUM
      I=TIME/T
      X=X-FREQ*X*DELTA+FREQ*.5*Y*DELTA
      Y=Y+FREQ*X*DELTA-FREQ*.5*Y*DELTA+FUNC(TIME)*Y*DELTA
      Z=X+Y
      TIME=TIME+DELTA
      N=N+1
      IF(N.EQ.300) THEN
      WRITE(10,*)TIME,X,Y,Z
      WRITE(11,*)TIME,Y
      WRITE(12,*)TIME,Z
      N=0
      ENDIF
20    CONTINUE
      END
      FUNCTION FUNC(TIME)
      COMMON I,L,SIGMA,T
      REAL*4 L
      IF(TIME.GE.I*T .AND. TIME.LE.L+I*T)THEN
      FUNC=SIGMA/(L+SIGMA*(TIME-I*T))
      ELSE
         FUNC=-SIGMA/((T-L)+SIGMA*(-(TIME-I*T)+T))
      ENDIF
      RETURN
      END
```

Triangular perturbation using Fourier series

```
      F(TIME)=SIN(6.28*TIME)+.33*SIN(18.8*TIME)+.2*SIN(31.4*TIME)
      G(TIME)=COS(6.28*TIME)+.11*COS(18.8*TIME)+(0.04*CCS(31.4*TIME))
      FUNC(TIME)=SIGMA*2.54*F(TIME)/(1+SIGMA*(.5-.4*G(TIME)))
      OPEN(10,FILE='X.DAT',TYPE='NEW')
      OPEN(11,FILE='Y.DAT',TYPE='NEW')
      OPEN(12,FILE='Z.DAT',TYPE='NEW')
      WRITE(5,10)
10    FORMAT(2X,'ENTER E=, E+, E, SIGMA, NC, T, DELTA ')
      READ(5,*)X,Y,Z,SIGMA,FREQ,T,DELTA
      TIME=C
      WRITE(10,*)TIME,X,Y,Z
      WRITE(11,*)TIME,Y
      WRITE(12,*)TIME,Z
      NUM=T/DELTA
      DO 20 I=1,NUM
      X=X-FREQ*X*DELTA+FREQ*.5*Y*DELTA
      Y=Y+FREQ*X*DELTA-FREQ*.5*Y*DELTA+FUNC(TIME)*Y*DELTA
      Z=X+Y
      TIME=TIME+DELTA
20    WRITE(10,*)TIME,X,Y,Z
      WRITE(11,*)TIME,Y
      WRITE(12,*)TIME,Z
      END
```

Sawtooth perturbation

```
        FUNC(TIME,I)=SIGMA/((1+SIGMA*(TIME/T-I))*T)
      OPEN(10,FILE='X.DAT',TYPE='NEW')
      OPEN(11,FILE='Y.DAT',TYPE='NEW')
          OPEN (12,FILE='Z.DAT',TYPE='NEW')
      WRITE(5,10)
10    FORMAT(2X,'ENTER E=, E+, E, SIGMA, NC, T, DELTA ')
      READ(5,*)X,Y,Z,SIGMA,FREQ,T,DELTA
      TIME=0
      WRITE(10,*)TIME,X
      WRITE(11,*)TIME,Y
      WRITE(12,*)TIME,Z
        NUM=10*T/DELTA
        DO 20 J=1,NUM
        I=TIME/T
      X=X-FREQ*X*DELTA+FREQ*0.5*Y*DELTA
        Y=Y+FREQ*X*DELTA-FREQ*0.5*Y*DELTA+FUNC(TIME,I)*Y*
      Z=X+Y                                                    DELTA
      TIME=TIME+DELTA
      WRITE(10,*)TIME,X
      WRITE(11,*)TIME,Y
20    WRITE(12,*)TIME,Z
      END
```

Sinusoidal perturbation

```
      FUNC(TIME)=-SIGMA*6.28*SIN(6.28*TIME)/(1+SIGMA*COS(6.28*TIME))
      OPEN(10,FILE='X.DAT',TYPE='NEW')
      OPEN(11,FILE='Y.DAT',TYPE='NEW')
      OPEN(12,FILE='Z.DAT',TYPE='NEW')
      WRITE(5,10)
10    FORMAT(2X,'ENTER E=, E+, E, SIGMA, NC, T, DELTA ')
      READ(5,*)X,Y,Z,SIGMA,FREQ,T,DELTA
      TIME=0
      WRITE(10,*)TIME,X,Y,Z
      WRITE(11,*)TIME,Y
      WRITE(12,*)TIME,Z
      NUM=20*T/DELTA
      N=0
      DO 20 I=1,NUM
      X=X-FREQ*X*DELTA+FREQ*.5*Y*DELTA
      Y=Y+FREQ*X*DELTA-FREQ*.5*Y*DELTA+FUNC(TIME)*Y*DELTA
      Z=X+Y
      TIME=TIME+DELTA
      N=N+1
      IF(N.EQ.200) THEN
      WRITE(10,*)TIME,X,Y,Z
      WRITE(11,*)TIME,Y
      WRITE(12,*)TIME,Z
      N=0
      ENDIF
20    CONTINUE
      END
```

Plotting subroutine

```
      REAL*4 MAX,MIN
            CHARACTER*1 FIL(10)
           DIMENSION TIME(1000),FUNC(1000)
           WRITE(5,10)
10         FORMAT(2X,'INPUT FILE NAME')
               READ(5,5)FIL
5              FORMAT(10A1)
           OPEN(10,FILE=FIL,TYPE='OLD')
             WRITE(5,31)
31           FORMAT(2X,'INPUT MAXIMUM VALUE')
             READ(5,*)MAX
          WRITE(5,32)
32        FORMAT(2X,'INPUT MINIMUM VALUE')
          READ(5,*)MIN
          WRITE(5,30)
30           FORMAT(2X,'INPUT NUMBER OF POINTS')
           READ(5,*)N
           DO 40 I=1,N
40         READ(10,*)TIME(I),FUNC(I)
           WRITE(5,50)
50         FORMAT(2X,'INPUT TERMINAL TYPE')
           READ(5,*)IMODEL,ICPS
           CALL TEKALL(IMODEL,ICPS,0,0,0)
         CALL PAGE(8.5,11.0)
         CALL HEIGHT(.25)
         CALL AREA2D(7.,8.)
         CALL XNAME('TIME',4)
       CALL YNAME('ENERGY',6)
           CALL GRAF(0,3,30,MIN,(MAX-MIN)/5,MAX)
           CALL CURVE(TIME,FUNC,N,0)
           CALL ENDPL(0)
           END
```

Appendix D

Description of the Classical Penning Discharge

The conventional or classical Penning discharge was first designed and used by F. M. Penning (Penning et al., 1949) as a low pressure vacuum gauge. It has since been scaled up in size and used in its conventional or modified configurations (as a magnetic bottle or a minimum B field geometry) by Roth et. al (Roth, 1966) and others. It produces a large volume, steady state plasma suitable for plasma physics and controlled nuclear fusion research. Fig D.1 is a schematic of the classical Penning discharge used in this research.

The vacuum vessel of the classical Penning discharge used in this research is made of a straight cylindrical section of pyrex glass either 15 cm or 10 cm in diameter. The uniform steady state axial magnetic field is generated by a set of 8 Magnion coils energized by a power supply able to provide up to 1000 Amperes at a voltage of 25V. The power in each coil can reach up to 3kW. For this reason the coils are water cooled. The magnetic field generated by these coils is adjustable and can reach up to approximately 0.44 Tesla. The axial profile of the magnetic field is shown in Fig D.2.

The gas to be ionized is introduced in the vacuum vessel through a leak valve situated at one end of the vessel. The gas is constantly pumped out by a combination of a mechanical pump and a turbomolecular pump mounted in series at the other end of the experimental volume. When no gas is introduced in the system, the base pressure is about 6 μ Torr. The pressure is read by two ion-gauges situated at each end of the apparatus. Also, the composition of the gas inside the vessel is monitored by a mass sepectrometer.

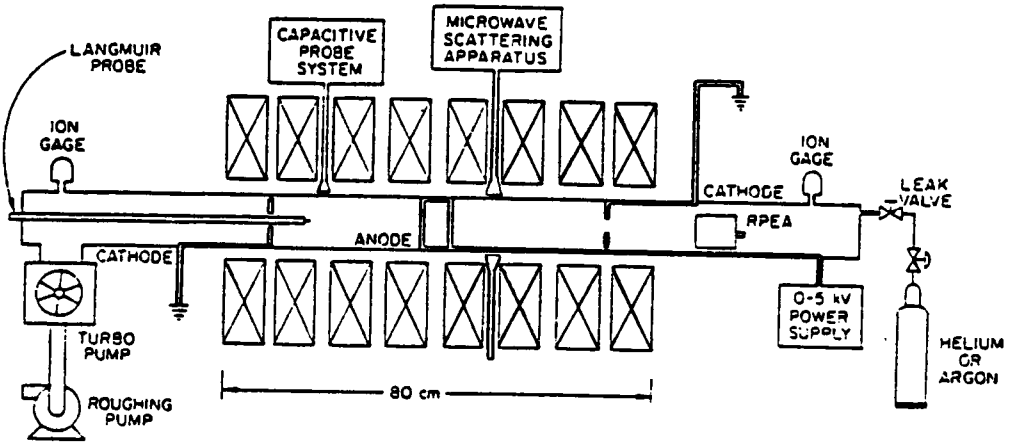

Fig D.1. Schematic of the classical Penning discharge with uniform axial magnetic field in the plasma volume.

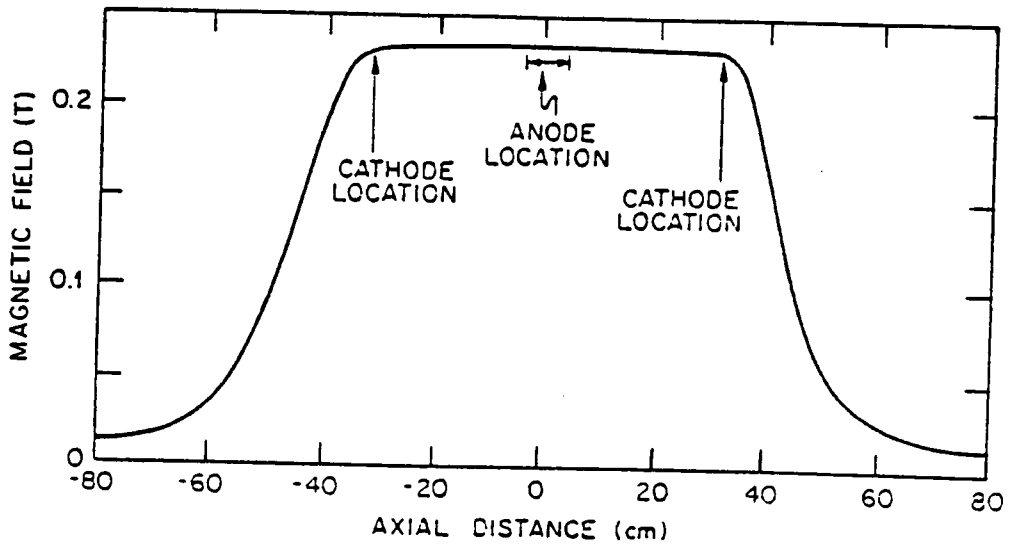

Fig D.2. Axial profile of the background magnetic field.

The ionization of the gas is achieved by applying a DC voltage to an anode ring situated in the middle of the straight section of the vaccum vessel. Two cold cathodes are placed symmetrically at each end of the chamber. These cathodes are two circular discs made out of tungsten for low sputtering yield. Both the anode and the two cathodes are water-cooled. The two cathodes have a circular opening in the center to allow a Langmuir probe be inserted axially into the plasma, and to let some of the ions escape and reach a retarding potential analyzer for energy distribution analysis. The DC voltage applied to the anode is in the kilovolt range, and the typical range of current is several tens to several hundreds of milliamperes at a working pressure range of 50 to 400 μ torr. The anode is energized by a power supply which provides up to 40 kV and 1 Ampere. The distance from the anode to each cathode is 32 cm. The plasma produced is steady state, weakly ionized, and its volume for a 10 cm diameter tube is 5000 cm^3. The gas used is usually helium or argon. The charged particle number density is typically 2 10^9 cm^{-3} with an electron kinetic temperature between 2 and 10 eV, and an ion kinetic temperature one to two orders of magnitude larger. The ions are hotter than the electrons due to heating by an ExB drift that heats the heavier species. Both radial and axial electric fields are present in the plasma. The axial field can reach up to 100 V/cm. The radial electric field, as measured in turbulence studies, can be several hundreds of volts per cm. Fig D.3 through Fig D.7 show the axial profile of different plasma parameters, as measured by a Langmuir probe, for a typical experimental run. Fig D.8 through Fig D.10 show the dependence of the electron and ion kinetic temperatures and of the number density on the magnetic field strength.

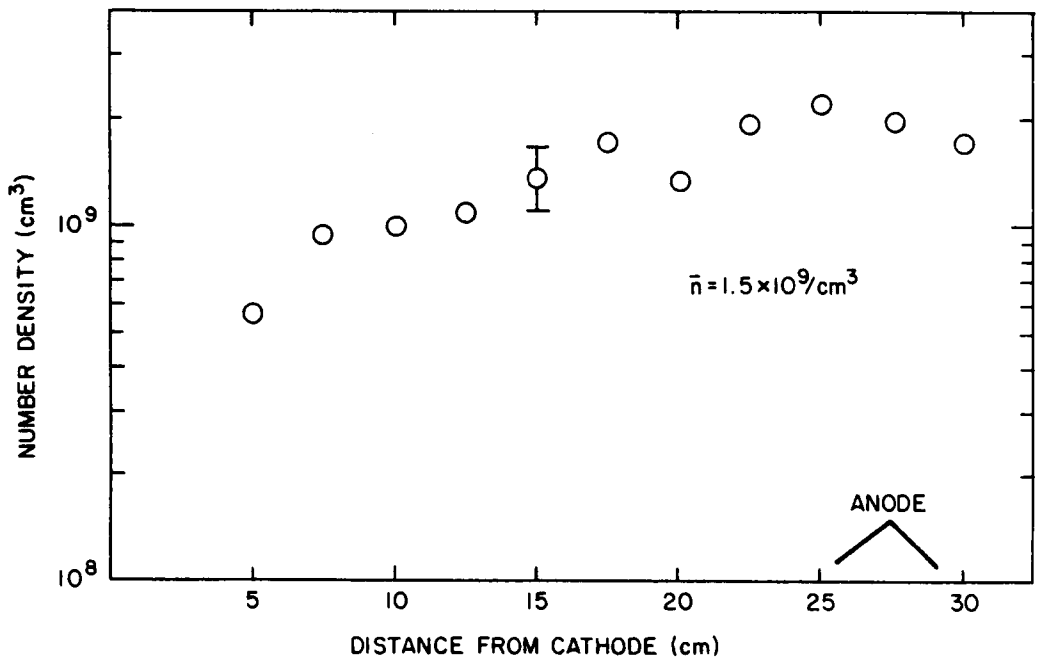

Fig D.3. Axial profile of the number density at $V_A = 1.5$ kV, $I_A = 40$ mA, P = 100 μ Torr, B = 0.255 T.

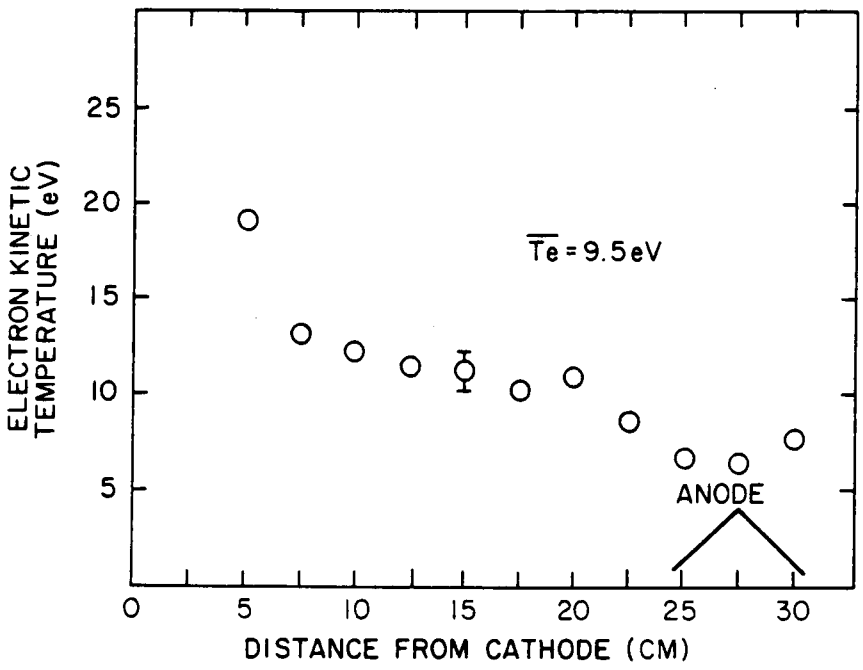

Fig D.4. Axial profile of the electron kinetic temperature at $V_A = 1.5$ kV, $I_A = 40$ mA, P = 100 μ Torr, B = 0.255 T.

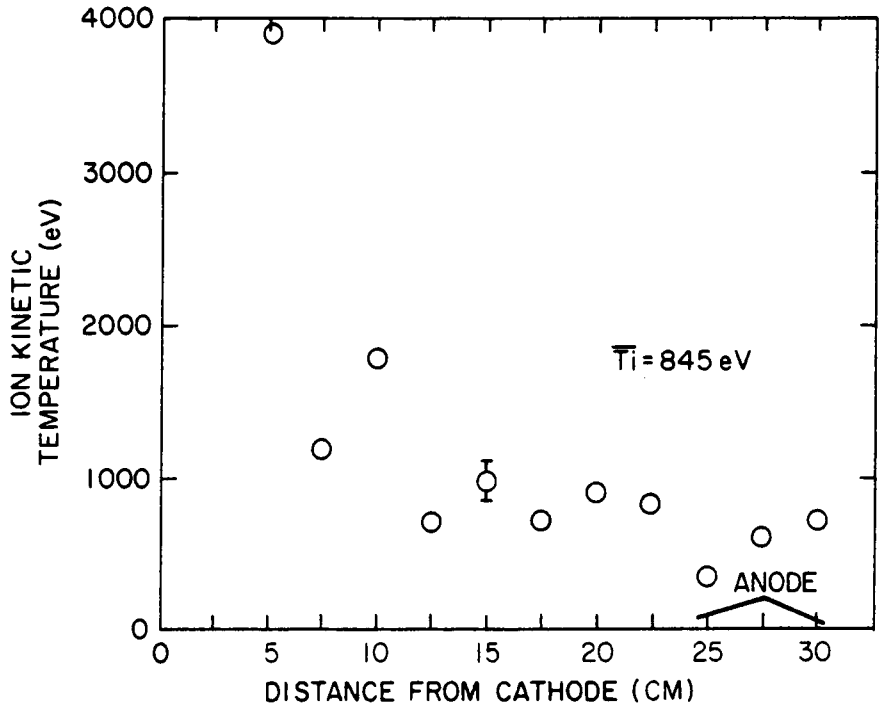

Fig D.5. Axial profile of the ion kinetic temperature at V_A = 1.5 kV, I_A = 40 mA, P = 100 μ Torr, B = 0.255 T.

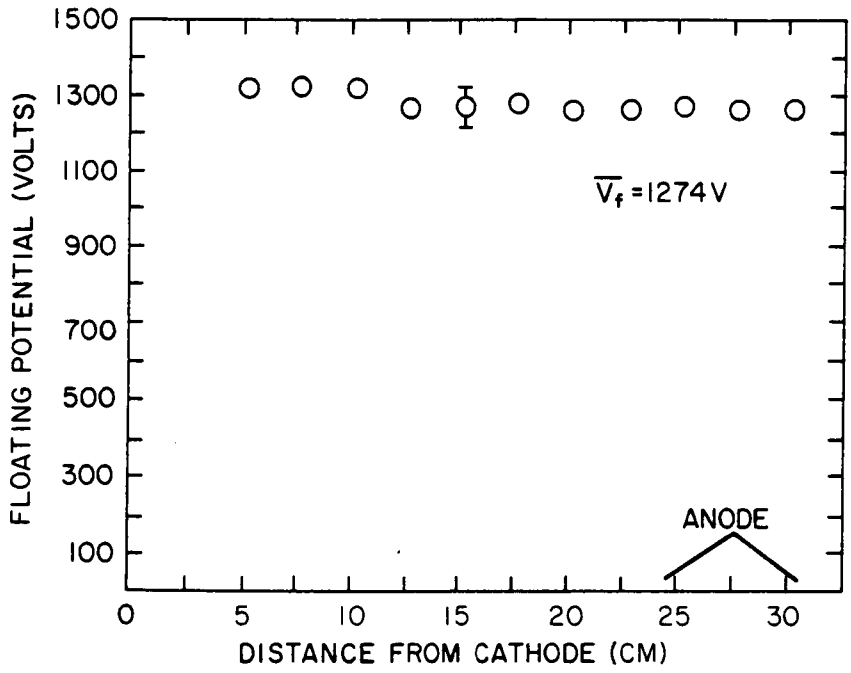

Fig D.6. Axial profile of the floating potential at V_A = 1.5 kV, I_A = 40 mA, P = 100 μ Torr, B = 0.255 T.

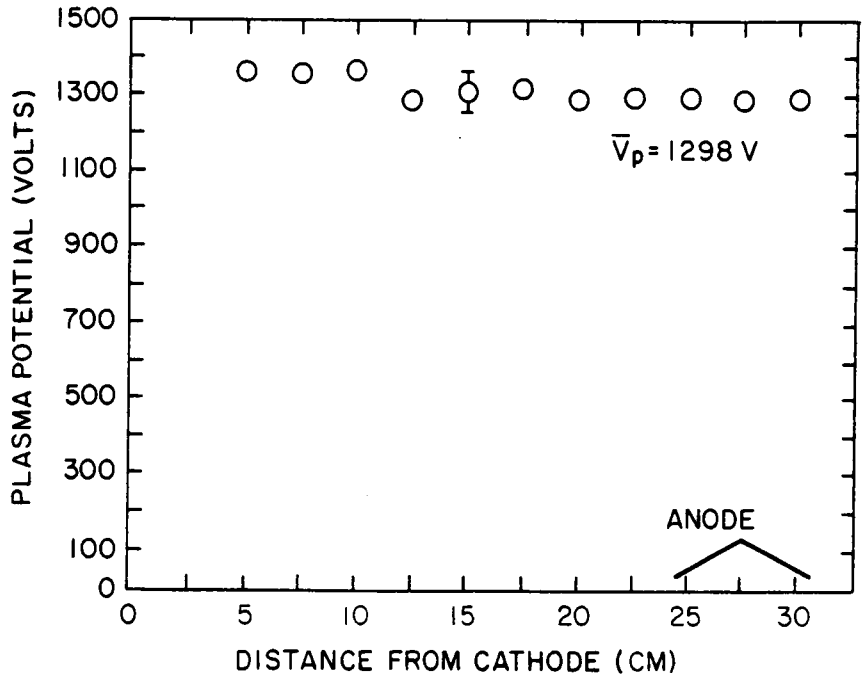

Fig D.7. Axial profile of the plasma potential at V_A = 1.5 kV, I_A = 40 mA, P = 100 μ Torr, B = 0.255 T.

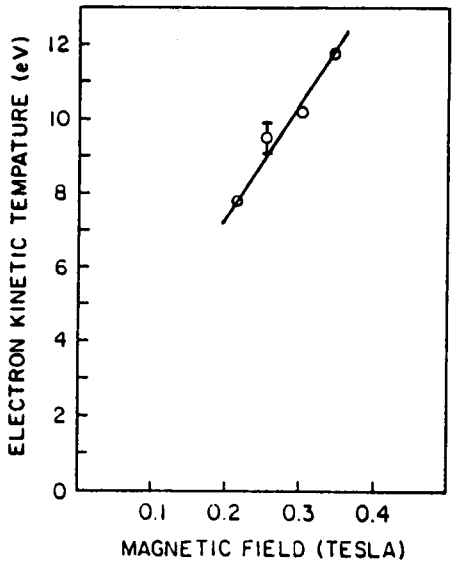

Fig D.8. Electron kinetic temperature versus magnetic field strength at $V_A = 1.5$ kV, $I_A = 40$ mA, P = 100 μ Torr.

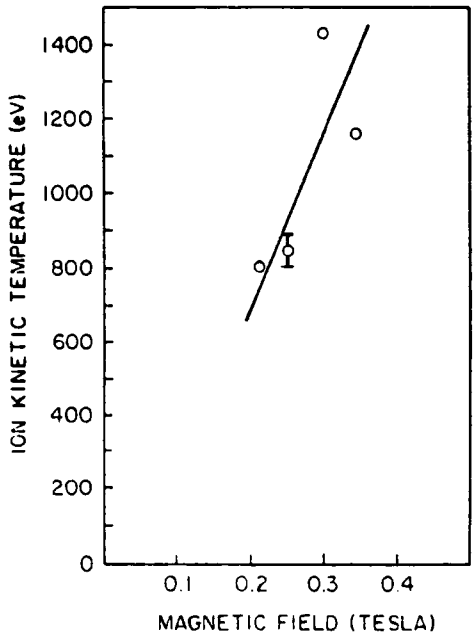

Fig D.9. Ion kinetic temperature versus magnetic field strength at $V_A = 1.5$ kV, $I_A = 40$ mA, P = 100 μ Torr.

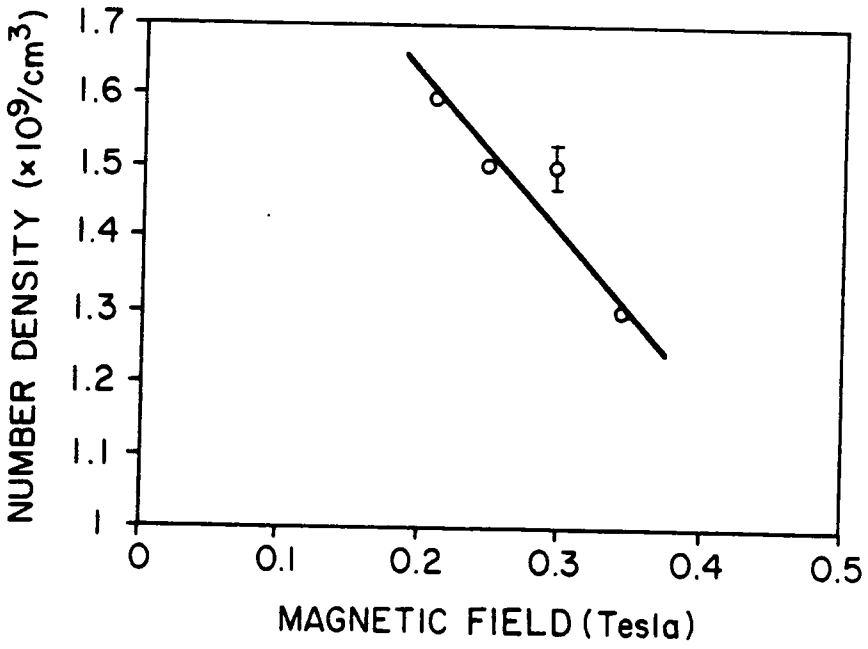

Fig D.10. Plasma number density versus magnetic field strength at $V_A = 1.5$ kV, $I_A = 40$ mA, P = 100 μ Torr.

The plasma produced by the classical Penning discharge has been found to exhibit a rich variety of physical processes. The understanding of the physics behind such processes can be very beneficial for the fields of plasma confinement and plasma heating. Our investigations showed that a wide range of instabilities are present in the plasma. These instabilities are mainly excited by drift waves generated in the presence of density and temperature gradients. Also, due to the existence of a strong radial electric field, rotating spokes gyrating in the azimuthal direction with an E_r/B_0 drift velocity have been observed (Baylor et al., 1984; Laroussi et al., 1985), where E_r is the radial electric field strength and B_0 is the background magnetic field. These spokes are known as E x B drift waves. They are the manifestation of an electrostatic instability known as the "dioctron instability" (Cap, 1976).

Radio frequency (RF) emission from the plasma has been observed (Laroussi et al., 1985). Fig D.11 shows a typical RF spectrum. The spectrum of emission extends from 0 to 1 GHz. Due to the turbulent state of the plasma, the emission observed has contributions from several different processes. One particularly interesting emitted frequency is the "Geometric Mean Plasma Frequency". This frequency was first observed by Roth and Alexeff (Alexeff et al., 1981). It is due to the presence of two interpenetrating beams of electrons interacting with a background of ions. The dispersion relation is

$$1 = \frac{\frac{1}{2}\omega_{pe}^2}{(\omega - k V_0)^2} + \frac{\frac{1}{2}\omega_{pe}^2}{(\omega + k V_0)^2} + \frac{\omega_{pi}^2}{\omega^2}, \qquad \text{(D.1)}$$

where ω_{pe} is the electron plasma frequency, ω_{pi} is the ion plasma frequency, k is the wave number, and $\pm V_0$ are the velocities of the electron beams. The frequency at which an instability growth exists is given by

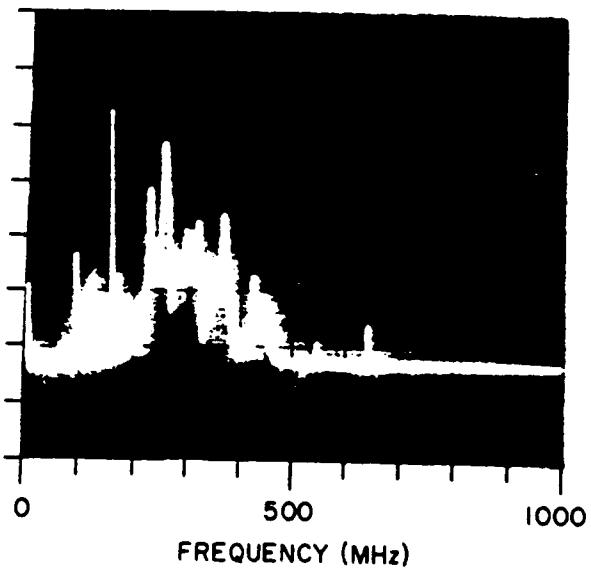

Fig D.11. RF emission spectrum with 100 MHz/division horizontal and 40 μV/division vertical.

$$\nu = 0.537\,(\omega_{pe}\,\omega_{pi})^{1/2}\,. \tag{D.2}$$

This is the geometric mean plasma frequency.

Appendix E

Characterization of the Plasma

This Appendix describes some of the physical processes occuring in the plasma on which collisional magnetic pumping is applied. This is important so that an understanding of the plasma behavior and its impact on the experiment is reached. The first section treats the collision phenomena and their influence on the plasma properties. The second section treats the dynamics of the plasma and its various instabilities along with the experimental methods used to study them.

E.1 Collision Phenomena

In this section we are going to study the collision phenomena occuring in a partially ionized gas. These collision events happen between charged particles or between charged particles and neutral atoms (or molecules).

The collisions between charged particles can be important because they affect directly plasma transport. This type of collision has been studied by Spitzer (Spitzer, 1956). Their cross-sections, based on multiple small angle collisions is given by

$$\sigma_m = \frac{Z_1^2 Z_2^2 e^4 \ell n \Lambda}{51.6 \sqrt{2}\, \varepsilon_0^2 (kT)^2}, \tag{E.1}$$

where Z_1 and Z_2 are the charge states of the incident and target particles. The temperature T is the kinetic temperature of the incident particle and $\ell n\ \Lambda$ is the Coulomb logarithm (a number between 7 and 20). The collision frequency is given by

$$\nu_c = n_1 \bar{v} \sigma_m , \tag{E.2}$$

where n_1 is the density of the target species, and $\bar{v}$ is the mean thermal velocity of the incident particle, assuming a Maxwellian velocity distribution, and is given by

$$\bar{v} = \left(\frac{8kT}{\pi m} \right)^{1/2} . \tag{E.3}$$

The parameters m and T are respectively the mass and the temperature of the incident particle. The values of the various collision frequencies for the plasma parameters relevant to the classical Penning discharge are computed and compared in Appendix F.

Since electrons have a much greater velocity than ions, collisions between electrons and neutrals dominate ion-neutral collisions. These collision processes and their results determine such plasma properties as its ionization state, its conductivity, its electric breakdown, etc. For this reason, we find it necessary to present a fairly detailed study of these processes.

Three types of collision can occur between an electron and a neutral atom or molecule: Elastic, inelastic, and superelastic collisions. In the case of an elastic collision the amount of energy lost is very small, and the internal state of the target remains unchanged. Using the principles of classical mechanics, the fraction of energy lost is (Christophorou, 1971, 1984)

$$\frac{\Delta E}{E} = \frac{2m M}{(m + M)^2} (1 - \cos\theta), \tag{E.4}$$

where θ is the scattering angle in the center of mass frame, m is the electron mass, and M is the target mass. For helium gas $\Delta E/E$ is about $5.5\ 10^{-4}$. When the collision is inelastic, the electron loses energy to the target, thus exciting or ionizing it. The amount of energy lost by the electron depends on the quantum states of the target. In the case of superelastic collisions, the internal energy of the target is imparted to the electron, thus increasing its

kinetic energy. The most important collisions of the three types listed above are elastic and inelastic. A discussion of these two types follows.

E.1.1 Elastic Collisions

The study of the scattering problem involves quantum theory for a complete understanding of the phenomena. Elastic scattering is usually studied using two methods: the method of partial waves, and the Born approximation. The former assumes that the incident particles are a plane DeBroglie wave of wavelength λ. For a wave propagating in the z-direction we have

$$\psi_{inc} = C e^{ikz} \quad . \tag{E.5}$$

The scattered wave presume the asymptotic form

$$\psi_{sc} = \frac{C}{r} f(\theta)\, e^{ikr} \quad , \tag{E.6}$$

where the scattered amplitude $f(\theta)$ is related to the differential elastic cross section per unit solid angle, $I_s(\theta)$ by

$$I_s(\theta) = \left| f(\theta) \right|^2 \quad . \tag{E.7}$$

The scattered amplitude is found by solving the equation

$$\nabla^2\psi + \frac{2M_r}{h^2}[E - V(r)]\psi = o \quad , \tag{E.8}$$

where $M_r = mM/m+M$, and $V(r)$ is the scattering potential. The solution of the above equation leads to an expression for the elastic scattering cross-section for the ℓ^{th} partial wave (Christophorou, 1984)

$$(\sigma_e)_\ell = \frac{4\pi}{k^2}(2\ell + 1)\sin^2\eta_\ell \quad , \tag{E.9}$$

where η_ℓ is the phase shift of the partial wave of ℓ due to the scattering process. The total elastic cross-section is then obtained by summing over the

partial waves

$$\sigma_e = \sum_{\ell=0}^{\infty} (\sigma_e)_\ell \,. \tag{E.10}$$

In the case of Born's approximation, which is good for fast particles, it is assumed that the scattering potential is small. The expression for the scattered amplitude is given by (Christophorou, 1984)

$$f(\theta) = -\frac{2M_r}{h^2} \int \frac{\sin kr}{kr} V(r) r^2 dr \,, \tag{E.11}$$

where k is the magnitude of the momentum transferred during the collision divided by h · the parameter V(r) is given by

$$V(r) = -\varepsilon^2 \int \left(\frac{z}{r} - \sum_{n=1}^{z} \frac{1}{|r - r_n|} \right) \left| \psi_0(r_1, \ldots) \right|^2 d\tau_1 \ldots d\tau_z \,. \tag{E.12}$$

For helium, the angular distribution and total cross section has been obtained using the wave function obtained by Hyllerass (Christophorou, 1984)

$$\psi_0 = \frac{Z^3}{(\pi a_0)^3} e^{-Z(r_1 + r_2)/a_0} \,, \tag{E.13}$$

where Z = 1.69. Fig E.1 shows the angular distribution of electrons scattered elastically by helium atoms. It shows that most of the electrons are scattered in the forward direction (Massey and Mott, 1965). Fig E.2 shows the momentum transfer cross-section for helium versus electron energy for low energy electrons (Christophorou, 1984).

E.1.2 Inelastic Scattering

The main inelastic processes of interest are electronic excitation of atoms and molecules, ionization by electron impact, and excitation of molecular rotation and vibration by electron impact.

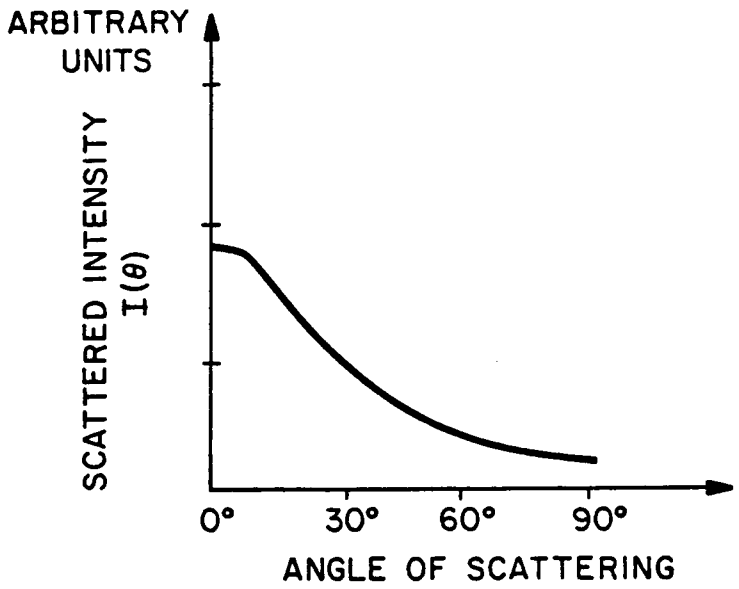

Fig E.1. Angular distribution of electrons elastically scattered by helium atoms.

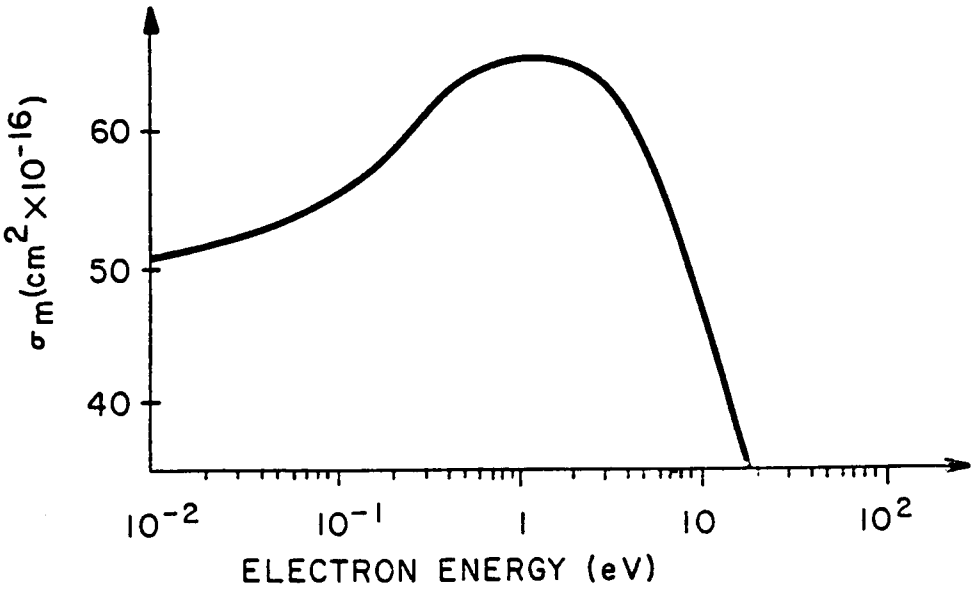

Fig E.2. Elastic scattering cross-section of slow electrons by helium atoms.

a. Electronic excitation by electron impact

When the energy of the electrons exceeds the lowest electronic excitation threshold of the target, the incident electron can loose energy to the target by exciting its electronic levels. The total cross-section for a target electronically excited from state o to state n is given by

$$\sigma_n = 2\pi \int_0^{\pi} I_n(\theta) \sin\theta \, d\theta \,, \tag{E.14}$$

where $I_n(\theta)$ is the differential excitation cross-section having the units cm^2 /atom (molecule) steradian. I_n is given by (Christophorou, 1984)

$$I_n = \frac{4\pi^2 m^2}{h^4} \frac{k_n}{k} \left| \int V_n(r') \exp[i(k n_o - k_n n) r'] d\tau' \right|^2 , \tag{E.15}$$

where $2\pi/k$ and $2\pi/k_n$ are the DeBroglie wave lengths of the impinging and scattered electrons, n_o and n are the unit vectors in the incident and scattered direction. V_n is given by (Christophorou, 1984)

$$V_n = e^2 \int \sum_1^N \frac{1}{r_{o,s}} \psi_o(r_1, r_2, \ldots, r_N) \psi_n^*(r_1, r_2, \ldots, r_N) d\tau_1 \ldots d\tau_n \,, \tag{E.16}$$

where $r_{o,s}$ is the distance between the incident electron and the S^{th} atomic electron, and ψ_o and ψ_n are respectively the wave function for the ground state and the n^{th} excited state. Table E.1 shows the differential cross-sections for excitation of various levels of helium (Massey and Mott, 1965). Table E.2 shows the total cross-section for excitation of various states of helium (Massey and Mott, 1965). As shown in Fig E.3, excitation functions for allowed transitions in atoms rise sharply from zero at the threshold to a maximum value at an electron energy above the threshold, then decreases with increasing incident electron energy (Christophorou, 1984). Fig E.4 shows that the angular distribution of the scattered electrons by helium atoms after exciting various levels is peaked in the forward direction (Massey and Mott,

EXCITED STATE	2^1S		2^1P		3^1P	
	ANGLE OF SCATTERING					
ELECTRON ENERGY (ev)	0°	30°	0°	30°	0°	30°
100	0.51	0.066	5.92	0.035	1.21	0.011
200	0.55	0.013	14.425	0.0034	2.99	0.0011

Table E.1. Differential cross-sections per unit solid angle in units of a^2_0 per steradian for various excited states of helium atoms and two scattering angles.

ELECTRON ENERGY (ev)	2^1S	2^1P	3^1P
100	0.023	0.155	0.0384
200	0.012	0.111	0.0275

Table E.2. Total cross-sections in units of πa^2_0 for various excited states of helium atoms.

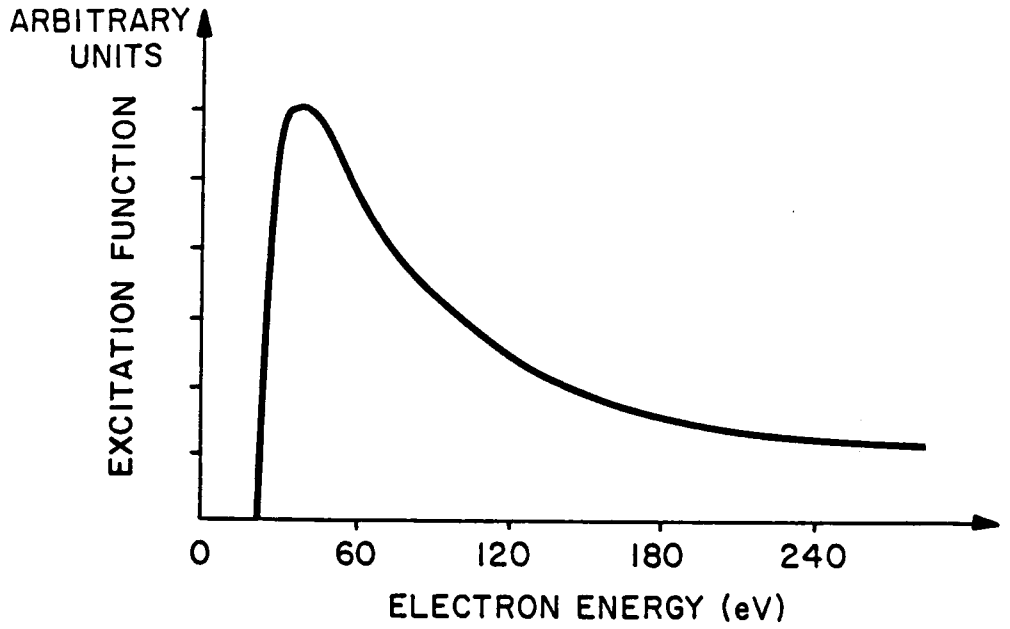

Fig E.3. Excitation function for a $5^1S \rightarrow 2^1P$ helium transition.

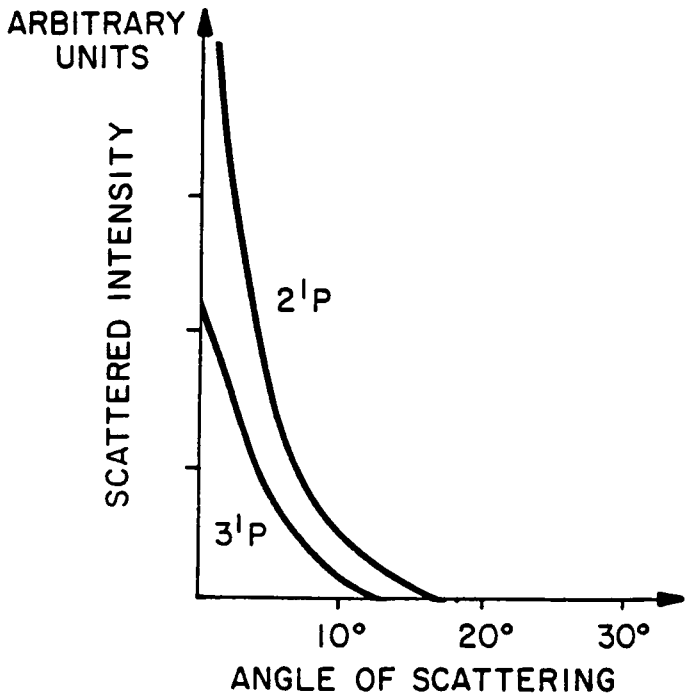

Fig E.4. Angular distribution of 200 eV incident electrons after exciting the 2^1P and 3^1P transitions in helium atoms.

1965). The scattered intensity falls off sharply and the number of scattered electrons at an angle larger than ten degrees is practically zero.

b. Ionization by electron impact

If the energy of the incident electron is higher than the ionization threshold of the target, impact ionization can occur. The ionization cross-section is given by

$$\sigma_i = \int_{\varepsilon} \int_{\Omega} I_{\varepsilon}(\theta) d\Omega \, d\varepsilon \,, \tag{E.17}$$

where $I_{\varepsilon}(\theta)d\varepsilon$ is the differential cross-section. For both atoms and molecules, the cross-section for single ionization is much larger than the one for multiple ionization. Using Born's approximation it has been shown that σ_i varies with the incident electron energy ε in the following manner (Christophorou, 1984)

$$\sigma_i \, \alpha \, \varepsilon^{-1} \ell n \, B\varepsilon, \tag{E.18}$$

where B^{-1} is a quantity of the order of the ionization potential. Fig E.5 shows the ionization cross-section for helium as function of the incident electron energy (Christophorou, 1984).

Ionization can occur in different ways

1. Ionization without dissociation

   $AB + e^- \rightarrow AB^+ + 2e^-$

2. Dissociative ionization

   $AB + e^- \rightarrow A + B^+ + 2e^-$

3. Ion pair formation

   $AB + e^- \rightarrow A^+ + B^- + e^-$

4. Dissociation with complete ionization

   $AB + e^- \rightarrow A^+ + B^+ + 3e^-$

Each of the above processes occur at a different threshold.

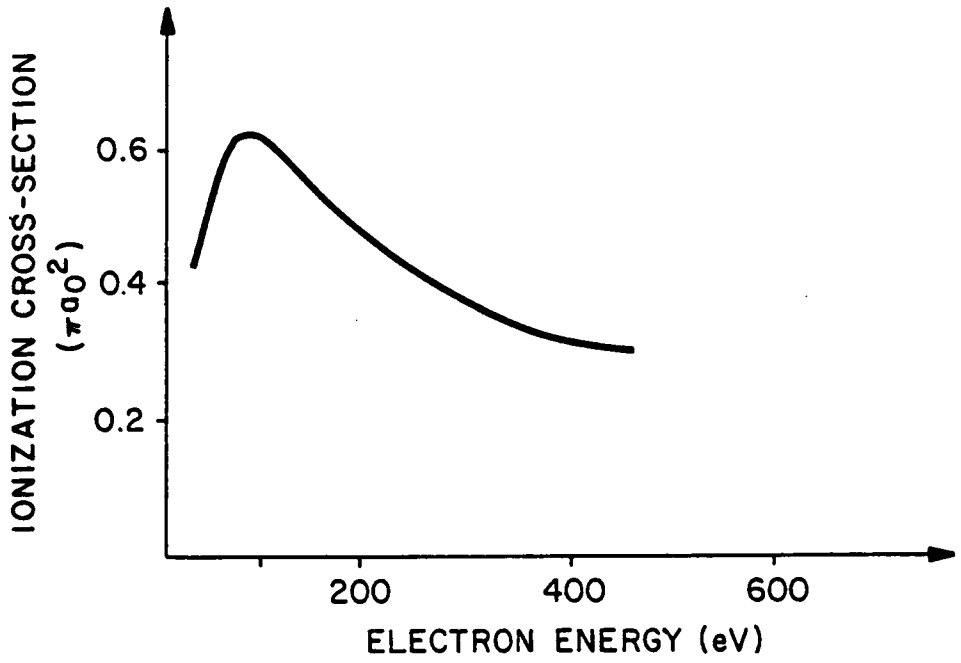

Fig E.5. Cross-section for ionization of helium atoms by electron impact based on Born's approximation, in units of πa^2_0, where a_0 is the Bohr radius, $a_0 = 0.529 \times 10^{-10}$ m.

c. Excitation of molecular rotation and vibration by electron impact

Low-energy electrons, like those present in our plasmas, are known to lose energy by exciting molecular rotational and vibrational levels. The energy lost by these electrons through this process is much greater than that lost due to elastic scattering. For maximum excitation, the collision time has to be in the order of the natural vibrational period of the molecule.

Electrons can also interact with atoms and molecules by resonant scattering. This happens when the energy of the incident electron is sufficient to excite the target to a state where the electron is temporarily captured. If the electron affinity is positive the resonant scattering can lead to a stable negative ion. If the electron affinity is negative the excited atom or molecule can revert back to a neutral in its ground state and a free electron. A process worth mentioning in this category of electron-molecule interaction is dissociative attachment. It can be represented by

$$e^- + AB \rightarrow A + B^- .$$

This process is often important in a weakly ionized plasma and affects strongly plasma properties such as the electrical conductivity and electrical breakdown strength.

E. 1.3 Penning ionization

This process is important for a gaseous discharge plasma like the one operated in the UTK plasma laboratory. This type of ionization involves an excited atom.

$$A^* + B \rightarrow A + B^+ + e^- .$$

For ionization to occur, the excited energy of atom A has to be larger than the ionization potential of atom B. Table E.3 shows cross-sections of the Penning process for different types of atoms (Rosenbluth et al., 1984).

ATOM B \ ATOM A	He (2^1S)	Ar (P)
H	22	——
He (2^3S)	110	——
Ar	5.5	——
H_2	2.4	0.3

Table E.3. Cross-sections in units of 10^{-16} cm^2 of the Penning process obtained experimentally for atoms of thermal energies.

In the case where atom A and B are helium atoms, the cross-section is 110 10^{-16} cm^2. Associative Penning ionization can also occur

$$A^* + B \rightarrow AB^+ + e^- .$$

In this case, the energy necessary for ionization comes from the energy of the excited atom added to the bond energy of the molecular ion AB^+.

E.1.4 Other processes

A number of other processes involving electrons and ions, electrons and excited ions, and ions and neutrals occur. The following is a list of these interactions for helium gas

$$e^- + H_e^+(1s) \rightarrow He^{2+} + 2e^- .$$

$$e^- + H_e^{2+} \rightarrow He^{+*}(n) + h\nu .$$

$$e^- + H_e^+(1s) \rightarrow He^{+*}(2s) + e^- .$$

$$e^- + H_e^+(1s) \rightarrow He^{+*}(2p) + e^- .$$

$$e^- + H_e^{+*}(2s) \rightarrow He^{+*}(n) + e^- \quad n = 3,4,5,\ldots .$$

$$e^- + H_e^{+*}(2p) \rightarrow He^{+*}(n) + e^- \quad n = 3,4,5,\ldots .$$

$$e^- + H_e^{+*}(n) \rightarrow He^{2+} + 2e^- \quad n \geq 2 .$$

$$H_e^+ + He \rightarrow He + He^+ .$$

$$H_e^+ + He \rightarrow 2He^+ + e^- .$$

$$H_e^{2+} + He \rightarrow He + H_e^{2+} .$$

$$H_e^{2+} + He \rightarrow H_e^{2+} + H_e^+ + e^- .$$

E.1.5 Discussion

Table E.4 shows the cross-sections of some of the important collision processes discussed in this chapter for electrons energy of 10eV and a helium gas (Christophorou, 1984), (Massey and Mott, 1965).

PROCESS	ELASTIC	EXCITATION BY ELECTRON IMPACT	PENNING IONIZATION	IONIZATION BY ELECTRON IMPACT	VIBRATIONAL EXCITATION
CROSS-SECTIONS IN cm^2	$4\ 10^{-16}$	10^{-18}	$1.1\ 10^{-14}$	$8\ 10^{-18}$	10^{-17}

Table E.4. Cross-sections of various collision processes for a helium gas and electron energy of 10 eV.

These values are relevant to the plasma used in the experimental part of this dissertation. It is clear that Penning ionization has the largest cross-section. A rank of these processes with respect to their likelihood of occurrence (which implies a large cross-section) is the following:

1. Penning ionization.
2. Elastic scattering.
3. Vibrational excitation.
4. Ionization by electron impact.
5. Excitation by electron impact.

The above rank helps give a quantitative idea about the main interaction processes occurring between the charged particles and the neutral atoms or molecules in a partially ionized gas. It is these processes that give the plasma its properties and define its physical state and degree of ionization.

E.2 Drift Waves and Plasma Turbulence

E.2.1 Drift waves

Drift waves are generated in a plasma when spatial inhomogenities are present. They are electrostatic modes with an electric field parallel to the direction of propagation (Schmidt, 1979). These modes propagate perpendicular to the density or the temperature gradient. The frequencies of these waves are typically lower than the ion gyro-frequency. To study these modes, kinetic theory or a fluid approach can be used. Drift waves are very important because they can directly affect plasma confinement. They can lead to growing instabilities and enhance particle transport across the confining magnetic field. There are a wide variety of drift waves. Of particular interest is the density gradient driven drift wave, due to its relevence to the plasma used in this work. To study this drift wave, the continuity equation and the momentum equation are used. These are

$$\frac{\partial n}{\partial t} + \nabla \cdot (nv) = 0, \qquad \text{(E.19)}$$

and

$$\frac{\partial v}{\partial t} + v \cdot \nabla v = - \frac{1}{nm} \nabla P + \frac{q}{m} E + \frac{q}{m} (v \times B). \qquad \text{(E.20)}$$

We assume that the background magnetic field is along the z-axis and the electric field of the wave in the y-z plane with its y-component much larger than the z-component. This situation is illustrated in Fig E.6. B_0 is the background static magnetic field.

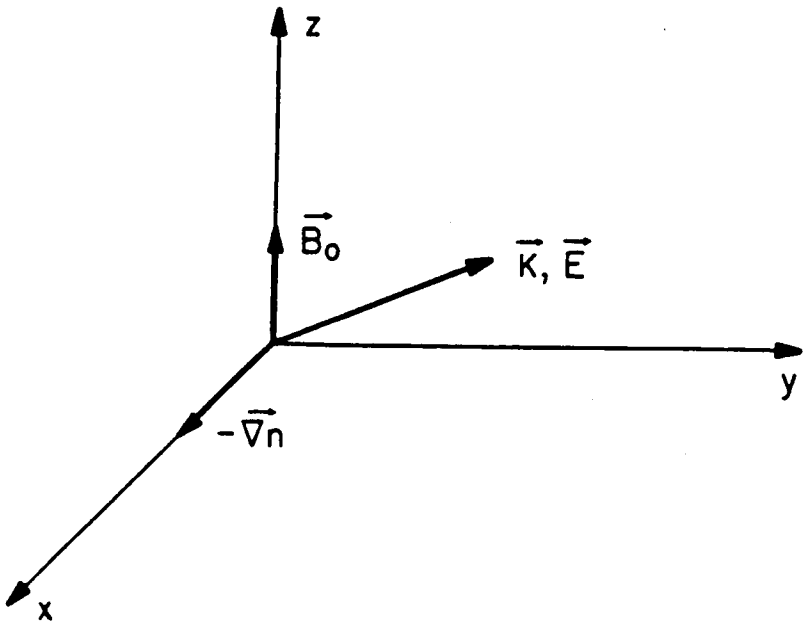

Fig E.6. Vector orientation for a density gradient generated drift wave.

The electric field satisfies the equation

$$E = - \nabla \phi . \qquad \text{(E.21)}$$

The vectors E and k are given by

$$k = k_y \vec{y} + k_z \vec{z}, \qquad \text{(E.22)}$$

and

$$E = E_y \vec{y} + E_z \vec{z}, \tag{E.23}$$

with

$$k_y >> k_z \text{ and } E_y >> E_z.$$

Assuming that the frequency of the wave is high enough that the ions remain unperturbed, the electrons undergo an E_y x B_z force. Consequently the electrons drift in the x-direction, causing a charge separation. A density gradient along the x-axis is then created. Let

$$n = n_o + \tilde{n}_1 , \tag{E.24}$$

$$v = v_o + \tilde{v}_1 , \tag{E.25}$$

and

$$\phi = \phi_o + \tilde{\phi}_1 , \tag{E.26}$$

where n_o, v_o, and ϕ_0 are respectively the initial values of the density, velocity and potential, and $\tilde{n}_1$, $\tilde{v}_1$, and $\tilde{\phi}_1$ are the perturbations. The linearized continuity equation is

$$\frac{\partial \tilde{n}_1}{\partial t} + \nabla \cdot (n_0 \tilde{v}_1) = 0 . \tag{E.27}$$

Assuming that

$$\tilde{n}_1 = n_1 \exp i(k_y y + k_z z - \omega t), \tag{E.28}$$

$$\tilde{v}_1 = v_1 \exp i(k_y y + k_z z - \omega t), \tag{E.29}$$

and

$$\tilde{\phi}_1 = \phi_1 \exp i(k_y y + k_z z - \omega t), \tag{E.30}$$

Equation (E.27) becomes

$$- i\omega n_1 + \frac{\partial}{\partial x} (n_0 v_{1x}) = 0 , \tag{E.31}$$

where $k_z v_{1z}$ and $k_y v_{1y}$ have been neglected due to the smallness of k_z and v_{1y}. Equation (E.31) can also be written as

$$- i\omega n_1 + \frac{\partial n_0}{\partial x} (v_{1x}) = 0 , \tag{E.32}$$

v_{1x} is the velocity due to the E x B drift. The electric field is given by

$$E = \begin{bmatrix} 0 \\ -k_y \phi_1 \exp i(k_y y + k_z z - \omega t) \\ -k_z \phi_1 \exp i(k_y y + k_z z - \omega t) \end{bmatrix} \tag{E.33}$$

Using Equation (E.33) and assuming that $B = B_0 \vec{z}$, the drift velocity v_{1x} is

$$v_{1x} = \frac{-k_y \phi_1}{B_0}. \tag{E.34}$$

Substituting Equation (E.34) into Equation (E.32) the density n_1 is

$$n_1 = \frac{i}{\omega} \frac{\partial n_0}{\partial x} \frac{k_y \phi_1}{B_0}. \tag{E.35}$$

The density perturbation n_1 can also be found from the momentum equation. This is easily done by taking the z-component of this equation. Linearizing and Fourier transforming gives

$$-i\omega m_e n_0 v_{1z} = -T_e i k_z n_1 + e n_0 k_z \phi_1, \tag{E.36}$$

where $\nabla P = T(\nabla n)$ has been used. If ω is small enough, as it is for an electrostatic wave, Equation (E.36) can be approximated by

$$0 = -T_e i k_z n_1 + e n_0 k_z \phi_1, \tag{E.37}$$

or

$$n_1 = -i \frac{e n_0 \phi_1}{T_e}. \tag{E.38}$$

Equating (E.35) and (E.38) we get

$$\omega = -\frac{T_e k_y}{e n_0 B_0} \frac{\partial n_0}{\partial x}, \tag{E.39}$$

or

$$\omega = k_y v_{De}, \tag{E.40}$$

where v_{De} is the electron diamagnetic drift velocity defined as

$$v_{De} = -\frac{T_e}{e n_0 B_0} \frac{\partial n_0}{\partial x}. \tag{E.41}$$

v_{De} can also be expressed as a function of the Debye length, the electron plasma frequency, and the electron gyrofrequency as

$$v_{De} = - \frac{\omega_{pe}^2 \lambda_D^2}{\Omega_e} \frac{d}{dx} \ell n\, n_0(x)\,, \tag{E.42}$$

where

$$\lambda_D = \left(\frac{T_e \varepsilon_0}{n_0 e^2} \right)^{1/2}, \tag{E.43}$$

$$\omega_{pe} = \left(\frac{n_0 e^2}{\varepsilon_0 m_e} \right)^{1/2}, \tag{E.44}$$

and

$$\Omega_e = \frac{e B_0}{m}. \tag{E.45}$$

Equation (E.40) is the dispersion relation of electrostatic drift waves.

E.2.2 Transition to Turbulence

a. Theoretical background

The drift wave instability is caused by density gradients, temperature gradients, or E x B drift. It affects the edge regions of all magnetically confined plasmas, and because of that it is called "The Universal Instability". A characteristic quantity of these drift waves is the electron diamagnetic drift velocity defined by

$$v_{De} = - \frac{\omega_{pe}^2 \lambda_D^2}{\Omega_e} \frac{d}{dx} \ell n\, N(x)\,, \tag{E.46}$$

where ω_{pe} is the electron plasma frequency, λ_D is the Debye length, Ω_e the electron gyro-frequency, and N(x) is the equilibrium density. When the flow of electrons along the magnetic field lines is slowed down by collisions, a resistive drift wave instability develops. Theoretical work has been done

concerning drift wave fluctuations that evolve into a strongly turbulent state. A plasma becomes turbulent when micro-instabilities grow and a nonlinear limit is reached in which plasma parameters such as electric field, electrostatic potential, number density, currents, and magnetic fields fluctuate in a random fashion. Chen showed that the spectrum of potential fluctuations can be determined (Chen, 1965). If the turbulence is locally homogeneous and isotropic, Tchen et al. showed that the wave number spectrum is divided in three ranges denoted "Production", "Coupling", and "Dissipation" (Tchen et al., 1980). Tchen et al. showed, by using dimensional arguments, that the power spectrum of the potential fluctuation follows a power law. In the production range it goes as k^{-3}, in the coupling range as k^{-5}, and in the dissipation range as $k^{-3/2}$. It has been found that energy cascades along the wave number spectrum until it is dissipated at large wave numbers, propagating in the plane perpendicular to the magnetic field B. Other theoretical attempts based on the general ion fluid equations have been done. Some of them disagree with Tchen's results but still showed a k^{-5} power law in the coupling range.

To check these theories experimentally, the determination of the relationship between the frequency of the wave and its wave number is of great importance. This is because it is more practical to measure power spectra as a function of frequency rather than as a function of wave number. Hence to relate the experimental results to the theoretical ones, a relationship between k and ω is to be assumed. The simplist one is the linear relationship $\omega = kv_0$, where v_0 is the convective velocity of the turbulence. This assumption is called Taylor's hypothesis or "The frozen turbulence approximation". It is applicable when the turbulence flows past the detecting

probe with high velocity. In practice it is found that in many cases the linear relationship between k and ω is violated and one measures power spectra with spectral indices different from the one predicted by theory (Roth, 1971; Roth et al., 1981).

b. Application to Experiment

To study a turbulent plasma experimentally, and compare it with theory, the turbulent power spectra have to be measured, and the different turbulence-related parameters extracted from it. For this purpose a digital spectral analyses technique which allows one to compute the spectral index and the relationship between k and ω was implemented (Smith et al., 1974; Krawczonek et al., 1977). The potential fluctuation ϕ and density fluctuation n are respectively monitored by capacitive and Langmuir probes. After conditioning and filtering, the signals proportional to ϕ and n are sampled by transient recorders, and sent to a general purpose computer for processing. A fast Fourier transform algorithm allows the computation of the Fourier transforms of the digitized signals. Then, the autopower, crosspower, phase, and coherency spectra are computed and plotted. Of particular interest is the phase spectrum which shows the phase shift each spectral component undergoes when traveling from a probe location to another. If we assume a wave $A\exp i(\omega t - kx)$, the phase is $\theta(\omega) = k(\omega)\Delta x$, where $k(\omega)$ is the wave number at the frequency ω and Δx is the distance between two probes. So in fact the phase spectrum gives the relationship between k and ω. This is important if any comparison between theory and experiment is to be done successfully. The spectra obtained by the digital spectral analyses are calculated on the basis of the following spectral densities.

1. Auto-power Spectral Density

The auto-power spectral density of a random process g(t) is defined by

$$S(f) = \lim_{T\to\infty} \frac{1}{T} E[|G(f)|^2], \tag{E.47}$$

where E represents an expected value, and G(f) is the Fourier transform of g(t). The auto-correlation function defined by

$$R(\tau) = E[g(t)g(t+\tau)] \ , \tag{E.48}$$

is the inverse Fourier transform of the auto-power spectral density and R(o) is the mean square value of the random process.

$$R(o) = E[g^2(t)] = \int_{-\infty}^{\infty} S(f)\, df. \tag{E.49}$$

To find the power contained in a random process, the integral of its auto-power spectral density over the whole range of frequency has to be calculated. In other words S(f) represents power per unit frequency.

2. Cross-power Spectral Density

Let g_1 (t) and g_2 (t) be two random processes and G_1 (f) and G_2 (f) their respective Fourier transforms. The cross-power spectral density is defined by

$$S_{12}(f) = \lim_{T\to\infty} \frac{1}{T} E[G_1(f)\, G_2^*(f)], \tag{E.50}$$

where the * denotes complex conjugates. Since S_{12} (f) is a complex quantity, it can be expressed as

$$S_{12}(f) = |S_{12}(f)| \exp(i\,\theta_{12}(f)), \tag{E.51}$$

or

$$S_{12}(f) = C_{12}(f) + i\,Q_{12}(f). \tag{E.52}$$

C_{12} (f) and Q_{12} (f) are respectively called co-spectral density and the quadrature spectral density. The cross-correlation function defined by

$$R_{12}(\tau) = E[g_1(t)\, g_2(t+\tau)], \tag{E.53}$$

is the inverse Fourier transform of S_{12} (f), and R_{12} (0) is given by

$$R_{12}(0) = \int_{-\infty}^{\infty} S_{12}(f)\,df. \tag{E.54}$$

Since $Q_{12}(-f) = -Q_{12}(f)$ and $C_{12}(-f) = C_{12}(f)$, $R_{12}(0)$ can be expressed as

$$R_{12}(0) = E[g_1(t)\,g_2(t+\tau)] = 2\int_0^{\infty} C_{12}(f)df. \tag{E.55}$$

3. Coherence Spectrum

This quantity is defined by

$$\gamma_{12}^2(f) = \frac{|S_{12}(f)|^2}{S_1(f)\,S_2(f)}, \tag{E.56}$$

with

$$\gamma_{12}^2 \leq 1 .$$

4. Bispectral Density

The bispectral density is defined by

$$B(f_1, f_2) = \lim_{T\to\infty} \frac{1}{T} E[G(f_1)(f)\,G(f_2)\,G^*(f_1 + f_2)]. \tag{E.57}$$

It is the two-dimensional Fourier transform of the bicorrelation function defined by

$$R(\tau_1, \tau_2) = E[g(t)g(t + \tau_1)g(t + \tau_2)]. \tag{E.58}$$

The mean cube $E[g^3(t)]$ is given by

$$R(0,0) = E[g^3(t)] = \int_{-\infty}^{\infty}\int_{-\infty}^{\infty} B(f_1,f_2)df_1\,df_2. \tag{E.59}$$

Since $B(f_1, f_2)$ is symmetrical, only its real part contributes to the above integral which gives

$$R(0,0) = E[g^3(t)] = \int_{-\infty}^{\infty}\int_{-\infty}^{\infty} Re[B(f_1,f_2)]df_1\,df_2. \tag{E.60}$$

The quantity $B(f_1, f_2)\,(\Delta f)^2$ represents the contribution to the mean cube of the spectral components lying in the intervals $f_1, f_1 + \Delta f$ and $f_2, f_2 + \Delta f$ in the $f_1\,f_2$-plane.

c. Plasma transport

Plasma turbulence can affect strongly the transport properties of a plasma and in particular its radial transport across a magnetic field. This type of particle transport across the magnetic field lines is referred to as fluctuation-induced transport. To study this process, it is necessary to find a relationship between the observed spectral characteristics of the turbulence and fluctuation-induced transport. This has been done by Powers et al. (Powers et al., 1978). The Fourier transform of the digitized signals proportional to the density and potential fluctuations are first computed using an FFT algorithm. A transport spectral density function T(f) is then defined as

$$T(f) = 2\, k_\theta(f)\, Q_{n\phi}(f)/B, \tag{E.61}$$

where $Q_{n\phi}$ (f) is the quadrature spectrum between density and potential fluctuations, k_θ is the poloidal wave number, and B is the magnetic field. The factor 2 accounts for "negative frequency". T(f) is an even function of frequency. It indicates quantitatively how many particles per unit area, time, and frequency have been transported in a certain spectral band. The transport associated with the small spectral band of width Δf centered at a frequency f can be expressed as follows

$$T(f)\Delta f = \frac{k_\theta(f)}{B}\, n(f)\phi(f) \sin[\alpha_{n\phi}(f)]\, \gamma_{n\phi}(f), \tag{E.62}$$

where $\alpha_{n\phi}(f)$ and $\gamma_{n\phi}(f)$ are respectively the phase and coherency spectra between the density and phase fluctuatons. The above expression not only gives the amount of transport associated with the band Δf but also gives its direction, which is given by the sign of T(f).

d. Experimental set-up for turbulence diagnostic

The method used to study plasma turbulence in these experiments is based on digital time series analysis. Digital time series analysis permits one to extract the desired information from a background of noise. The techniques used by this method are statistical and use digital spectral analysis based on fast Fourier transform (Smith et al., 1974). The block diagram of the data acquisition system is shown in Fig E.7. The potential fluctuations are detected by capacitive probes. The signals proportional to the potential fluctuations are fed to Tektronix 1121 amplifiers and to Kron-Hite 3200 filters set as a band pass filter. The signals out of the filters are digitized by LeCroy TR 8837 transient recorders. These transient recorders are capable of sampling up to 32 mega-samples/second, and storing the digitized signal in an 8K-x-8-bit memory. The user may dedicate only a fraction of the available memory. The data sampling is halted by a stop trigger pulse. To the data residing in the histogram memory of the signal analyzer (Lecroy 3500 SA), fudiciary data such as date, run number, file number, anode voltage, magnetic field, pressure, etc. is added, then sent to the host computer (VAX 11/780) for processing. The communication between the signal analyzer, Lecroy 3500 SA, and the host computer, VAX 11/780, is achieved through a quad serial communication board which provides four standard RS-232-C ports. The processed data is sent back from the host computer to the signal analyzer which has its own plotting subroutine. The data is read and the various spectra such as auto-power spectrum, cross-power spectrum, phase spectrum and squared coherency spectrum are plotted. The time series itself can be retrieved and plotted.

e. Interpretation of the fluctuation spectra

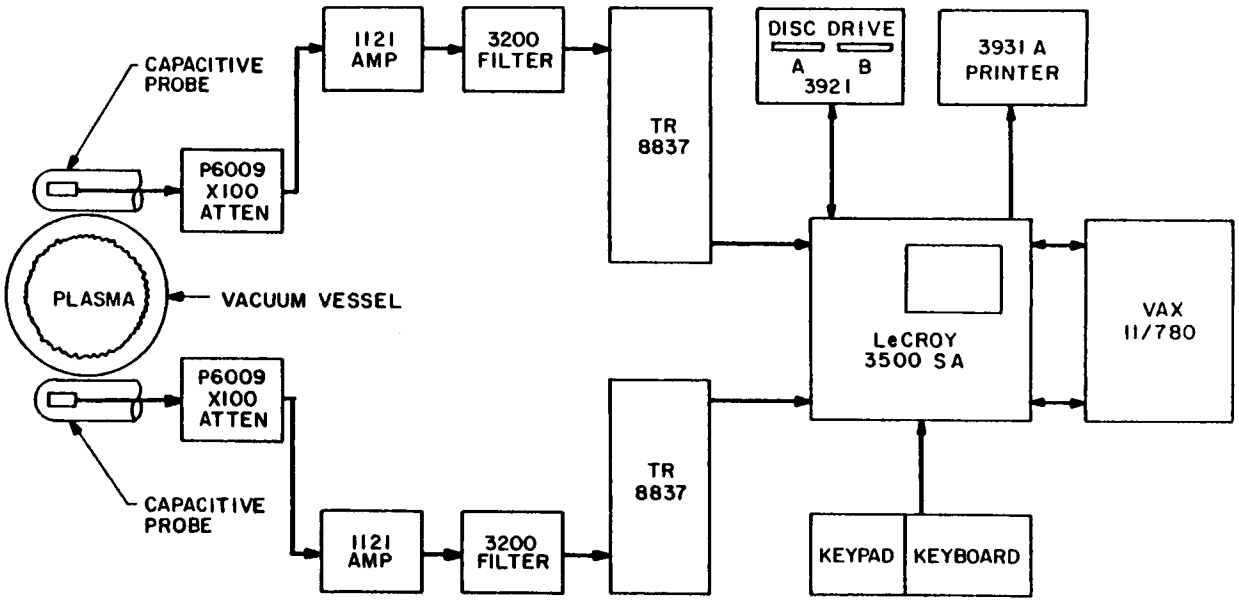

Fig E.7. Block diagram of a two channel data acquisition and handling system.

From the various spectra obtained by the application of digital time series analysis, one can extract physical parameters characterizing the turbulent state of the plasma. From the log-log plot of the auto-power spectrum, one can measure the extent to which the power spectrum follows a power law. The slope of the straight line in the log-log plot gives the spectral index. From the peaks in the power spectrum one can determine the frequencies of the different modes present in the plasma. The phase spectrum with some modifications gives the relationship between $k(\omega)$ and ω, which is often needed to compare theoretical and experimental results. Also the phase velocity of the modes present can be calculated in the following fashion (Smith and Powers, 1973). If a peak is present at a certain frequency ω, and $\theta_{xy}(\omega)$ is the phase shift of the fluctuating potential signal monitored at two different locations x and y, then we have

$$\theta_{xy}(\omega) = k(\omega)\,\Delta S, \tag{E.63}$$

where ΔS is the distance between the two probes, and $k(\omega)$ is the wave number at the frequency ω where the peak is located. If the probes are located at the same radius but at two different azimuthal angles, we have

$$\Delta S = r\,\Delta\theta\ , \tag{E.64}$$

where r is the radius and $\Delta\theta$ is the angle between the probes. The azimuthal mode number is given by

$$m(\omega) = \theta_{xy}(\omega)/\Delta\theta\ . \tag{E.65}$$

In cylindrical geometry we have

$$k(\omega) = m(\omega)/r\ . \tag{E.66}$$

The phase velocity of a wave of frequency ω is given by

$$v_{ph} = \omega/k. \tag{E.67}$$

Substituting K and $m(\omega)$ by their expressions in Equation (III.67) we get

$$v_{ph} = \omega r\,\Delta\theta/\theta_{xy}(\omega)\ . \tag{E.68}$$

If the mode under study is an E x B drift wave then the electric field strength of the wave is

$$E = vB , \tag{E.69}$$

where v is the phase velocity of the wave and B is the axial magnetic field.

f. Experimental data analysis

In this subsection a few experimental runs have been selected to show some of the turbulent processes going on in the plasma and to illustrate the use of digital spectral analysis. The different spectra presented are based on a two channel system, where the digitized signals are sampled fluctuating potentials detected by two capacitive probes at two different locations. Each of Fig E.8 through Fig E.10 consists of four spectra. Spectra A and B are autopower spectra. Spectrum C is the phase spectrum and spectrum D is the coherency spectrum. The frequency span over which these spectra are studied is 0-500 kHz.

Fig E.8 and Fig E.9 are spectra associated with signals detected by two capacitive probes located at the anode position but 90° apart. They show that a high degree of turbulence is present in the plasma, with the existence of one discrete mode of oscillation at about 100 kHz. This can be checked by the high degree of coherency around that frequency and a weak coherency elsewhere. The phase spectra show that the dispersion relation is linear across most of the frequency range, and that the fluctuations are rotating in the azimulthal direction with a phase velocity of about 1.95 10^4 m/s. Fig E.10 shows spectra associated with signals detected by two capacitive probes located at the same azimuthal position but 26 cm apart. A high degree of turbulence is present with a prominent peak around 180 kHz in channel 2. The coherency is low

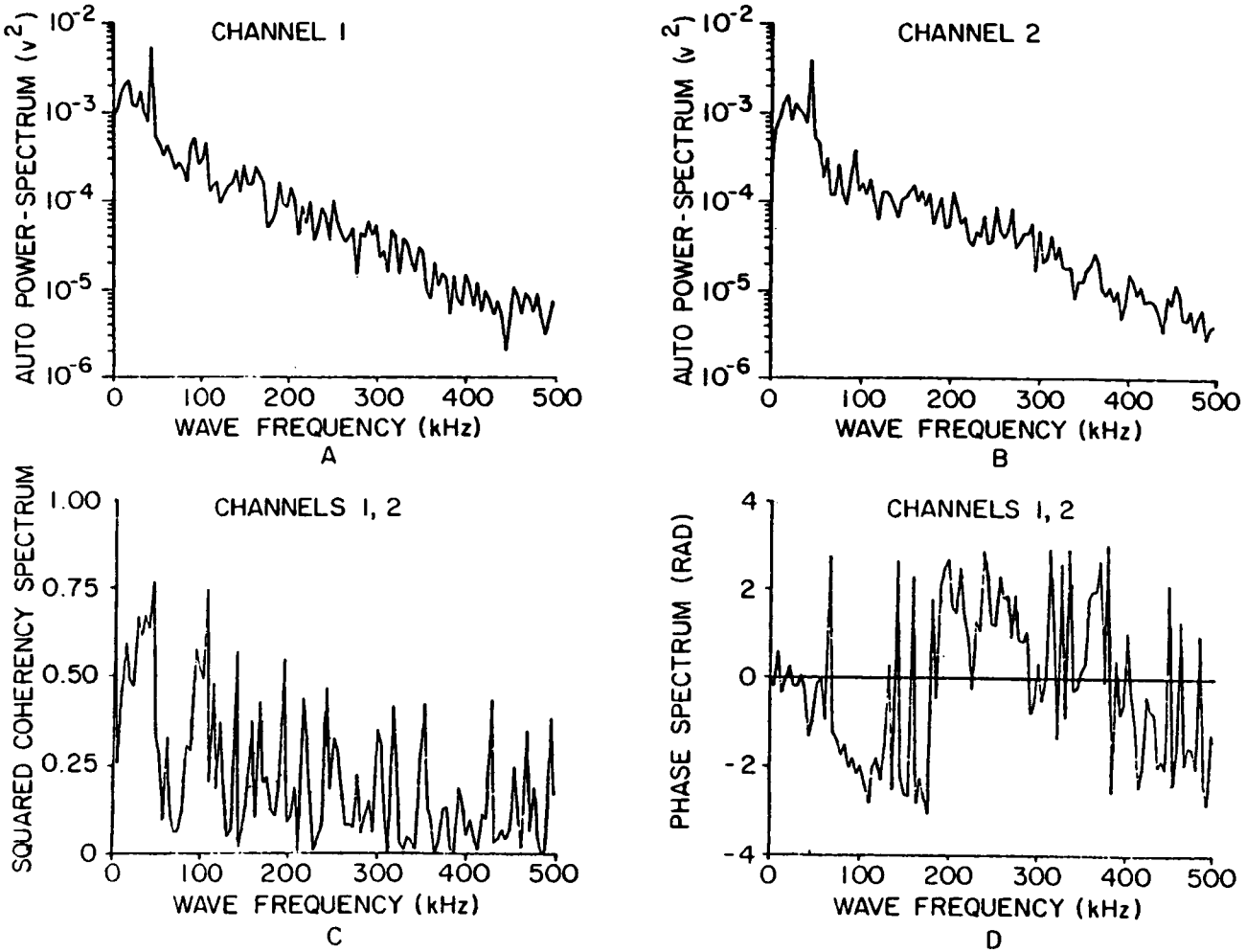

Fig E.8. Autopower spectra (A and B), coherency spectrum (C), and phase spectrum (D) of two potential fluctuations detected by two capacitive probes 90° apart, P = 190 μ Torr, V_A = 1.3 kV, I_A = 56 mA, B = 0.262 Tesla.

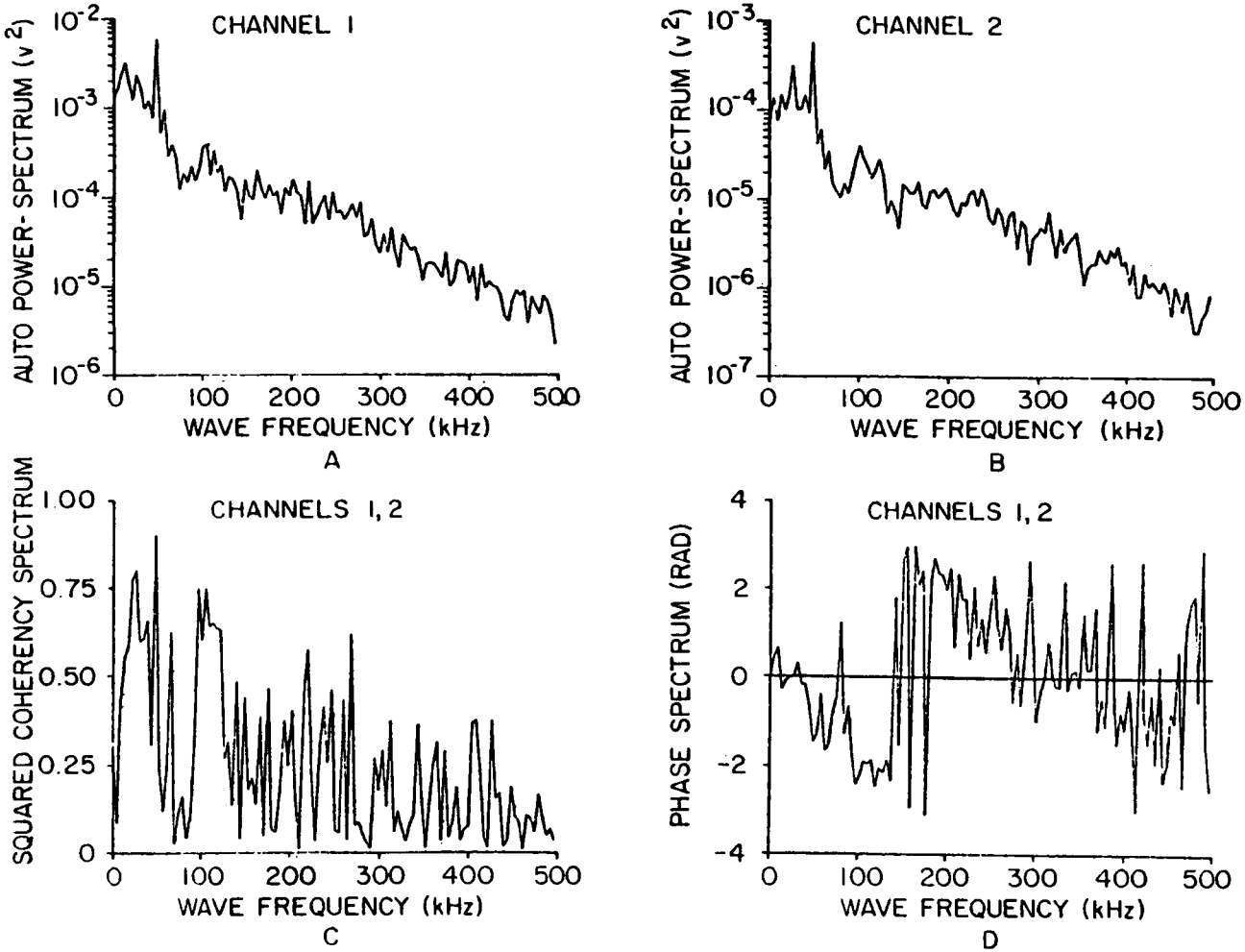

Fig E.9. Autopower spectra (A and B), coherency spectrum (C), and phase spectrum (D) of two potential fluctuations detected by two capacitive probes 90° apart, P = 210 μ Torr, V_A = 1.3 kV, I_A = 58 mA, B = 0.3 Tesla.

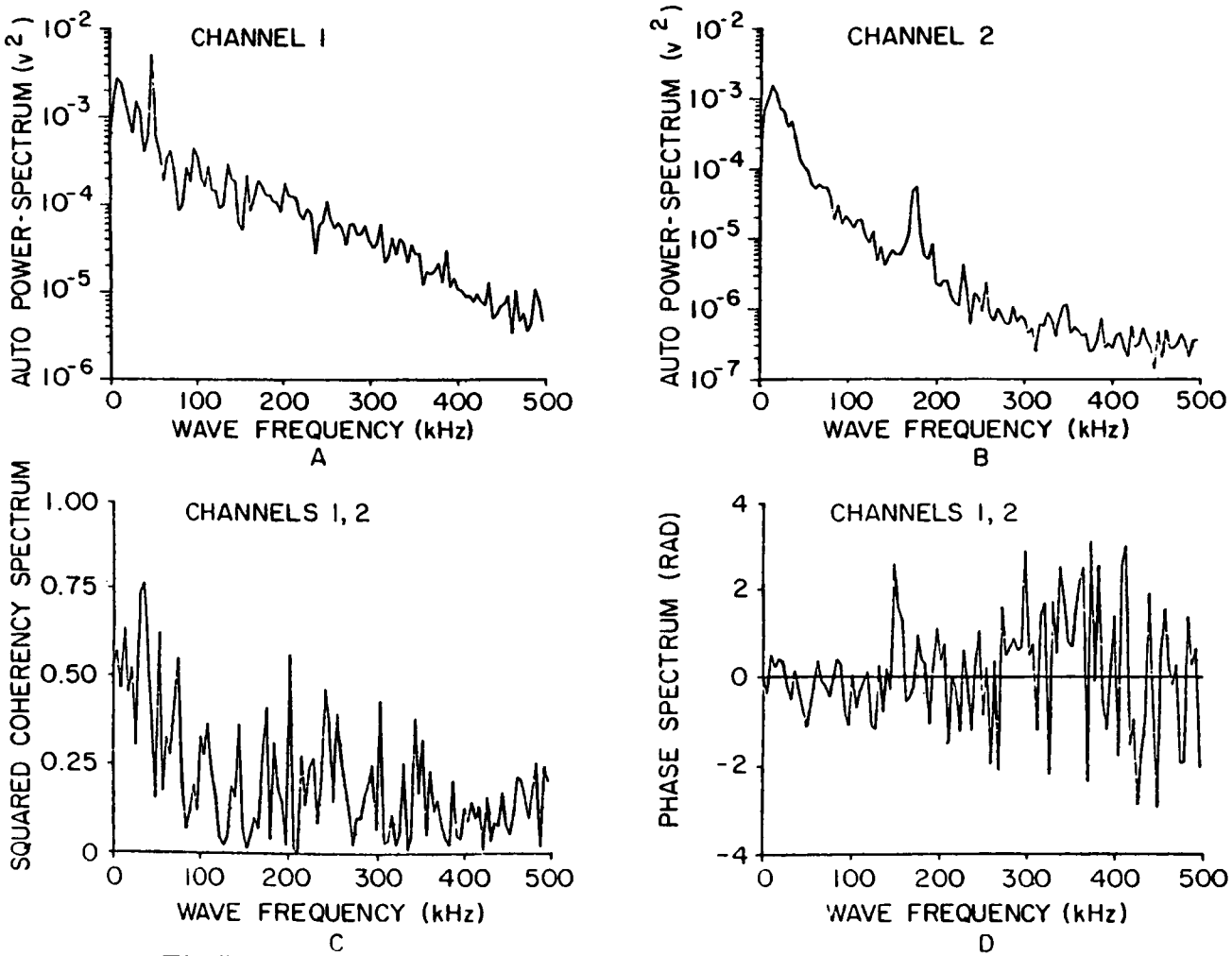

Fig E.10. Autopower spectra (A and B), coherency spectrum (C), and phase spectrum (D) of two potential fluctuations detected by two capacitive probes 26 cm apart at the same azimuthal angle, $\theta = 0°$. P = 210 μ Torr, V_A = 1.3 kV, I_A = 58 mA, B = 0.3 Tesla

across the whole frequency range. The phase spectrum shows a nonlinear dispersion relation and that the fluctuations detected by the two capacitive probes are occuring independently at the same time. This suggests that no axial propagation is present. This is reinforced by the low degree of coherency between channel 1 and channel 2.

Fig E.11 through Fig E.13 are selected autopower spectra plotted both on a linear and logarithmic frequency scales. The plasma parameters for the three cases are kept constant except for the magnetic field. The low and high frequency of the band pass filter are set to 500 Hz and 500 kHz. The linear plots show a high degree of turbulence with a discrete mode the frequency of which decreases as the magnetic field strength increases. This is an E x B drift mode. The logarithmic plots show a power law relationship with various spectral indices. In all cases the spectral index was less than the theoretical predicted value of 5. This is most probably due to the fact that the wave number, k, was not proportional to the frequency, ω, over the frequency range where the autopower spectrum obeys a power law. This indicates highly dispersive turbulent modes.

Fig E.14 shows a collection of power spectra of potential fluctuations, taken at the same plasma parameters but for different magnetic field strengths. The unit on the y-axis is arbitrary and the spectra are placed on top of each other for comparison purposes. Three distinct modes of oscillation are apparent. The first peak to the left is due to the contunuity equation oscillation (Roth, 1969). This mode does not depend on the magnetic field, but is a function of the neutral and electron densities (A detailed analyses of this mode is found in (Roth, 1969)). The second and third peaks are found to be E x B drift modes. This can be concluded easily by inspecting Fig E.15 and Fig

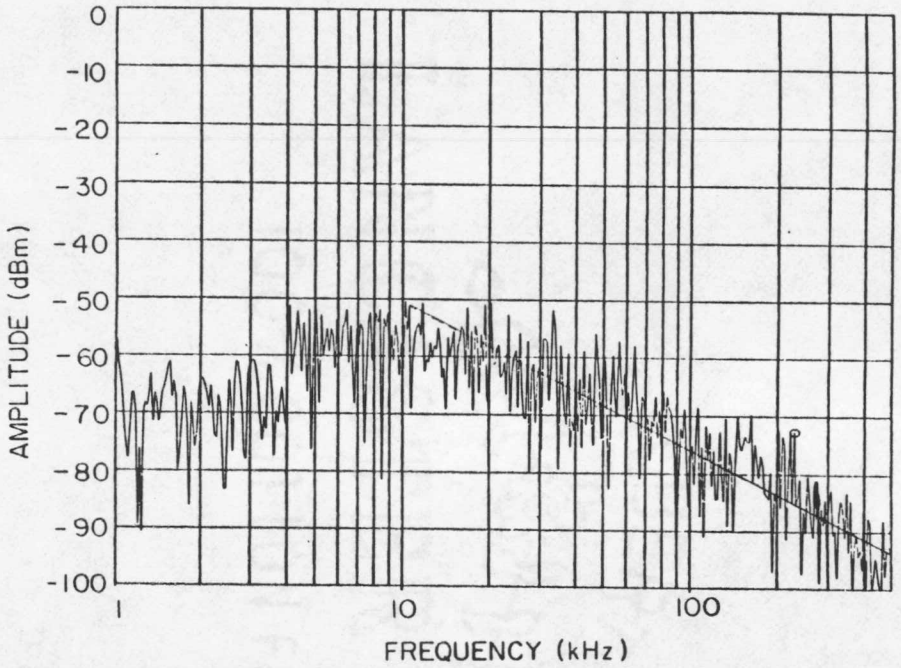

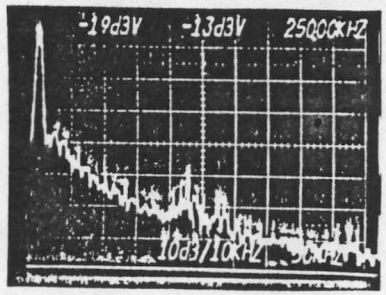

A

B

Fig E.11. Autopower spectrum on linear frequency scale (A), and on logarithmic frequency scale (B) with a spectral index $n = 2.5$, $P = 47\ \mu$ Torr, $V_A = 1.6$kV, $I_A = 22$ mA, $B = 0.3$ Tesla.

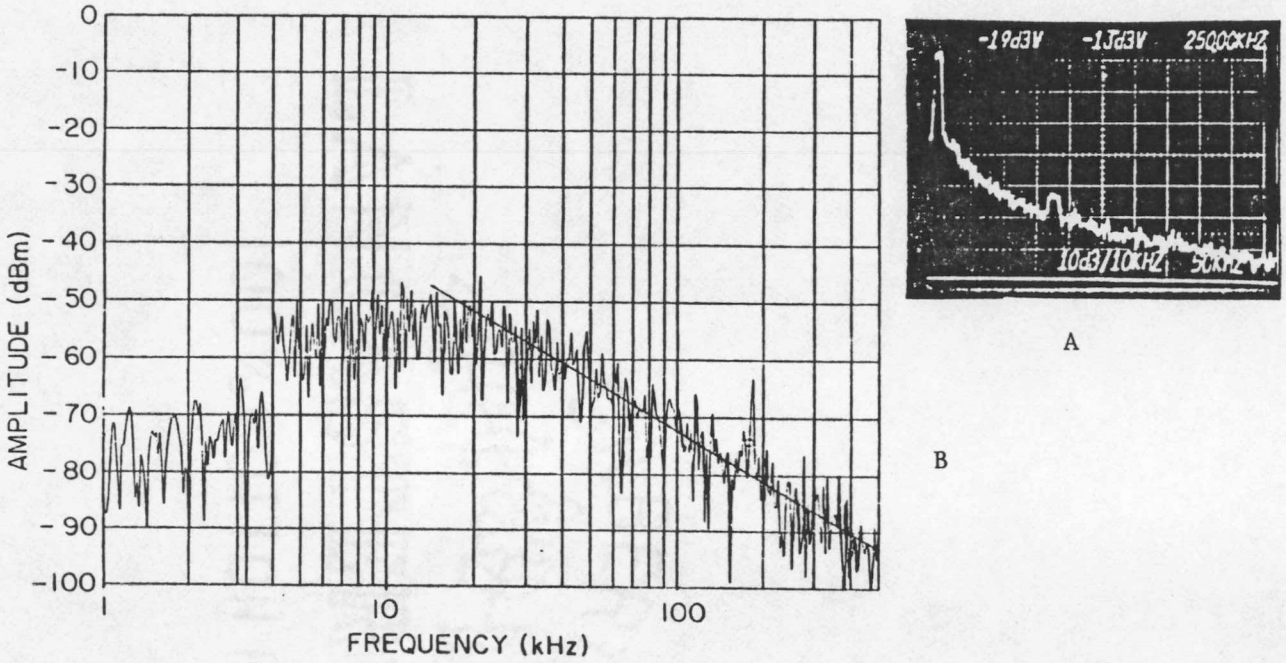

Fig E.12. Autopower spectrum on linear frequency scale (A), and on logarithmic frequency scale (B) with a spectral index n = 2.92, P = 55 μ Torr, V_A = 1.6 kV, I_A = 24 mA, B = 0.347 Tesla.

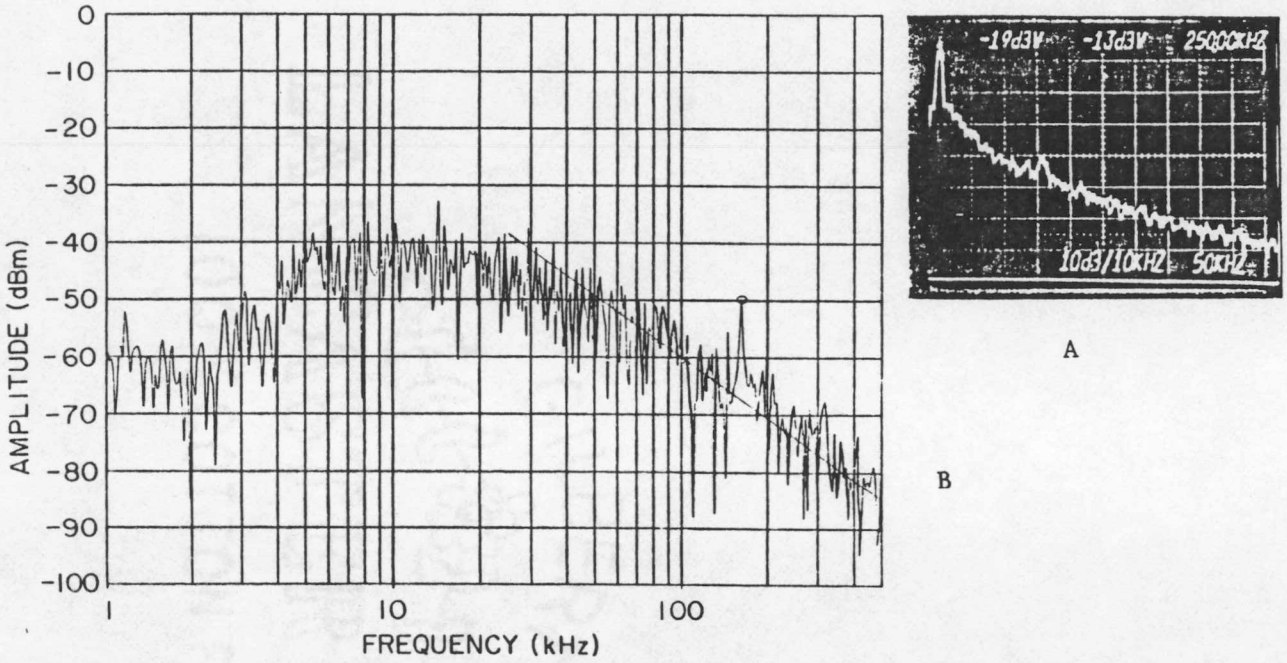

Fig E.13. Autopower spectrum on linear frequency scale (A), and on logarithmic frequency scale (B) with a spectral index n = 3.57, P = 50 μ Torr, V_A = 1.6 kV, I_A = 20 mA, B = 0.395 Tesla.

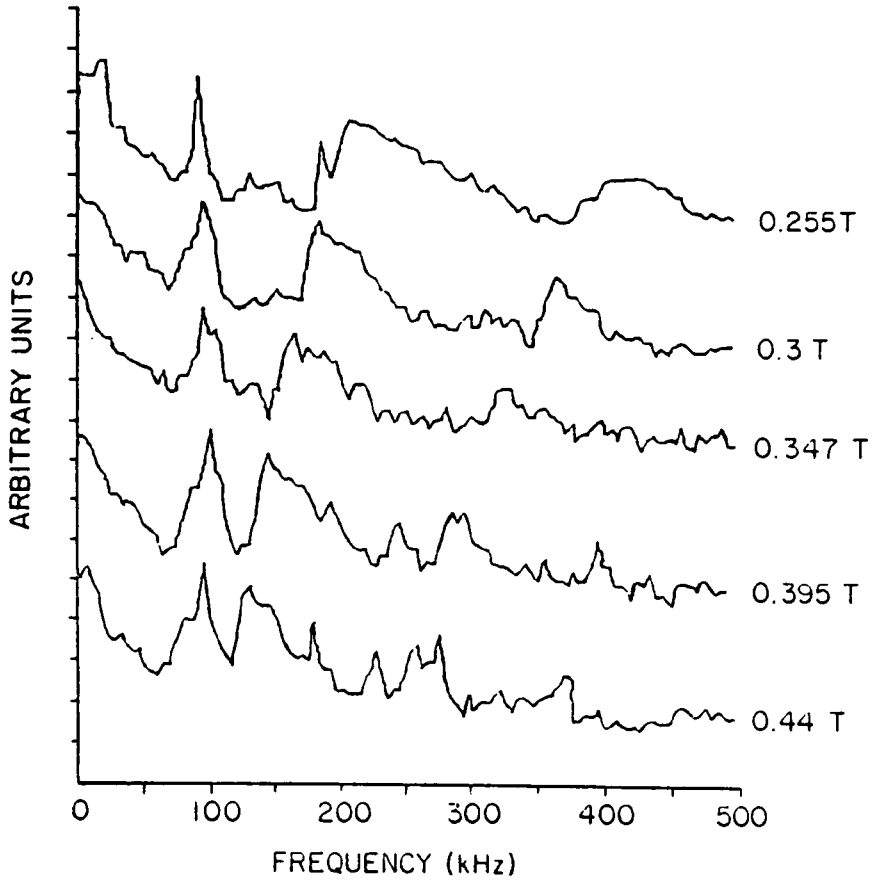

Fig E.14. Autopower spectra of potential fluctuations at V_A = 1.3 kV, I_A = 2 mA, P = 30 μ Torr, and various magnetic field strengths.

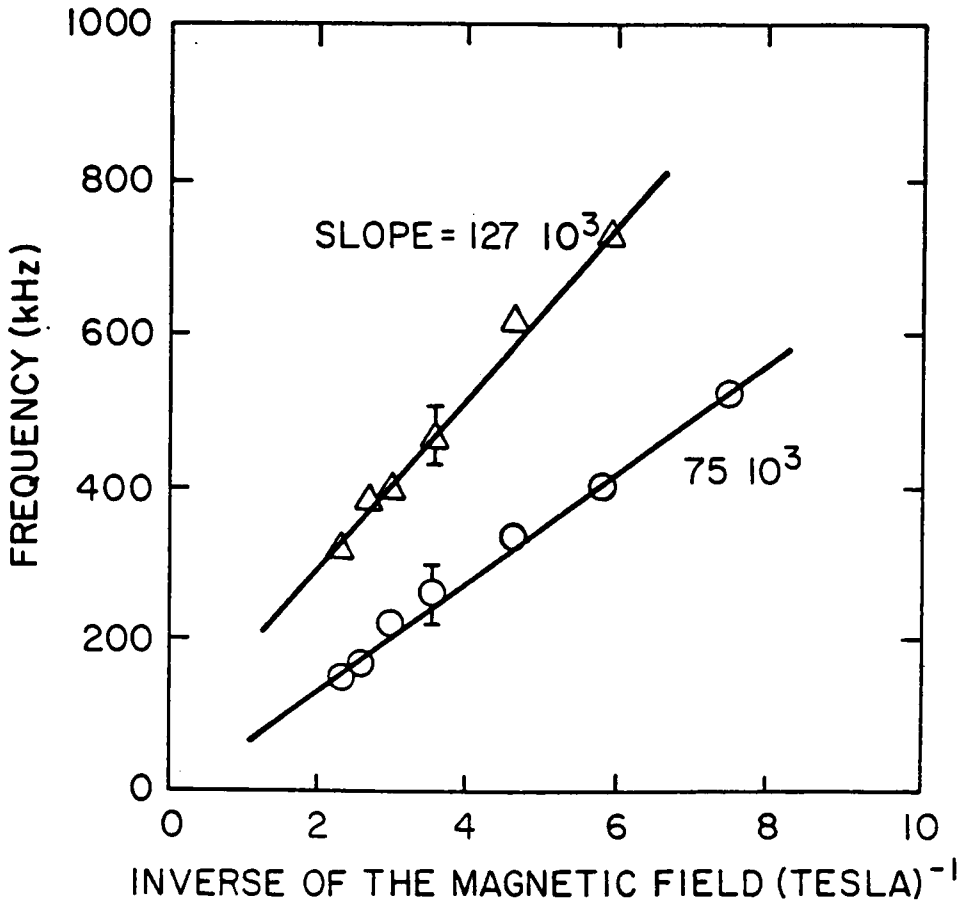

Fig E.15. Mode frequency versus the inverse of the magnetic field strength.

E.16. Fig E.15 shows that the plot of the frequency of these two peaks against the inverse of the magnetic field strength, is a straight line and Fig E.16 shows that the mode frequency is proportional to the radial electric field, since the latter is itself proportional to the anode voltage.

The above data present only a small selection from an extensive collection for illustrative purposes, to help understand the behavior of the plasma on which collisional magnetic pumping is to be applied. More experimental data and turbulence analysis can be found in (Roth et al., 1981), (Laroussi et al., 1985), and (Baylor et al., 1984).

E.2.3 Effective Collision Frequency

The turbulent state of a plasma has an important influence on momentum transfer between charged particles. In a turbulent plasma electrons lose momentum to the waves generated by the various instabilities which in turn transfer their momentum to the ions. This anomalous momentum transfer tends to enhance the collision frequency and increase the resistivity of the plasma (Roth and Spence, 1987). In this section a theoretical treatment of this process along with an experimental measurement of the enhanced collision frequency is presented.

a. Theoretical background

The resistivity of a current-carrying plasma is defined by

$$\rho = \frac{m v_c}{n e^2} , \qquad \text{(E.70)}$$

where v_c is the collision frequency of electrons with scattering centers, such as ions and neutral atoms. If an instability develops, along with the momentum loss by binary collision, electrons also lose momentum through emission of

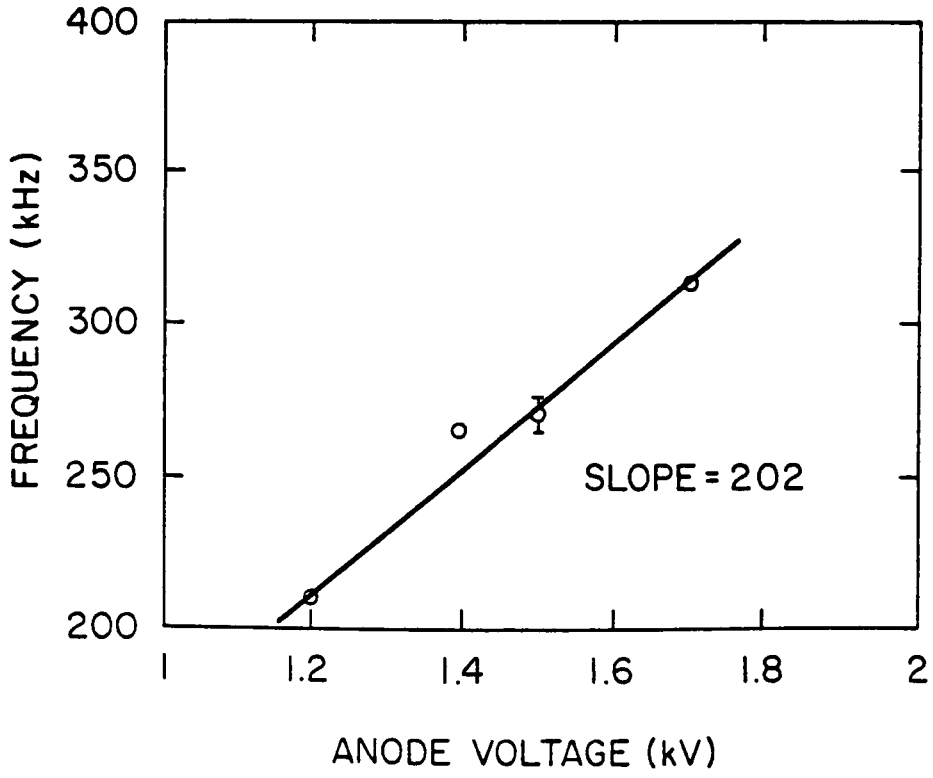

Fig E.16. Mode frequency versus anode voltage.

waves. The momentum of this emission is subsequently absorbed by the ions. This anomalous momentum loss increases the collision frequency which in its turn causes an anomalous plasma resistivity. An effective collision frequency, ν_{eff}, is therefore defined, when due to the existence of an instability, electrons excite waves through which an anomalous momentum loss occurs. An important class of instabilities that contribute to such a process are the electrostatic instabilities with $k^2_{\parallel} << k^2_{\perp}$, where $k_{\parallel}$ and $k_{\perp}$ are respectively the wave-numbers along and across the magnetic field lines. Drift wave instabilities are such a kind. In this case a current flows across the magnetic field causing an anomalous plasma transport.

The effective collision frequency can be found using the momentum conservation laws of the electron-wave system. The frictional force acting on the electrons can be expressed as

$$F_{fr} = - \nu_{eff} m_e n_o v_{De}, \tag{E.71}$$

where m_e is the electron mass, n_o is the number density, and v_{De} is the electron drift velocity, or using the momentum of waves emitted by the electrons (Rosenbluth and Sagadeev, 1984)

$$F_{fr} = 2 \int \gamma^e_k W_k \left(\frac{k}{\omega_K} \right) \frac{dk}{(2\pi)^3}, \tag{E.72}$$

where γ^e_K is the contribution of electrons to the instability growth rate and W_K is the spectral energy density of waves. The effective collision frequency is given by (Rosenbluth and Sagadeev, 1984)

$$\nu_{eff} = \frac{2}{m_e n_o v_{De}} \int \gamma^e_k W_k \left(\frac{k}{\omega_K} \right) \frac{dk}{(2\pi)^3}. \tag{E.73}$$

In the case of drift wave instabilities, the wave energy density is given by Horton as (Rosenbluth and Sagadeev, 1984)

$$W_k = \frac{e^2 n_e}{2\,Te}\left(1 + k_\perp^2 \rho^2\right)\left|\,\phi(k)\right|^2, \tag{E.74}$$

where ϕ is the electrostatic potential, and ρ is given by

$$\rho = \frac{(m_i T_e)^{1/2}}{e\,B}, \tag{E.75}$$

where T_e is the electron kinetic temperature, and m_i is the ion mass. The coefficient ρ describes the wave dispersion due to the ion inertia that produces a polarization current. The wave energy density can also be written as

$$W_k = \left(\frac{e^2 n_e}{2\,Te} + k_\perp^2 \frac{n_e m_i}{2\,B^2}\right)\left|\,\phi(k)\right|^2. \tag{E.76}$$

Plugging the above expression in Equation (III.73) gives

$$\nu_{eff} = \frac{2}{m_e n_o v_{De} (2\pi)^3}\left[\frac{e^2 n_e}{2\,T_e}\int \gamma_k^e \left|\,\phi(k)\right|^2 \left(\frac{k}{\omega}\right) dk\right.$$

$$\left. + \frac{n_e m_i}{2\,B^2}\int \gamma_k^e k_\perp^2 \left|\,\phi(k)\right|^2 \left(\frac{k}{\omega}\right) dk\right], \tag{E.77}$$

or

$$\nu_{eff} = \frac{\varepsilon_o \omega_{pe}^2}{n_o T_e v_{De} (2\pi)^3}\int \gamma_k^e \left|\,\phi(k)\right|^2 \left(\frac{k}{\omega}\right) dk$$

$$+ \frac{n_e m_i}{m_e n_o v_{De}\, 2\,B^2 (2\pi)^3}\int \gamma_k^e k_\perp^2 \left|\,\phi(k)\right|^2 \left(\frac{k}{\omega}\right) dk, \tag{E.78}$$

where ω_{pe} is the electron plasma frequency given by $\omega_{pe} = (n_e\, e^2/\varepsilon_o\, m_e)^{1/2}$. Equation (E.78) is a general expression of the effective collision frequency for a magnetized plasma where drift wave instabilities are dominant. Equation (E.78) shows that ν_{eff} depends strongly on the plasma parameters such as the electron plasma frequency, the number density, and the electron temperature. Knowledge of the turbulence potential fluctuation spectral density allows the

calculation of ν_{eff}. The potential fluctuation spectrum can be experimentally observed using a capacitive probe for detection and digital spectral analysis for processing.

b. Experimental Measurement of ν_{eff}

The experimental measurement of the effective collision frequency, ν_{eff}, was made on the basis of the absorption measurements near electron cyclotron resonance (Roth and Spence, 1987). The solution for propagation of an electromagnetic wave in a uniform medium can be expressed in terms of a complex refractive index defined as $\mu \cdot \mu$ can be expressed as

$$\mu = \mu - jX , \tag{E.79}$$

with

$$\mu = \frac{c\beta}{\omega} , \tag{E.80}$$

and

$$X = \frac{c\alpha}{\omega} , \tag{E.81}$$

where α and β are respectively the real and imaginary part of the complex propagation constant γ appearing in the phase factor $\exp(i\omega t - \gamma z) \cdot \alpha$ is the attenuation coefficient and β is the phase coefficient. The problem of the propagation of a plane wave in a Lorentzian plasma was treated by Appleton (Heald and Wharton, 1978). By Lorentzian plasma we mean a plasma where positive ions and neutral molecules cause a damping of the electron motion. For such a plasma a damping term is added to the momentum equation. This damping term is given by (ν_c mv), where ν_c is the momentum transfer collision frequency. For an electromagnetic wave launched in the extra-ordinary mode (The electric field of the wave is perpendicular to the background magnetic field), Appleton derived the complex dielectric function $\varepsilon(\omega)$ to be (Heald and

Wharton, 1978)

$$\varepsilon(\omega) = \mu_{ex}^2 = 1 - \frac{\dfrac{\omega_p^2}{\omega^2}}{1 - j\dfrac{\nu_c}{\omega} - \dfrac{\omega_{cy}^2/\omega^2}{1 - \dfrac{\omega_p^2}{\omega^2} - j\dfrac{\nu_c}{\omega}}}, \qquad \text{(E.82)}$$

where ω_p, ν_c and ω_{cy} are respectively the plasma frequency, the collision frequency, and the cyclotron frequency. This is Appleton's equation for a wave propagating in the extra-ordinary mode. Appleton's equation gives the propagation indices for a plane wave in a magnetized cold plasma that is uniform over a dimension larger than the wave length. A plasma is defined to be cold when the thermal speed of the particles is negligible with respect to the phase velocity of the wave.

The expression for $\varepsilon(\omega)$ has a resonant behavior with maximum absorption at $\omega = \omega_{cy}$. The full width at twice the minimum transmitted power (or at half the maximum absorbed power) represents the collision frequency. Experimentally the absorption curve is plotted using a Hewlett Packard 8510 Network Analyser (Roth and Spence, 1987). This instrument is capable of measuring the reflection and transmission coefficients over a frequency band extending from 45 MHz to 18 GHz with a dynamic range greater than 80 dB. The RF wave is polarized with its electric field perpendicular to the ambient magnetic field and launched and received by custom made, specially designed horns. The experimental setup is shown in Fig E.17. Fig E.18 shows the resonant absorption curve with the collision frequency measured as the full width at twice the minimum. The collision frequencies measured by this method are in general one to two order of

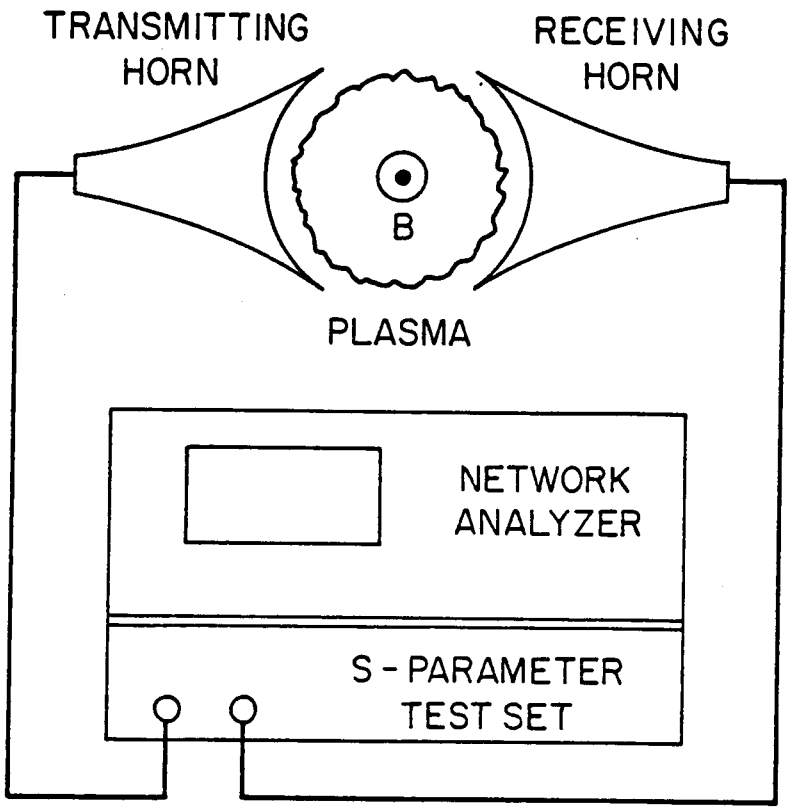

Fig E.17. Experimental setup for the measurement of the effective collision frequency.

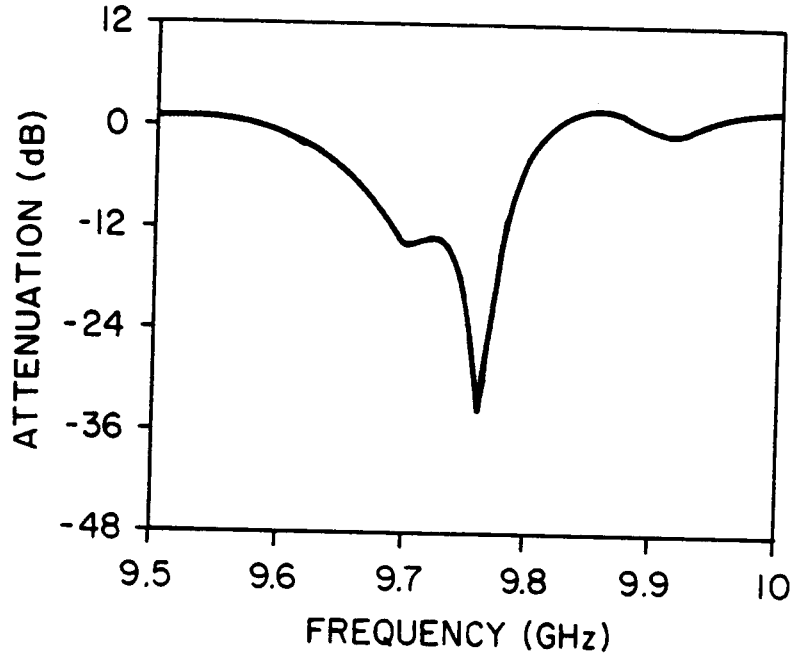

Fig E.18. Resonance absorption curve with an effective collision frequency of 7.5 MHz.

magnitude larger than the binary collisions. This is due to the strong turbulence existing in the plasma.

Appendix F

Binary Collision Frequencies

In this appendix we compute the values of the collision frequencies associated with the various types of binary collisions occuring in the plasma produced by the classical Penning discharge. The plasma parameters used in these computations correspond to a typical experimental run. They are measured with the appropriate diagnostics available in our laboratory. The gas selected is helium since it is the most often used.

The collision processes are going to be divided into two sets. The first set deals with charged particles (or neutrals) colliding with neutrals. The second set deals with charged particles colliding with charged particles. For all these computations the electron temperature, ion temperature and electron (or ion) number density are respectively chosen to be 10 eV, 1 keV, and $10^{15}\,m^{-3}$.

1. Charged Particles (or Neutrals) Colliding with Neutrals

In these computations the base pressure is assumed to be 100 μ Torr which corresponds to a neutral number density of $n \sim 3.45\,10^{18}\,m^{-3}$. The neutral atoms are assumed to be at room temperature T = 300°K ~ 0.0258eV. The helium atom radius is r = 0.504Å.

a. Neutral-Neutral

The mean thermal velocity of a neutral atom is

$$\bar{v} = \left(\frac{8kT}{\pi m}\right)^{1/2} = 1.25\,10^{3}\,m/s\,.$$

The cross-section is

$$\sigma = 4\pi r^2 = 3.19\,10^{-20}\,m^2\,.$$

The collision frequency is

$$\nu_c = \sigma n \bar{v} = 137 \quad \text{coll/s, or 137 Hz.}$$

b. Ion-Neutral

The mean thermal velocity of an ion is

$$\bar{v} = \left(\frac{8kT_i}{\pi m_i} \right)^{1/2} = 2.46\, 10^5 \text{ m/s}.$$

The cross-section is $\sigma = 3.19\, 10^{-20}\ m^2$. The collision frequency is

$$\nu_c = \sigma n \bar{v} = 27\, 10^3 \quad \text{coll/s, or 27 kHz.}$$

c. Electron-Neutral

The mean thermal velocity of the electron is

$$\bar{v} = \left(\frac{8kT_e}{\pi m_e} \right)^{1/2} = 2.1\, 10^6 \text{ m/s}.$$

The cross-section is $\sigma = 3.19\, 10^{-20}\ m^2$. The collision frequency is

$$\nu_c = \sigma n \bar{v} = 265\, 10^3 \quad \text{coll/s, or 265 kHz.}$$

2. Charged Particles Colliding with Charged Particles

a. Electron-Electron

The electron-electron collision time is given by multiple small angle collisions

$$\tau_{ee} \approx \frac{25.8\sqrt{\pi}\,\varepsilon_o^2 m_e^{1/2} (kT_e)^{3/2}}{n_e e^4 \ell n\, \Lambda}.$$

A more practical expression of τ_{ee} is

$$\tau_{ee} = 5.264\, 10^{-6} \frac{T_e^{3/2}}{n_e},$$

where T_e is expressed in KeV and n_e is in units of 10^{20}.

$$\tau_{ee} = 5.264\, 10^{-4} \text{s}.$$

The collision frequency is

$$\nu_c = \frac{1}{\tau_{ee}} \approx 1.9\ \text{kHz}\ .$$

b. Electron-Ion

The electron-ion collision time is given by

$$\tau_{ei} = \frac{51.6\sqrt{\pi}\ \varepsilon_o^2 m_e^{1/2} (kT_e)^{3/2}}{n_e Z e^4 \ell n\ \Lambda},$$

or

$$\tau_{ei} = 1.053\ 10^{-5}\ \frac{T_e^{3/2}(\text{KeV})}{Z\, n_e (10^{20})}.$$

For Z = 1 we have

$$\tau_{ei} = 1.053\ 10^{-3}\ \text{s}.$$

The collision frequency is

$$\nu_c = \frac{1}{\tau_{ei}} \approx 950\text{Hz}\ .$$

c. Ion-Ion

The ion-ion collision time is given by

$$\tau_{ii} = \frac{25.8\sqrt{\pi}\ \varepsilon_o^2 m_i^{1/2} (kT_i)^{3/2}}{n_e Z^3 e^4 \ell n\ \Lambda},$$

or

$$\tau_{ii} = 2.256\ 10^{-4}\ \frac{\sqrt{A}}{Z^3}\ \frac{T_i^{3/2}(\text{KeV})}{n_e (10^{20})},$$

where A is the atomic mass. A = 4 for helium.

$$\tau_{ii} = 5.64\ \text{s}.$$

The collision frequency is

$$\nu_c = \frac{1}{\tau_{ii}} = 0.177\ \text{Hz}\ .$$

d. Ion-Electron

The ion-electron collision time is given by

$$\tau_{ie} = \frac{3\pi\,\varepsilon_o^2\, m_i\,(kT_e)^{3/2}}{n_e Z^2 e^4 \ell n\,\Lambda},$$

or

$$\tau_{ie} = 5\,10^{-3}\,\frac{A\,T_e^{3/2}(\mathrm{KeV})}{z^2\, n_e(10^{20})}.$$

$\tau_{ie} = 2$ seconds.

The collision frequency is

$$\nu_c = \frac{1}{\tau_{ie}} = 0.5\ \mathrm{Hz}.$$

Table F.1 is a rank of the collision frequencies of the processes seen above.

Collision	Collision Frequency, Hz
Electron-Neutral	$265\,10^3$
Ion-Neutral	$27\,10^3$
Electron-Electron	$1.9\,10^3$
Electron-Ion	950
Neutral-Neutral	137
Ion-Electron	0.5
Ion-Ion	0.177
Effective Collision Frequency (Fig E.18)	$7.5\,10^6$

Table F.1. Collision frequencies for the various binary collision processes.

Table F.1. shows that the dominant form of binary collision is the charged particle-neutral collisions. This is because the plasma produced by

the classical Penning discharge is weakly ionized and the charged particles have a relatively high kinetic temperature. As mentioned in Chapter III, the electron-neutral collisions are the most frequent and determine the properties of the plasma and its ionization level when binary collisions are dominant. Measurements in this plasma indicate (as shown on Table F.1) an effective collision frequency of 7.5 MHz, many orders of magnitude above the binary collision frequencies.

VITA

The author was born in Sfax, Tunisia, on August 9, 1955. He attended a technical high school (Lycee Technique) in Sfax, Tunisia. He was admitted to the University of Sciences in Tunis, Tunisia, where he majored in mathematics and physics. After two years, he joined the Engineering School of Sfax where he majored in Electrical Engineering. He obtained his Master of Science degree in June 1981. He accomplished his Master thesis at the "Ecole Nationale Superieure d'Electronique et d'Electricite de Bordeaux", in Bordeaux, France, where he built a single-phase DC-AC converter.

In September 1981, the author was admitted to the University of Tennessee at Knoxville to begin his studies for the Ph.D. degree in Electrical Engineering. He held a graduate teaching position instructing electronics, circuits, and plasma labs.

In March 1984, he joined the staff of the Plasma Science Laboratory as a research assistant. He was the senior assistant on an experiment funded by the Air Force Office of Scientific Research. His research duties included RF emission from plasmas, drift-wave instabilities in plasmas, and plasma heating.

The author received his Ph.D. in Electrical Engineering in June 1988.